Doctoral Dissertation
Doctoral Program in Energetics (36th Cycle)

Modelling of Concentrated Solar Power Systems

Mehdi Shokrnia

Supervisors:
Prof. Roberto Zanino, Supervisor
Dr. Mattia Cagnoli, Co-Supervisor

Doctoral Examination Committee:
Dr. Joe Coventry, Referee, Australian National University, Australia
Dr. Marcelino Sanchez Gonzalez, Referee, CENER, Spain
Dr. Marco Binotti, Politecnico di Milano, Italy
Dr. Roberto Bonifetto, Politecnico di Torino, Italy
Dr. Marco Simonetti, Politecnico di Torino, Italy
Dr. Luca Turchetti, ENEA, Italy

Politecnico di Torino
July 2024

I hereby declare that the contents and organisation of this dissertation constitute my own original work and does not compromise in any way the rights of third parties, including those relating to the security of personal data.

Mehdi Shokrnia Turin, July 2024

To my beloved parents, whose unwavering love sustains my journey.

Acknowledgment

I would like to express my deepest gratitude to my supervisors, Professor Roberto Zanino and Dr. Mattia Cagnoli, for their expert guidance and insightful feedback, which have been crucial to the completion of this thesis.

Special thanks to my colleagues from ENEA: Antonio D'Angelo, Walter Gaggioli, Roberto Grena, Michela Lanchi, Raffaele Liberatore, and Valeria Russo, for their collaboration and assistance.

I am also grateful to my colleagues in the NEMO group at Politecnico di Torino, especially Dr. Roberto Bonifetto and Dr. Antonio Froio, for their support during my PhD program.

Immense gratitude to my beloved family, especially my dear parents, whose endless love and support have been invaluable in my life.

I am profoundly grateful to my girlfriend, Zahra, whose love and understanding have been a source of strength and motivation throughout this process.

Lastly, I would like to thank all my friends for their companionship during these years.

Summary

Concentrated solar power (CSP) technology has captured significant attention over recent decades due to its capability to provide large-scale, renewable energy with the advantage of thermal energy storage, which allows for a dispatchable power production. In this context, this dissertation investigates computationally various features of CSP systems, aiming at introducing specific strategies for the enhancement of overall efficiency and sustainability. This investigation is conducted through three main activities: the optimization of the photo-thermal performance of a parabolic trough system, the comparative techno-economic assessment of various linear CSP technologies, and the thermal performance enhancement of a case study thermocline thermal energy storage system.

The first objective of this dissertation is to propose a new strategy to optimize the photo-thermal performance of a parabolic trough system, through arranging multiple selective coatings along the collector line. This optimization is based on a lumped-parameter model in the radial direction and a 1D model in the axial direction of the receiver tube, which was newly developed for that purpose. Consequently, the most photo-thermally efficient configuration of the receiver tube is presented, characterized by three different selective coating formulations implemented at the three different temperature ranges expected along the receiver. This optimized configuration improves the overall photo-thermal efficiency of the system, in comparison with the single-coated collectors. Moreover, this approach could reduce the receiver cost, owing to the employment of the more expensive selective coating only at the final collector segment.

The second goal of this dissertation involves conducting a comparative techno-economic feasibility assessment among various linear CSP technologies, encompassing evacuated and non-evacuated configurations of linear Fresnel and parabolic trough systems. This comparison is carried out in terms of levelized cost of electricity (LCOE), considering four different locations worldwide characterized by various levels of direct normal irradiation (DNI). The LCOE is determined by cost data and net annual energy yield of the CSP plant. While cost data is collected from existing literature, net annual energy yield is computed by a 1D axial model. This model is supported by an optical ray-tracing model and a radial lumped-

parameter model. In addition, a 2D steady-state computational fluid dynamics (CFD) model is developed in the case of the linear Fresnel receiver unit, where conventional correlations are not applicable for the convective heat transfer between the glass tube and the environment. Furthermore, a sensitivity analysis is performed to evaluate the effect of diverse techno-economic parameters on the LCOE.

Finally, this dissertation aims at enhancing thermal performance of a case study thermocline energy storage system. This improvement is achieved by geometric modifications and phase change material (PCM) integration through different scenarios. A transient 2D CFD model is developed to compute heat losses and temperature distribution within storage tanks. This model is coupled with a PCM lumped-parameter model to compute the PCM temperature and the corresponding heat transfer coefficient. By using these models, the thermal performance of various configurations is investigated for charge and discharge processes. Consequently, a comparative performance analysis is conducted between the proposed energy storage systems and the case study.

Contents

List of Figures

List of Tables

Chapter 1

Introduction

1.1 The global energy context

Addressing the global energy crisis is undoubtedly a significant challenge for communities nowadays. With regard to the global population growth, economic development and technological advancements, the demand for energy has increased considerably over the last few decades [1,2]. However, this rise in the energy demand has always been linked with environmental consequences, especially due to the widespread consumption of fossil fuels. The combustion of fossil fuels releases carbon dioxide and other greenhouse gases into the atmosphere, leading to major environmental issues such as global warming and air pollution [3,4]. Furthermore, the depletion of fossil fuels over a long period could be a serious concern [5]. Consequently, transforming energy systems into clean energy technologies is essential [6,7].

According to the stated policies scenario (STEPS), which provides a projection of energy economy based on the actual status in different regions worldwide [8], fossil fuels have been losing the energy market to clean energy resources in recent years. Figure 1.1 shows the consumption of fossil fuels including natural gas, oil and coal from 2000 to 2050. According to Figure 1.1, a remarkable growth can be observed in the consumption of fossil fuels by 2020. However, each of the three fossil fuels are projected to reach a peak in the timeframe from 2020 to 2030. In the case of coal, a substantial drop is expected due to its massive adverse impacts. Moreover, the use of natural gas and oil will decrease moderately, to be replaced with clean energy technologies [9].

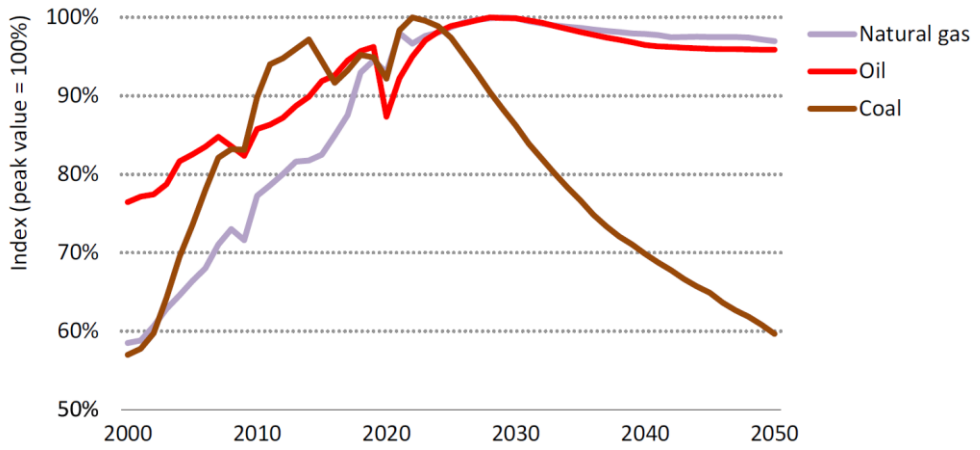

Figure 1.1: Fossil fuel consumption worldwide from 2000 to 2050, normalized to the respective peak [9].

The downward trend of fossil fuels consumption could also be observed in the projection of electricity generation. As outlined in Figure 1.2, total share of the fossil fuels in the global electricity generation will drop dramatically by 2050 in advanced economies, while a significant increase is expected for renewable power production. Regarding developing economies, although a relatively upward trend of electricity generation using fossil fuels is expected by 2050, a much more remarkable rise is anticipated in the share of renewable energy. The share of coal, as an extremely detrimental energy source, in total power production will decrease sharply by 2050 in both communities. Figure 1.2 also reveals that global electricity demand will increase by 80% from 2020 to 2050. Consequently, this higher demand is planned to be supplied mainly by renewable energy sources [10].

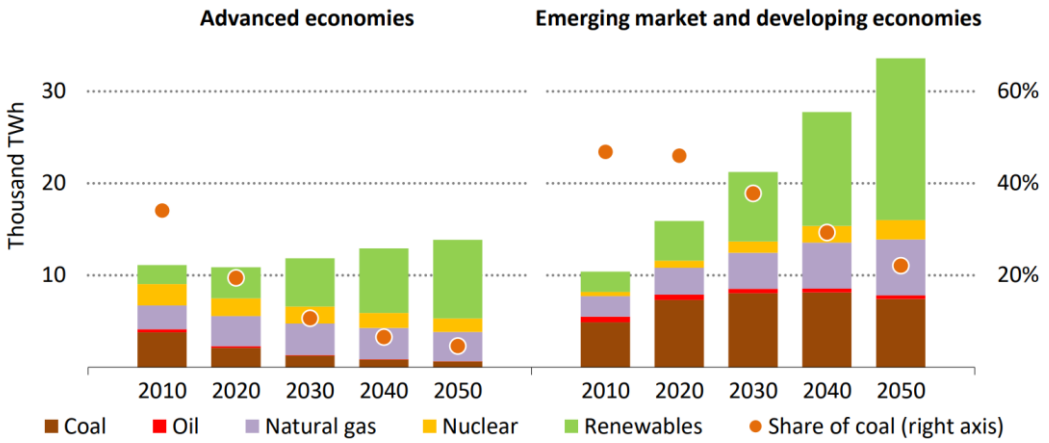

Figure 1.2: Global electricity generation using different resources from 2010 to 2050 in advanced and developing economies [10].

Huge declines in the use of fossil fuels as well as massive deployment of renewable energy technologies, as shown in Figure 1.2, paves the way for achieving the net zero emissions (NZE) initiatives [11]. The NZE scenario aims at reducing greenhouse gas emissions to attain net-zero emissions globally by 2050 [12]. This is necessary for limiting the global warming to 1.5 °C, as planned in the Paris Agreement on climate change, established in 2015 [13]. Based on the NZE scenario, global CO_2 emissions fall to around 21 Gt by 2030 and to net zero by 2050, as depicted in Figure 1.3. Although CO_2 emissions reach net zero by around 2045 in advanced economies, it is expected to achieve this goal by 2050 in emerging market and developing economies [14].

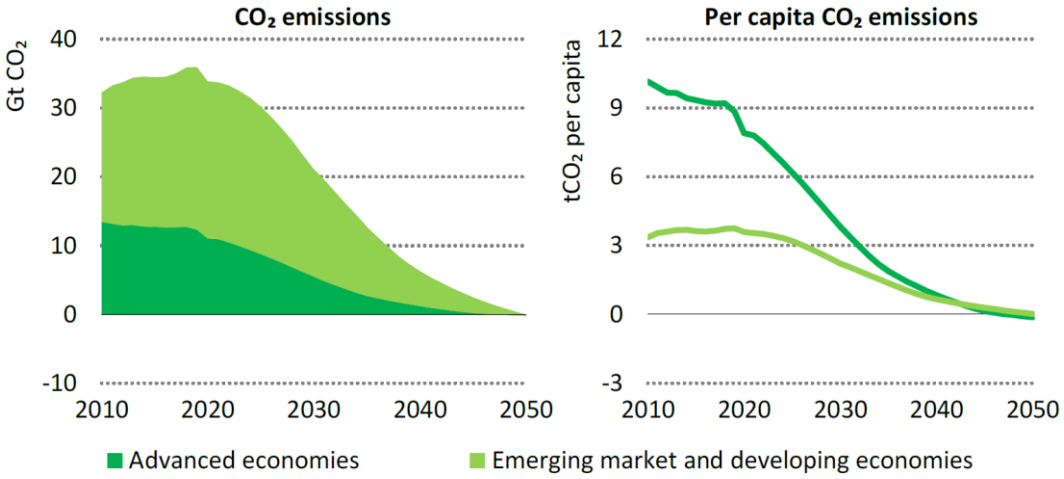

Figure 1.3: Global net CO_2 emissions from 2010 to 2050 in advanced and developing economies [14].

According to the NZE scenario, renewable energy sources replace the majority of the share of fossil fuels by 2050 in terms of total energy supply worldwide, as shown in Figure 1.4; the share of fossil fuels drops from about 80% in 2020 to about 20% in 2050. Furthermore, despite economic and population growth, total global energy supply starts decreasing after around 2020, which is caused by improvements in the energy systems efficiency. Figure 1.4 also reveals that a considerable share of the renewable energy in 2050 will be associated with solar energy, while this share indicates a massive increase from the current status in 2024 to the projection in 2050 [10].

Section 1.2 highlights bright prospects of solar energy within the broader context of renewable energy, representing the concentrated solar power (CSP) as a promising technology.

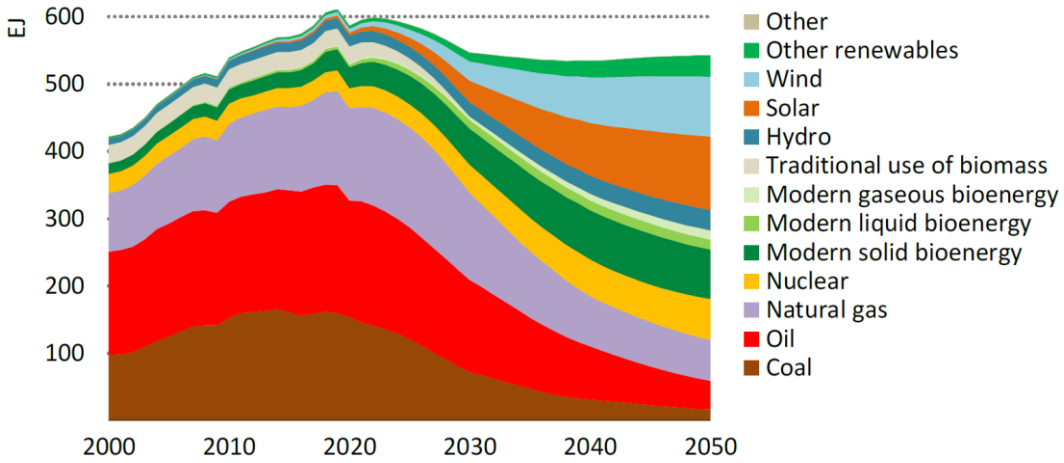

Figure 1.4: Global energy supply using different resources from 2000 to 2050 [10]

1.2 Solar energy: the concentrated solar power (CSP) perspective

Solar energy represents a clean, sustainable and abundant source of energy. The amount of sunlight available on the Earth's surface far exceeds the global energy demand. It has been claimed that within 6 hours deserts receive more energy from the sun than humankind consumes within a year [15]. Figure 1.5 outlines daily and yearly direct normal irradiance (DNI) available in different regions worldwide. As can be observed, extensive regions in the world are characterized by abundant sunlight with a yearly DNI of over 2000 kWh/m^2, demonstrating great potential of solar energy for power production on a large scale [16].

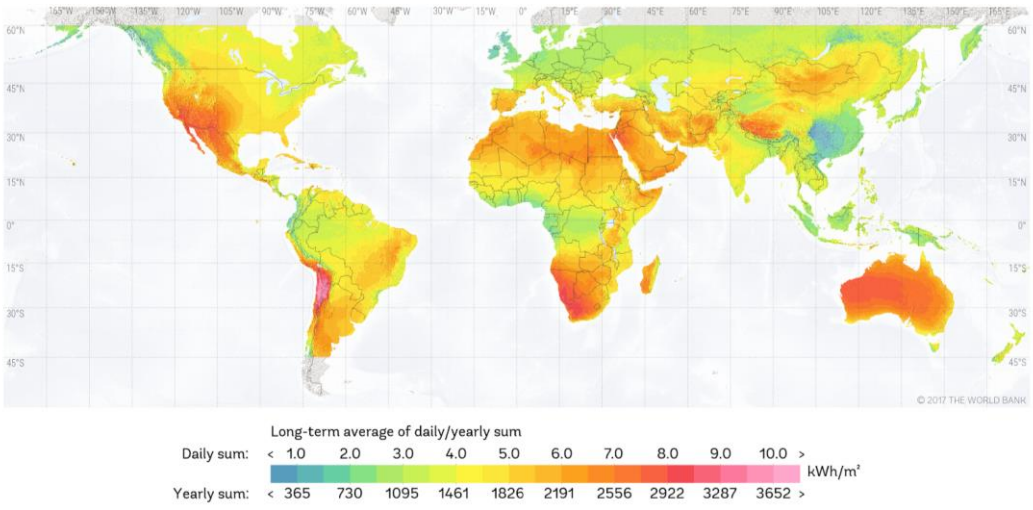

Figure 1.5: Available daily and yearly DNI across various global regions [16]

Solar energy can be harnessed through various technologies: photovoltaics (PV) that directly convert sunlight into electricity [17,18]; CSP that concentrates sunlight by means of mirrors to collect solar thermal energy for driving utility-scale electric turbines [19,20]; and heating/cooling systems that utilize solar thermal energy to provide hot water and air conditioning [21,22].

Among solar-based technologies, the CSP system has attracted substantial attention over recent decades, mainly owing to the capability of storing thermal energy, leading to a dispatchable power production [23]. This technology indicates a significantly positive outlook, as shown in Figure 1.6. According to the STEPS, which is based on the current policy landscape, the installed capacity of the CSP increases notably from 6 GW in 2019 to 55 GW in 2040. This rise is even more remarkable in the sustainable development scenario (SDS), which introduces necessary measures to achieve sustainable energy objectives, encompassing the Paris Agreement, air quality and energy access [12]; based on the SDS, the installed capacity of the CSP is projected to reach 253 GW by 2040 [24].

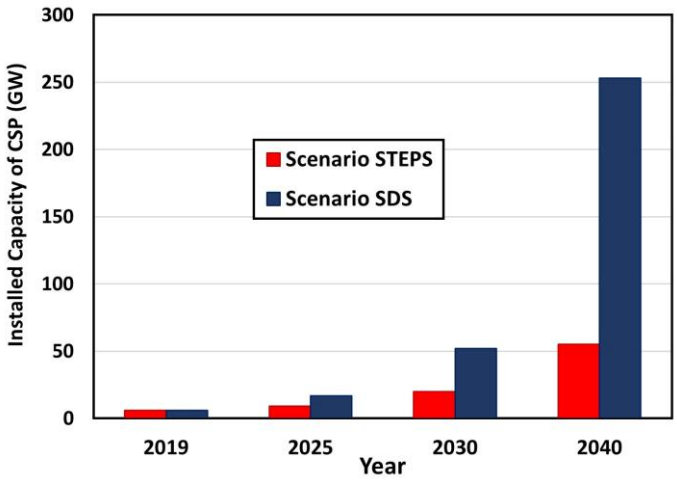

Figure 1.6: The CSP perspective by 2040 considering the STEPS and the SDS scenarios [24].

As mentioned, the CSP technology offers a major advantage by providing dispatchable power. The possibility of thermal energy storage in the CSP systems allows for adjusting power generation based on fluctuations in demand, enhancing flexibility within the energy network. Moreover, this feature ensures the long-time stable power output even during low solar radiation or during the night, despite some other renewable sources like PV and wind that cannot provide stable power because of the absolute dependence on the environmental conditions [23,25].

Figure 1.7 compares different renewable sources in terms of levelized cost of energy considering 24-hour dispatchability. As shown, the energy cost of the CSP technology could be competitive with other renewable sources. Among renewable technologies possessing the advantages of dispatchability and storage possibility while benefiting from abundant resources, CSP emerges as particularly promising. Although PV and wind are supplied by abundant renewable sources, they must be integrated with other technologies to generate dispatchable power, which mostly leads to a significant increase in the cost. On the other hand, more economical technologies with dispatchability and storage potential like biomass and geothermal lack the advantage of plentiful sources such as wind and solar energy [26].

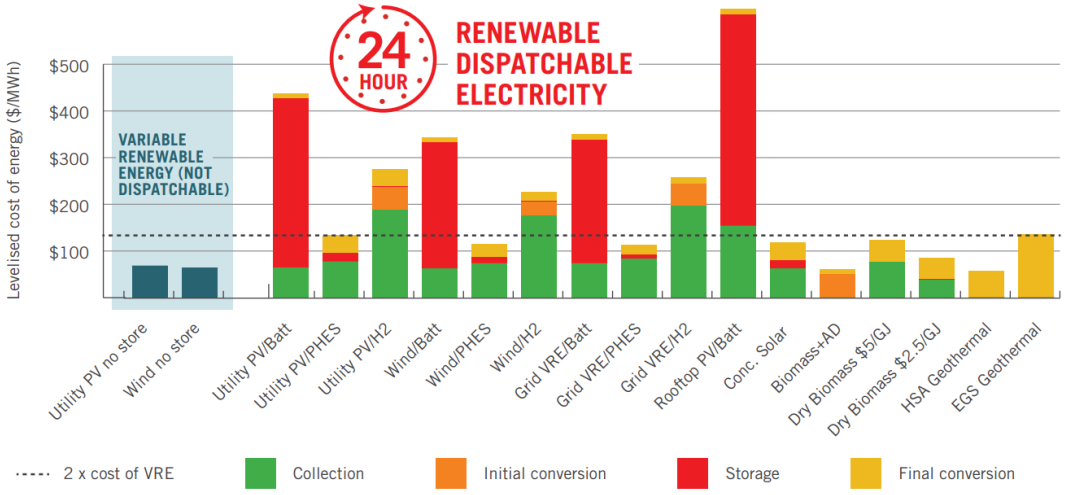

Figure 1.7: Comparison among different renewable technologies in terms of levelized cost of energy considering 24-hour dispatchable electricity production [26].

Consequently, harnessing solar energy by the CSP technology could be a viable solution to meet growing energy demands while addressing the challenges caused by the climate change. The unique advantages associated with the CSP technology, as mentioned above, have been the primary motivation for this thesis. In this respect, the present thesis endeavors to investigate diverse features within CSP systems, aiming at presenting potential opportunities for the enhancement of system efficiency and sustainability.

1.3 Structure and objectives of the thesis

In the context of the CSP technology, this thesis aims to introduce specific strategies for improving system performance and reducing costs, thereby increasing its competitiveness compared to other renewable systems. For this purpose, two

critical components of linear CSP technologies including receiver tube and storage unit have been investigated to propose solutions for enhancing the overall performance of the system and minimizing expenses. In addition, a techno-economic assessment of various linear CSP technologies has been carried out to provide detailed guidelines for the selection of the most profitable technology.

In this respect, the primary goal of this thesis is to optimize the photo-thermal efficiency of a parabolic trough system by implementing multiple selective coatings along the receiver tube. This strategy facilitates determining the most enhanced configuration of the receiver tube from a photo-thermal perspective through providing the spatial distribution of the selective coatings.

Furthermore, this study aims to perform a comparative techno-economic feasibility assessment among various linear CSP technologies, including evacuated and non-evacuated configurations of linear Fresnel and parabolic trough systems. This comparison is conducted in terms of levelized cost of electricity (LCOE) considering four locations worldwide characterized by various levels of DNI. For this purpose, net annual energy yield is calculated for different scenarios through an annual-based thermal analysis.

Additionally, the thesis intends to enhance the thermal performance of a thermal storage system through specific measures, encompassing geometric modifications and incorporation of latent heat into the system through different scenarios. This objective involves a comprehensive comparative study to evaluate the impacts of the adopted strategies.

To achieve the outlined research objectives, the thesis is organized in six chapters. After representing the global energy perspective in the current chapter, the following chapters delve into diverse features of CSP technology:

- Chapter 2 provides a comprehensive review of relevant literature and background knowledge in the context of the CSP technology. Initially, a general outline of the CSP technology is presented, followed by a detailed investigation of linear CSP systems. Subsequently, various energy storage mechanisms including sensible and latent heat storage are explored.
- Chapter 3 represents the photo-thermal optimization of a parabolic trough system. In this regard, the reference system and the methodology employed for the optimization purpose are explained. Then, two developed models are presented, along with the corresponding validation. Finally, results of the photo-thermal optimization are provided.

- Chapter 4 conducts a comprehensive comparative techno-economic assessment of parabolic trough and linear Fresnel collectors, considering evacuated and non-evacuated receiver tubes. Following the description of reference systems and the methodology implemented, optical and thermal models developed to obtained net annual energy yield are presented. Finally, a comparative economic analysis is carried out based on the LCOE, comprising a sensitivity study of various parameters.
- Chapter 5 introduces enhanced configurations of a case study energy storage system through geometric modifications and latent heat integration. Initially, the case study is presented, followed by describing the improvement strategies. Subsequent sections delve into the numerical modelling of the system, providing model validation. The chapter concludes with a comparative performance analysis among various energy storage systems under investigation.
- Chapter 6 summarizes key findings of the dissertation while proposing prospects for future research works.

Chapter 2

Background

2.1 Overview of CSP technologies

CSP technologies can be classified into two main categories: line-focusing systems, encompassing parabolic trough collector (PTC) [27] and linear Fresnel collector (LFC) [28], and point-focusing systems, which include solar power tower (SPT) [29] and parabolic dish collector (PDC) [30]. Schematics of various CSP technologies are shown in Figure 2.1.

Among the line-focusing CSP systems, the PTC is composed of parallel rows of long parabolic mirrors (Figure 2.1a), while in the LFC, the parabolic mirror is replaced with a series of curved or nearly flat mirror stripes (Figure 2.1c). Both these systems concentrate solar radiation over a focal line, where the receiver tube is located. In the case of the LFC, a secondary concentrator is also mounted above the receiver tube to allow for reconcentrating the solar radiation that misses the receiver. In the typical configuration of the single-tube receiver unit of an LFC system, the secondary concentrator is a compound parabolic concentrator (CPC) [31,32]. While the simple and low-cost design of the LFC results in significant economic advantages, this technology indicates lower optical efficiency compared to the PTC [33,34]. Currently, the PTC power plants constitute the largest share of the installed CSP plants worldwide, accounting for about 76% of the current share of CSP capacity. In contrast, the LFC is attributed to only 2% of the overall CSP market [35,36].

Among the point-focusing CSP systems, the SPT consists of a large number of mirrors called heliostats, which focus highly concentrated solar irradiation onto a central receiver located atop a tower [37] (Figure 2.1b). This technology is considered the most prospective solution for future CSP plants, mainly because of the capability to achieve very high concentration ratios [38]. Currently, the SPT plants account for about 21% of the CSP industry [36]. Another point-focusing CSP system is the PDC, in which the sunlight is concentrated onto a receiver placed at the focal point of the dish [39] (Figure 2.1d).

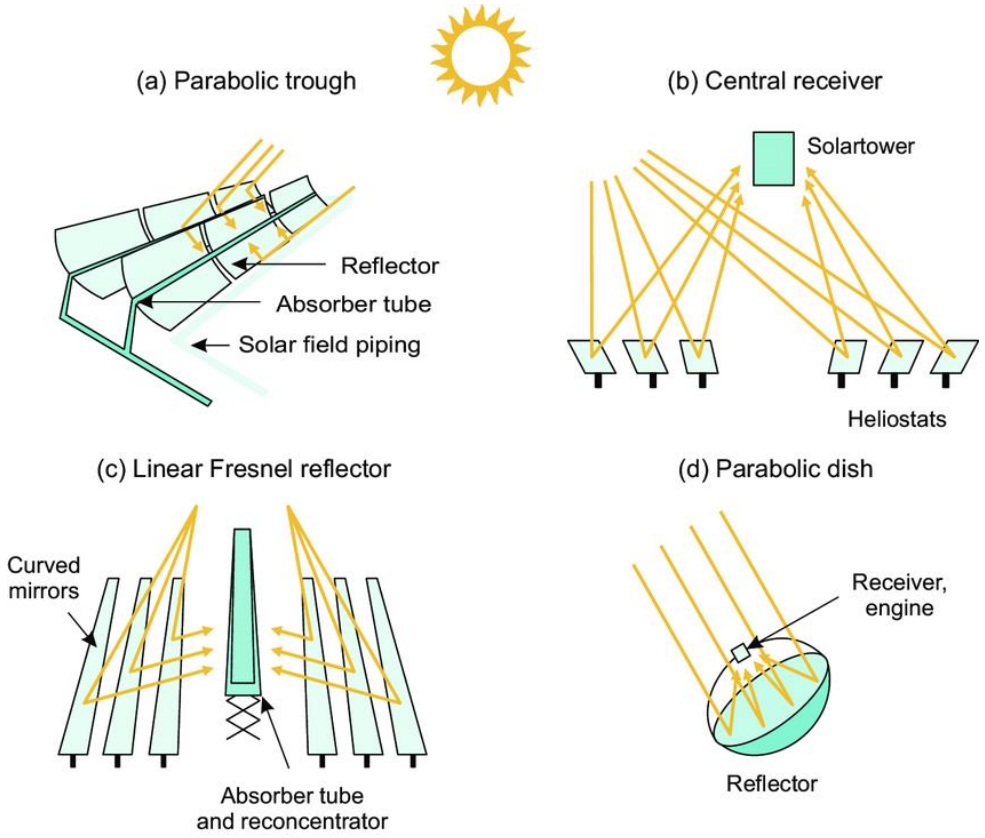

Figure 2.1: Schematics of classical CSP technologies [40]

CSP systems can be employed for various applications such as power generation [41,42], industrial heating [43], seawater desalination [44,45], residential heating/cooling [46], and hydrogen production [47]. A schematic of a typical CSP plant is depicted in Figure 2.2. As shown, a CSP plant encompasses three main parts: solar field, thermal energy storage (TES) unit and power block. The solar field, comprising mirrors, receiver unit, support structures, tracking system and heat transfer fluid (HTF), serves as the heart of the plant to heat the HTF

by concentrating direct solar radiation. In the typical configuration of a commercial CSP plant based on parabolic trough technology, synthetic oil is employed as the HTF. A heat exchanger (HX) is also utilized to transfer heat from the hot HTF available at the outlet of the solar field to the working fluid of the power block, which typically is organic Rankine cycle (ORC). Finally, this hot working fluid is exploited to generate electricity using a turbine. In some CSP plants, the HTF of the solar field and the working fluid of the power block are the same. Hence, the HTF directly passes through the turbine. However, during favorable solar radiation conditions, the thermal energy generated by the solar field may not be processed immediately in the power block. Alternatively, it could be stored in the TES unit to be utilized for additional power production during limited solar radiation availability or during the night. As shown in Figure 2.2, the TES unit consists of hot and cold storage tanks and heat storage medium (HSM). In this thesis, molten salt has been considered as the HTF for solar field since it can reach higher temperatures compared the oil, leading to higher efficiencies. Regarding the TES unit, a single-tank thermocline storage system has been employed due to its lower investment cost in comparison with the two-tank system [48,49].

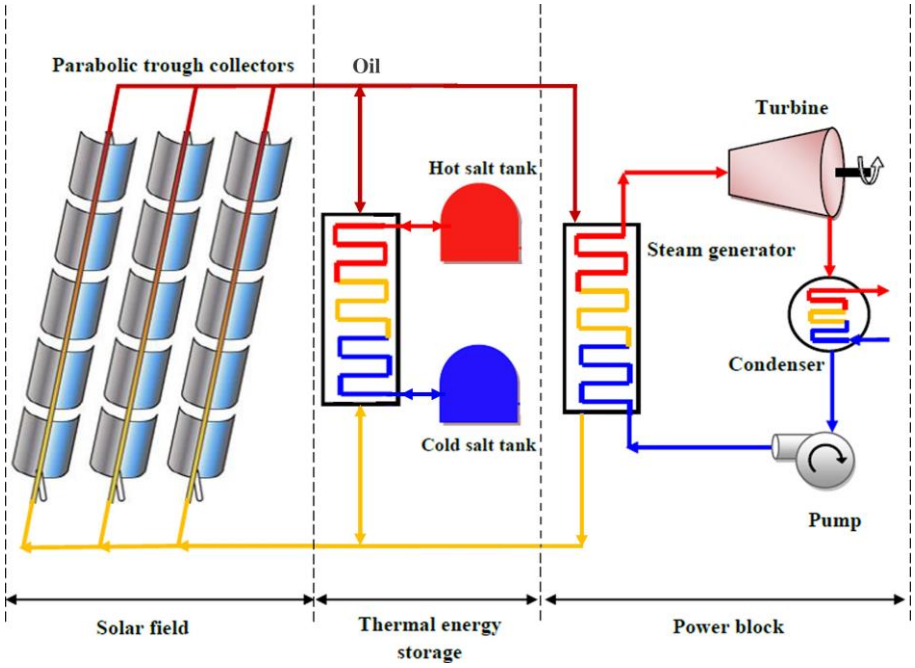

Figure 2.2: Schematic diagram of a CSP plant [48]

In the subsequent sections, a detailed overview of various aspects of the CSP technology examined in this thesis is provided, including a comprehensive review of the relevant literature. In this regard, Section 2.2 investigates diverse features of

line-focusing CSP systems encompassing the PTC and the LFC. Then, Section 2.3 presents different TES technologies, focusing on thermocline energy storage system.

2.2 Linear CSP systems

As mentioned, linear CSP technologies include the PTC and the LFC. In a PTC system, a parabolic mirror is employed to concentrate the incident solar radiation onto the focal axis, where the receiver tube is positioned to transfer the thermal energy of the concentrated sunlight to the HTF [50]. Figure 2.3 displays a schematic of the cross-sectional view of a PTC receiver tube. As shown, the receiver tube is composed of an absorber tube encapsulated in a glass cover. A HTF flows through the absorber tube to absorb the concentrated thermal energy. Thermal oil, steam and molten salt are prevalently employed as the HTF in the linear CSP systems [51,52]. The glass cover has the function of minimizing convective and radiative heat losses to the environment since it not only protects the receiver tube against wind effects but also is opaque in the infrared. A selective coating is typically implemented on the outer surface of the absorber tube to improve the photo-thermal performance of the collector through minimizing the emissivity and maximizing the absorptivity. The gap region between the absorber tube and the glass envelope is typically kept under vacuum conditions. This evacuation would result in a significant reduction in the convective heat loss from the absorber tube and would protect the selective coating from the air, as these coatings could be degraded in the presence of the air after several hours of use [53,54].

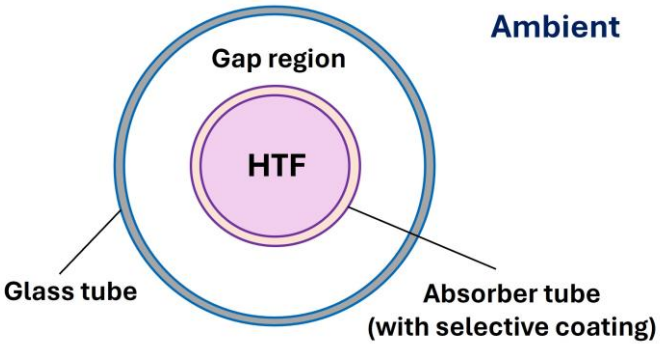

Figure 2.3: Cross-sectional view of a PTC receiver tube [55]

Another line-focusing CSP technology is the LFC, in which curved or nearly flat mirrors are utilized to concentrate the incident solar radiation onto the receiver unit. The conventional receiver unit of the LFC consists of a receiver tube coupled

to a secondary concentrator, as shown in Figure 2.4a. In this configuration, while the receiver tube is usually the same as that of the PTC, the secondary concentrator is an open cavity, typically a CPC.

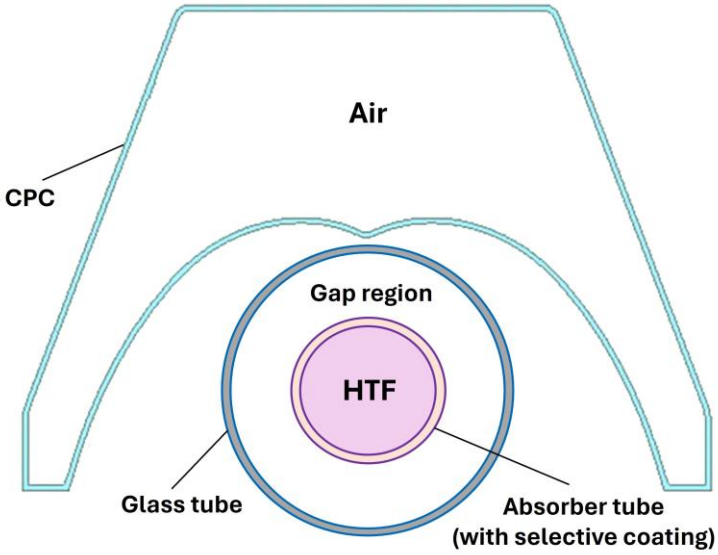

(a)

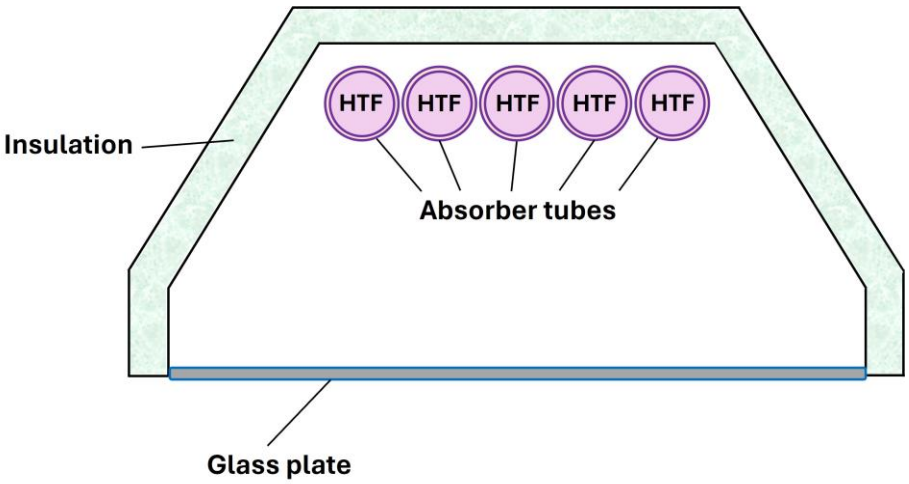

(b)

Figure 2.4: Cross-sectional view of conventional LFC receiver units: (a) single-tube configuration with a CPC secondary reflector, and (b) multi-tube trapezoidal cavity configuration [56–58].

Many investigations have been conducted to introduce alternative shapes for the secondary concentrator or to optimize the CPC geometry. In this respect, several configurations such as double CPC receiver [59], simultaneous multiple surfaces [60], and segmented parabolic concentrator [58] were proposed.

Another conventional design for the LFC receiver unit is the multi-tube trapezoidal cavity receiver, as illustrated in Figure 2.4b. In this configuration, multiple absorber tubes are placed within a trapezoidal cavity, which is closed at the bottom by a glass plate. The cavity is insulated, while the space between the glass window and the absorbing surface is not vacuum, but filled with a gas (typically nitrogen) at 1 bar [61]. Some studies have also suggested trapezoidal cavity receivers with a single tube [62,63], or less common configuraions like inverted flat plate collector [64], multi-tube V-cavity receiver [65], and triangular receiver [66].

In the next sections, a comprehensive review of the relevant literature is provided for various aspects of linear CSP systems investigated in the present thesis, comprising heat transfer in the LFC receiver unit (Section 2.2.1), enhancement of selective coatings (Section 2.2.2) and comparative techno-economic analysis of linear CSP technologies (Section 2.2.3).

2.2.1 Heat transfer in a linear Fresnel collector receiver unit

While investigation of heat transfer phenomena in the case of the PTC receiver tube is not challenging due to the availability of correlations in the literature for cylinder in cross flow [67], presence of the secondary concentrator in the case of the LFC receiver unit necessitates developing ad-hoc correlations. In fact, it is expected that the secondary concentrator would perturb the external air flow around the receiver tube, potentially reducing the convective heat loss. Several studies have been carried out to explore heat transfer phenomena in the LFC receiver unit. Pye et al. [68] investigated unsteady flow patterns in the trapezoidal cavity of an LFC with a multi-tube receiver. According to the results of computational fluid dynamics (CFD) simulations, a correlation was derived for the Nusselt number based on the Grashof number, cavity depth and width. Moreover, Natarajan et al. [69] developed a 2D steady-state laminar CFD model to investigate combined natural convection and radiation in a trapezoidal cavity of a multi-tube LFC. Then, a correlation was proposed based on the results obtained for the Nusselt number by the numerical simulation. The correlation was a function of Grashof number, surface emissivity, aspect ratio, absorber angles, temperature ratio and radiation-conduction number.

Moving to the single-tube configuration, Guadamud et al. [70] developed a 3D unsteady CFD model to study heat transfer phenomena in an LFC receiver. They obtained the azimuthal distribution of the Nusselt number on the receiver tube for only one specific condition. Therefore, no correlations were proposed for the Nusselt number.

In addition, Cagnoli et al. [71] developed 2D and 3D CFD models for a single-tube LFC receiver unit to evaluate heat losses from the absorber tube to the ambient for natural and forced convections. It was found that the wind effect on the receiver performance is not considerable, regardless of wind direction and intensity, due to the shielding effect of the secondary concentrator. Nevertheless, no correlations were proposed for the Nusselt number.

Therefore, reviewing the literature proves that no correlations have been established for the Nusselt number in the case of the single-tube LFC with a CPC secondary concentrator. The present thesis focuses on this problem to provide two ad-hoc correlations applicable for natural and forced convections (refer to Section 4.5.3).

2.2.2 Enhancement of selective coatings

Selective coatings play a key role in the overall performance of the linear CSP systems. Therefore, development of optimized selective coatings is of great importance. Various optimization strategies have been proposed by numerous research works through the enhancement of the specifications or the configuration of the coating applied to the absorber tube (Section 2.2.2.1). Additionally, development of air-stable selective coatings for the non-evacuated receiver tubes has captured attention during the last few years, as these tubes could be an alternative solution to address the challenge of maintaining evacuation within the receiver tube (Section 2.2.2.2).

2.2.2.1 Optimization of photo-thermal performance

The photo-thermal efficiency of a solar collector represents a metric to evaluate collector effectiveness in converting solar radiation into useful thermal energy (see Section 3.6). Many investigations have been carried out on the photo-thermal enhancement of PTCs through implementing specific strategies on selective coatings. Olson et al. [72] introduced enhanced configurations of a direct steam generation PTC by optimizing environmental, spectral and material properties of selective coatings. For this purpose, several parameters were investigated, including

emissivity, absorptivity, transition wavelength, transition length, concentration factor and operating temperature. Then, optimized selective coatings were represented with respect to these parameters for ideal and realistic non-ideal conditions. Esposito et al. [73] implemented specific optimization approaches to develop cermet-based selective coatings for high temperature applications up to 580 °C. In this regard, six optimized selective coatings were introduced by adopting a layer-on-layer ellipsometric characterization and a semi-empirical approach. According to the results, the developed selective coatings could demonstrate enhanced performance compared to similar selective coatings, indicating a photo-thermal efficiency of 85% at 550 °C. °C. In addition, Yang et al. [74] performed a spectral optimization of selective coatings designed for PTCs, exploring the influence of solar irradiation flux and absorber temperature on coating spectrum distribution and overall efficiency. It was observed that a uniform distribution of solar irradiation flux and absorber temperature would result in optimal selective coatings. Conducting a spectral absorptivity analysis confirmed that the absorptivity of selective coatings has nearly equal positive impact on the receiver performance at various temperatures, while an emissivity analysis revealed varied negative effect with respect to temperature. Consequently, it was concluded that spectral emissivity plays a vital role in optimizing selective coatings at high temperatures. However, all these studies optimized the photo-thermal performance of PTC systems by improving selective coating specifications. In the present study, a different technique has been applied, in which multiple selective coatings are arranged along the collector line based on their photo-thermal performance.

Furthermore, Yang et al. [75] proposed a novel configuration of the PTC receiver, namely double-selective-coated receiver. For this purpose, the receiver was split into two zones to apply two different selective coatings based on the circumferential distribution of solar flux on the absorber tube, as shown in Figure 2.5. Performing a cut-off wavelength optimization for the proposed receiver reported distinct optimum optical properties for the two zones. Then, the double-selective-coated receiver was compared with two traditional single-coated receivers. It was stated that the proposed receiver could decrease heat losses from the absorber tube to the external ambient and enhance the photo-thermal efficiency, in comparison with the two traditional single-coated receivers. Yang et al. [76] also carried out a spectral-spatial analysis of the same PTC receiver tube. They claimed that the proposed configuration could decrease heat losses and improve the photo-thermal efficiency of the system. However, in these works, the distribution of the two selective coatings was considered in the circumferential direction, instead of the axial direction.

In addition, Zhao et al. [77] adopted a strategy involving the application of multiple coatings in various segments of a PTC system. In this respect, two configurations were proposed: a multi-section receiver with multiple practical selective coatings, and an ideal receiver encompassing multiple selective coatings with optimum cut-off wavelengths at various temperatures. According to the results, both proposed configurations indicated enhanced thermal performance compared to a conventional single-coated receiver in terms of thermal efficiency and heat loss.

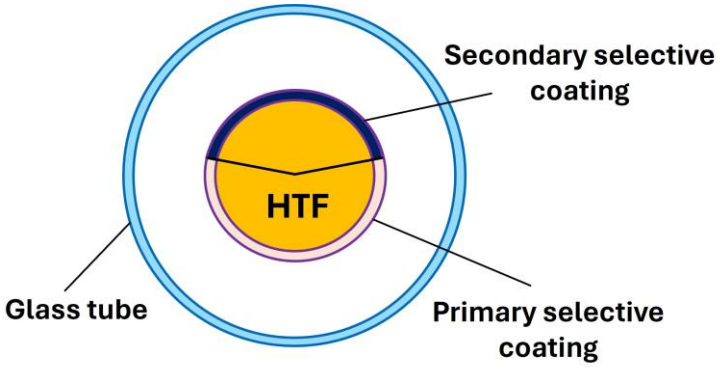

Figure 2.5: Schematic of the double-selective-coated receiver tube, proposed by [75,76].

Moreover, Singh et al. [78] presented a performance enhancement approach for the PTC receiver tube through applying a MXene-based coating, and proposed two retrofitted coated absorber tubes. The results showed that the proposed coating technique could improve the thermal efficiency of the absorber tube compared to a conventional selective coating. Accordingly, employing a retrofitted coated absorber tube could result in a reduced collector size. Additionally, Stanek et al. [79] pursued the strategy of applying a non-selective coating to the initial segment of a PTC receiver tube to decrease the investment cost of the system. The concept of the suggested configuration is displayed in Figure 2.6. Four case studies were investigated in the analysis considering various temperature ranges of solar industrial applications. The suggested strategy demonstrated a great potential for deployment in low-temperature and medium-temperature applications. Nevertheless, it could not be applied to high-temperature systems because of high heat losses and limited potential for improvement. However, an optimization based on the photo-thermal efficiency is absent in all the above-mentioned works. Furthermore, an optimal configuration of the PTC receiver indicating spatial distribution of selective coatings along the absorber tube was not presented.

2.2.2.2 Coatings for non-evacuated receiver tubes

The most critical issue related to the non-evacuated receiver tubes from a technical viewpoint is the stability of selective coatings in air at high temperatures. A few studies have been conducted to evaluate and enhance the stability of selective coatings at medium-high temperatures in the air after many hours of use. For instance, Raccurt et al. [80] evaluated stability of a selective solar absorber coating exposed in air under high temperatures up to 500 °C. The degradation process at higher temperatures was investigated and the results proved that the coating has a good resistance to the oxidation. The material was stable up to 450°C during 3000h without change in the absorptivity and emissivity, while at 500 °C the optical properties started to degrade after 1000h.

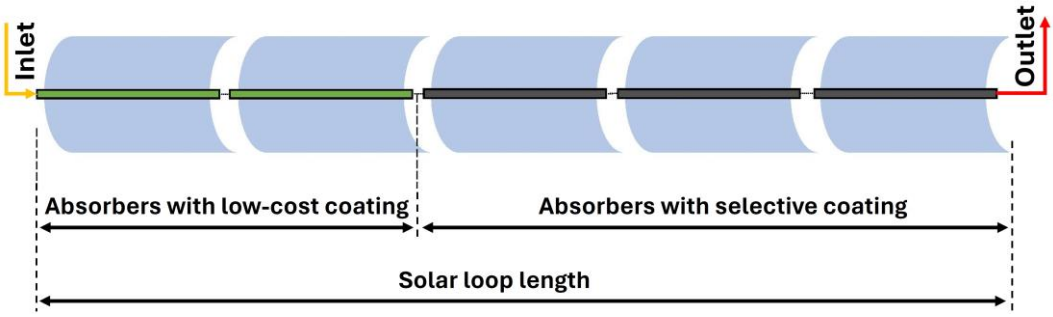

Figure 2.6: A configuration of the PTC proposed by [79]*, aimed at reducing the investment cost.*

Furthermore, Wang et al. [81] adopted a quantitative design approach to introduce an air-stable manganese-iron oxide nanoparticle-pigmented selective coatings for CSP applications operating at high temperatures (up to 750 ℃). It was claimed that the absorptivity of the developed coating could reach about 93%, while the optical-to-thermal energy conversion efficiency was 89.7% after exposure to air at 750 ℃ for 700 h. These results demonstrated a considerable improvement compared to the non-selective benchmark Pyromark 2500 coatings that showed degradation at 750 ℃ in air. However, after 1000 hours of working, a thermal degradation was observed in the newly developed coating. Recently, Rossi et al. [54] developed new spectrally selective coatings for the linear CSP systems operating in air at high temperatures (up to 600 ℃). As depicted in Figure 2.7, these coatings were composed of different functional elements considering stainless steel as a substrate as well as back reflector, absorber and two antireflection layers, respectively. The coatings demonstrated favorable thermal and optical stability with slight variations in the optical properties after over 2000 hours of exposure to air at

600 °C. The study reported the absorptivity of 73% and 87% and emissivity of 18% and 27% for aged coatings obtained through thermal oxidation and sputtering process, respectively.

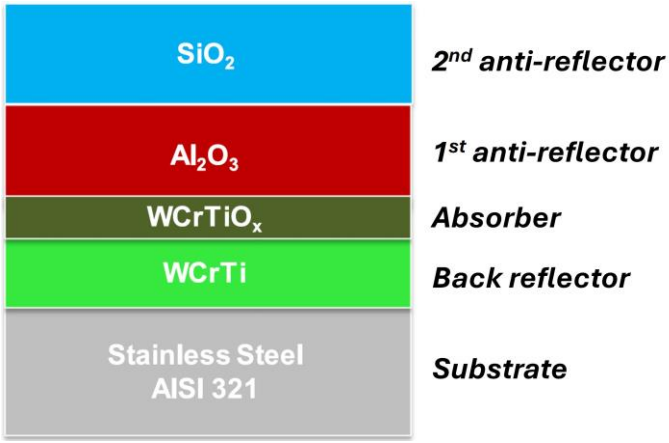

Figure 2.7: Scheme of the multilayer structure for an air-stable selective coating, developed by [54].

In this thesis, a selective coating under development at ENEA (AIR PLUS coating) has been considered for the non-evacuated receiver tubes to perform a techno-economic comparison among various configurations of the linear CSP technologies (see Section 4.2).

2.2.3 Comparative techno-economic analysis

As mentioned, while the LFC benefits from a low-cost design, it offers lower optical performance compared to the PTC. Furthermore, although evacuating the receiver tube facilitates reaching higher thermal efficiency, it involves an additional expenditure. Thus, conducting annual-based optical, thermal and economic analyses is essential for making a fair comparison among different configurations of the linear CSP technologies. In this regard, Morin et al. [33] conducted a comparative analysis among a reference evacuated PTC and different configurations of evacuated and non-evacuated LFCs in terms of thermal and optical efficiencies as well as electricity generation costs. For this purpose, an LFC receiver tube with a 7 cm diameter was compared to that with a larger diameter (14 cm), and it was found that smaller receiver designs would be more efficient. Additionally, although the LFC technology demonstrated lower optical and thermal efficiencies compared to the PTC, it was concluded that a lower cost per aperture area for the LFC technology could compensate for its lower efficiency.

Nevertheless, the non-evacuated PTC technology was not included in the study, and a glass plate (not a glass tube) was considered at the receiver unit.

Cau and Cocco [82] carried out a comparative thermal analysis between two CSP plants based on PTC and LFC. It was highlighted that, although the LFC plant could generate a higher electricity per unit area of land, the PTC could produce a higher energy per unit area of solar collector due to a higher optical efficiency. Consequently, the PTC plant could provide greater conversion efficiencies. This work was followed by Cocco and Cau [83] to investigate economic implications of the comparison. The economic analysis revealed that the LFC produces energy with a higher cost compared to the PTC. However, these studies focused only on the evacuated configuration of receiver tube, while the non-evacuated configuration was not investigated.

Sait et al. [84] performed a performance/cost optimization on a Fresnel-based modular solar thermal power plant though optical and thermal analyses and compared it with a reference PTC plant. The LFC under investigation encompassed 8 tubes, a glass plate at the receiver bottom and a wedge-type secondary concentrator. Based on the results, the annual solar to electricity efficiency of the LFC plant could be close to the state of the art in PTCs. Additionally, a reduced cost was observed in the LFC compared to the PTC due to lighter structures. This comparison proved that a Fresnel-based solar field could capture solar heat flux for producing a given level of power with about 2/3 of the cost of PTC plants. Nonetheless, configurations of the non-evacuated PTC as well as the LFC with a CPC were not considered in this analysis.

Rovira et al. [85] conducted a comparative annual performance analysis and economic assessment of an integrated solar combined cycles using PTC and LFC. Two locations, Las Vegas and Almeria, were considered for the annual analysis. Results showed that the thermal contribution would be greater with the PTC, while the LFC could enhance the economic feasibility of the plant. Furthermore, Purohit and Purohit [86] evaluated the technical and economic feasibility of CSP technology in India based on solar radiation and land resource assessment. A comparative study was conducted between LFC and PTC technologies and it was reported that the LCOE would be lower by implementing a PTC-based plant compared to the LFC-based one. Then, the most suitable locations for building CSP plants were introduced. Moreover, Bellos [87] investigated the potential of CSP technologies in different Greek locations to determine the most effective scenario. In this regard, LCOE was computed for LFC and PTC technologies considering

hourly meteorological data collected for thirteen locations. The results revealed that the PTC technology could provide lower LCOE compared to the LFC for various yearly DNI values. However, these works did not include non-evacuated configurations in their investigation and focused only on the evacuated receiver tubes.

In addition, several research works have conducted comparisons between evacuated and non-evacuated configurations. Bendato et al. [88] carried out a comparative economic analysis among three single-tube LFC configurations, namely evacuated tube, tube in air with a glass cover and tube in air with a glass plate closing the CPC at the bottom. The study aimed at evaluating the effect of technical solutions on economic performance indicators performed by using regression meta-models based on the theory of response surface methodology. According to the results, the best configuration from an economic viewpoint was found to be the evacuated one. On the contrary, the least effective configuration was determined to be the tube in air with a glass cover. Additionally, Montes et al. [89] performed a comparative thermal and economic study on among three single-tube LFC configurations, namely evacuated tube, non-evacuated tube without a glass and non-evacuated with a glass plate at the bottom. The work focused on the annual electricity cost of the LFC-based plants with hybrid loops. It was stated that simplicity, robustness and lower investment costs required for non-evacuated tubes could compensate for greater heat losses on some occasions. Nevertheless, these studies did not involve the PTC technology in their comparisons and investigated only the LFC system.

Moreover, Cagnoli et al. [71] carried out a comparative thermal analysis between the evacuated and non-evacuated tubes in the context of an LFC system working at relatively low temperatures (180-300 °C). It was demonstrated that the benefit of using the evacuated tube depends on the solar heat absorbed by the receiver unit. A slight difference was observed in the thermal performance between the evacuated and non-evacuated tubes, which was attributed to the relatively low temperature of the receiver. Nonetheless, the work focused only on the LFC, and the PTC was not included in the study. In addition, an economic analysis was not conducted.

Osorio and Rivera-Alvarez [90] proposed a new configuration of the non-evacuated PTC with double glass envelope and compared it with traditional evacuated tubes. In this respect, the thermal and economic performance of the two technologies were assessed based on thermal output per unit cost of the plant. The

results showed that the proposed non-evacuated configuration could present more efficient thermal and economic performance at high operating temperatures compared to traditional evacuated configurations. However, this study did not include the LFC technology in the analysis and investigated only the PTC.

Consequently, it is evident from literature that a comparative techno-economic assessment of the linear CSP systems, encompassing evacuated/non-evacuated PTC/LFC, has not been carried out yet. This dissertation conducts this comparison through investigating annual optical and thermal performance of these four linear CSP configurations (see Chapter 4).

2.3 Thermocline energy storage system

TES is a vital component in a CSP plant since it allows for generating dispatchable power [91,92]. Currently, the most commercially developed TES technology implemented in CSP plants is two-tank sensible TES system where hot and cold working fluids are stored in two separate tanks (refer to Figure 2.2). However, this system offers minimal opportunity for reducing costs [93]. Thus, single-tank thermocline TES technology was introduced, incurring a lower investment cost in comparison with the two-tank system [94,95]. The thermocline storage is based on the thermal stratification constituted within the tank because of the density difference. Among single-tank thermocline TES technologies, dual-medium tanks have been employed more extensively. Nevertheless, single-medium tanks have demonstrated potential as a promising alternative to be implemented in the TES unit of CSP plants [96]. In a single-medium thermocline TES system, the less dense hot fluid moves upwards by the buoyancy force to displace the cooler fluid, creating a temperature gradient along the vertical direction within the tank. The zone between the hot and cold regions with a dramatic temperature gradient is called thermocline. The concept of the thermocline TES is represented graphically in Figure 2.8. During the charge phase, the thermocline region descends gradually because of the extension of the hot zone. Conversely, during the discharge phase, the thermocline region ascends gradually due to the extension of the cold region [97].

Thermal energy can be stored in the form of sensible heat or latent heat within a thermocline tank. Next sections compile an overview of existing literature for these two concepts, representing sensible heat storage in Section 2.3.1 and latent heat storage in Section 2.3.2.

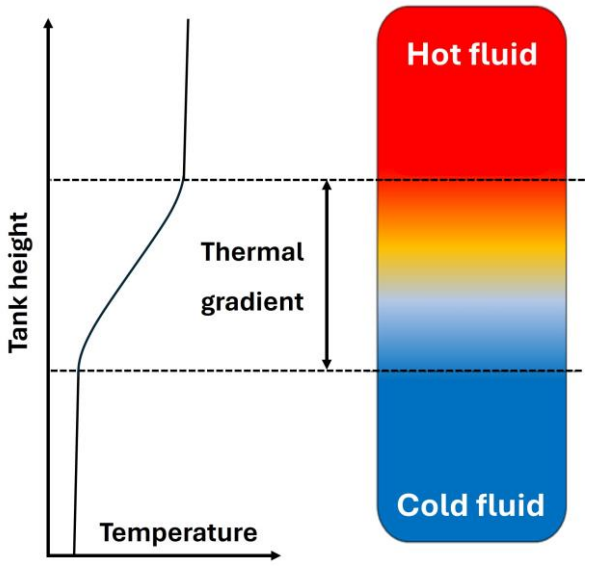

Figure 2.8: The thermocline concept: hot and cold mediums stored in the same tank and separated by a thermal gradient.

2.3.1 Sensible heat storage

Sensible heat storage within the single-medium thermocline tank has been explored by numerous studies. Gajbhiye et al. [98] established an experimental setup of a direct single-medium thermocline tank with a vertical flow distributor, using water as the working fluid. A schematic layout of this system is illustrated in Figure 2.9. As shown in Figure 2.9, a vertical flow distributor has been installed eccentrically at a distance from the tank center to reduce potential flow disturbance spreading within the entire tank. The flow distributor employed in the experiment was of annular porous type with multiple holes along the height and the periphery. It was reported that the thermocline thickness could be reduced by the flow distributor through mitigating the thermal diffusion during the charging process, and a higher flow rate might further decrease the thickness of the thermocline region. These results were also confirmed by Shaikh et al. [96] through performing a numerical analysis of the same storage tank. This storage system was further investigated numerically by Joshi et al. [99] to assess the effect of the porosity and permeability of the distributor wall on the thermal stratification within the tank. The results showed that the impact of the permeability of the flow distributor on the thermal stratification could be more dominant compared to the porosity. Advaith et al. [97] also performed an experimental investigation on a direct single-medium

thermocline TES system. It was claimed that the most effective HSM could be a room-temperature liquid with a high operating range and a high specific heat. Additionally, Gajbhiye et al. [100] experimentally studied a direct single-medium thermocline tank equipped with a flow distributor with regard to three performance parameters. According to the results, the tank with a central flow distributor indicated a reduced thermal gradient region by 60% in comparison to the tank without a flow distributor. Lou et al. [101] also carried out a numerical analysis to solve the flow maldistribution problem in a single-medium thermocline tank by properly structuring the inlet and outlet manifolds. In this respect, optimized perforated baffles were inserted in the manifolds. Based on the results, it was claimed that the proposed approach could significantly enhance the thermal performance of the TES system in terms of charging/discharging efficiency, capacity ratio and overall efficiency. This numerical result was then confirmed by an experimental study presented in [102]. Moreover, the proposed system was further enhanced by incorporating a buoyant jet into the thermocline tank [103]. It was found that the buoyant jet entrainment could result in a more efficient thermal performance compared to the initial uniform baffle distributor. However, despite the above-mentioned studies that investigated the direct thermocline TES technology, the present work focuses on an indirect thermocline TES system. In this regard, a different strategy was adopted to prevent the flow mixing, implementing two heat exchangers for charging and discharging purposes.

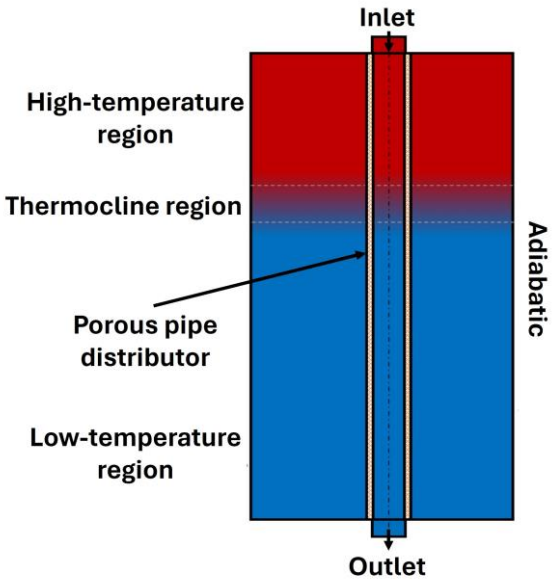

Figure 2.9: Schematic layout of a single-medium thermocline tank with porous pipe flow distributor, experimentally developed by Gajbhiye et al. [98].

Gaggioli et al. [104] conducted an experimental analysis of a single-medium indirect molten salt thermocline tank developed by ENEA. Two helically coiled serpentine HXs were incorporated into the storage tank for charging (bottom serpentine) and for discharging (top serpentine). An internal vertical channel was employed to drive the salt motion, connecting the two HXs. The experimental results revealed that the thermocline performance could be enhanced by making specific geometric modifications. Furthermore, it was claimed that the integration of phase change material (PCM) could further improve the system performance through stabilizing salt temperature in the upper region of the tank. This prototype was also investigated by Cagnoli et al. [105] through a transient 2D CFD model to compute heat losses and salt temperature distribution within the tank during the charge and discharge processes. The study reported several geometrical issues in the tank that could be mitigated by adopting appropriate optimization measures. This thesis focuses on the above-mentioned thermocline storage system presented by [104,105] to address ineffective geometric characteristics and to enhance the thermal performance by implementing specific optimization strategies (refer to Section 5.3).

2.3.2 Latent heat storage

Although sensible heat storage currently dominate the TES market, latent heat storage has exhibited considerable potential as a viable alternative [106]. Adopting latent heat storage approach by using PCM could result in a reduced tank size and a lower capital cost due to a higher energy storage capacity, compared to the sensible heat storage system [107]. Thermal performance of PCM-based TES systems has been investigated by several studies. Wu et al. [108] developed a transient 2D model to analyze the dynamic thermal performance of a molten salt packed-bed TES system using PCM capsules. As shown in Figure 2.10, the system included a vertical cylindrical tank with inlet and outlet ports on the top and bottom for hot and cold flows, respectively. PCM capsules were packed within the tank, while molten salt flew through the void space. The model investigated the heat transfer between the molten salt and the packed PCM capsules. A parametric sensitivity analysis indicated different trends for the capsule temperature in various processes because of the existence of the isothermal solidification process during the discharging phase. This resulted in a quasi-isothermal region and two thermocline regions along the tank height, and a quasi-isothermal period for the molten salt temperature at the outlet. It was reported that a decrease in the molten salt inlet velocity or in the capsule diameter or an increase in the phase change temperature would improve the discharging efficiency of the system.

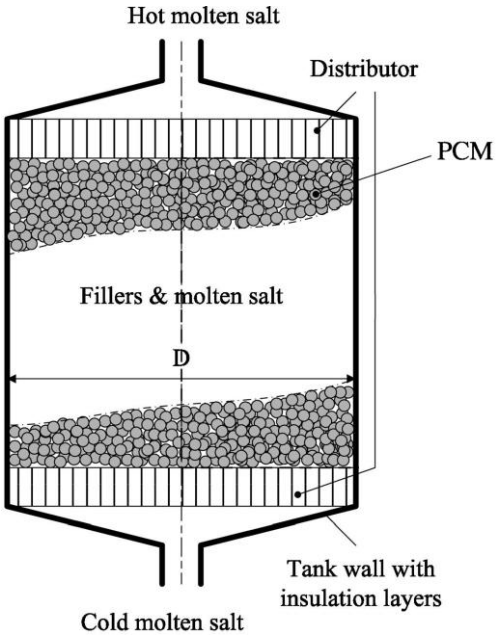

Figure 2.10: Schematic of a molten salt packed-bed TES system with spherical PCM capsules, studied by [108].

Bellan et al. [93] performed a numerical and experimental analysis on the dynamic thermal performance of a lab scale thermal energy storage system packed with PCM capsules (sodium nitrate). The transient 2D numerical model was validated by comparing with the experimental results. It was found that the heat transfer fluid flow rate plays a key role on the rate of charging/discharging process, and the thermal performance of the system is remarkably influenced by the shell properties of the capsule. Moreover, Galione et al. [109] carried out a numerical analysis on a multi-layered solid-PCM thermocline TES system (see Figure 2.11). As illustrated in Figure 2.11, the TES system consisted of three layers: a PCM layer at the top with a high melting point, a molten salt layer as the heat transfer fluid, and a PCM layer at the bottom with a low melting point. A numerical methodology was adopted by considering the same amount of stored/released energy in consecutive charging/discharging cycles for solid-filled thermocline, single encapsulated PCM, multi-layered solid-PCM and cascaded PCM configurations. It was suggested that a configuration with multi-layered solid-PCM could prevent the high thermocline degradation observed in single-solid filled systems, resulting in a significantly higher thermal efficiency. Compared to the cascaded PCM configuration, the proposed concept required much less volume of encapsulated PCM for the same total stored energy. This concept was then employed to design a TES system for a 50 MWe parabolic trough plant [110].

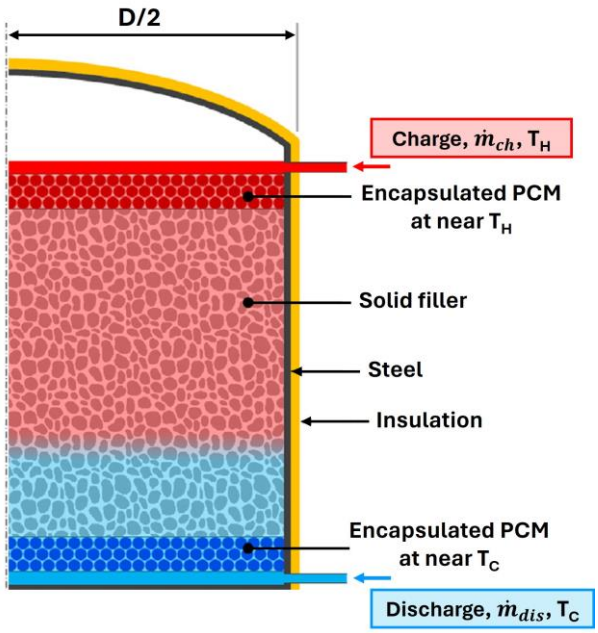

Figure 2.11: Sketch of a multi-layered solid-PCM thermocline TES tank with three layers, investigated by [109,110].

Zhao et al. [111] explored the transient thermal behavior of a multi-layered solid-PCM thermocline system during the charging and discharging processes over cyclic operational conditions. The study demonstrated that larger packed-bed radius would lead to a higher total capacity factor and a longer cyclic operating duration. Conversely, larger volume ratios between two PCM layers result in a lower total capacity factor and a shorter operating duration. The impact of PCM layers on increasing the cyclic operating duration of the system was more considerable at lower filling proportion of PCM layers. This study was then followed by a system-level thermal analysis conducted on five different packed-bed configurations [112]. It was highlighted that partial charge cycles may result in a thermocline degradation, influencing the energy stored/released in the subsequent full charge cycles. The configurations with encapsulated PCMs indicated greater resistance and enhanced recoverability to the variation in energy storage/release capacity of the TES system. Furthermore, assessment of a practical operating condition revealed that the energy storage capacity of various configurations decreases during the operation owing to the partial charge effect, resulting in energy release capacity reductions and energy collection discards.

Wang et al. [113] established an experimental setup of a thermocline TES system to investigate the effect of the PCM balls position on the thermal

stratification within the tank considering various inlet flow rates. The results showed that the thermal stratification within the tank could improve by reducing the height and the diameter of the PCM balls at a constant flow rate. However, increasing the flow rate degraded the thermal stratification by increasing the cold and hot water mixing. While for lower flow rates the thermal stratification of the tank without PCM balls was superior to that of the PCM water tank, for higher flow rates the PCM water tank performed better with the PCM balls located at the lowest height. In addition, Suresh and Saini [114] conducted an experimental study on a combined sensible-latent heat storage system (see Figure 2.12). As shown in Figure 2.12, the TES system was filled with concrete spheres and PCM capsules, while PCM capsules were located above the concrete spheres, acting as a thermal buffer. The study aimed at tackling the issue of thermocline degradation considering various volume fractions of PCM during the charging and discharging processes. Based on the results, volume fraction of PCM had a significant effect on the thermal stratification of the system as the rapid degradation of the thermocline was minimized by increasing the volume fraction of PCM. Higher volume fractions of PCM resulted in greater energy storage, extraction and cumulative energy transfer as well. It was also proposed that discharge at lower flow rates could be more efficient in terms of energy utilization for a longer time duration in the case of solar thermal applications.

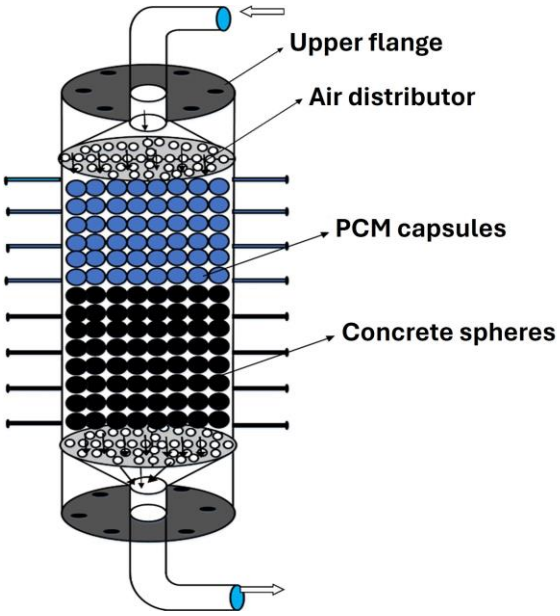

Figure 2.12: Schematic layout of a combined sensible-latent heat storage system, experimentally developed by [114].

Keilany et al. [115] carried out an experimental and numerical study of a pilot-scale thermocline TES system with synthetic oil as HTF consisting of a layer of stainless-steel tubes containing PCM filled with sodium nitrate. During the charge phase in the experiment, HTF temperature showed a semi-plateau profile near the phase change temperature of the PCM at 30 min. Accordingly, during the discharge phase, the impact of PCM solidification was observed close to the phase change temperature of the PCM after 90 min. Another semi-constant region appeared below the phase changing point of the PCM after 105 min. This implied that the heat transfer between the liquid PCM and the stainless steel is limited by the already solidified PCM, reducing the efficiency of the process.

Furthermore, Elfeky et al. [116] performed a thermo-economic analysis on eight different TES configurations to evaluate the impact of PCM layer thickness change on the system performance. The main objective of the study was to prevent temperature fluctuations at the end of the discharge process. According to the results, a configuration with 15% PCM at both top and bottom of the tank would lead to the most efficient performance among the cases under investigation, providing a reduced thermocline region and an enhanced thermal efficiency. In addition, Zahid et al. [117] established an experimental setup of a TES system with multi-layered PCM for medium temperature applications. Four configurations were explored during the experiments, including two single-layered sensible heat concrete with PCM, a multi-layered sensible heat concrete with PCM, and a single sensible heat concrete block arrangement. The results revealed that the multi-layered configuration could attain the highest discharge efficiency and storage capacity. It was concluded that the use of multiple PCM layers could be a viable and economical solution for TES at medium temperatures. Recently, Elfeky et al. [118] conducted a numerical analysis of a multi-layered thermocline tank with three cascaded PCM layers. In this regard, a parametric analysis was carried out to evaluate the impact of varying PCM melting temperature on the basis of variations in the dimensionless temperature differences. It was reported that reaching equal dimensionless temperature differences across the three PCM layers would lead to the most enhanced thermal performance of the TES system.

However, in the present thesis, a novel configuration of the thermocline TES tank with layers of toroidal tubes containing PCMs has been proposed. This concept of PCM introduction within TES systems has not been previously presented in the existing literature. The toroidal setup of the tubes not only keeps the axisymmetric layout of the tank, but can also allow us to locate PCMs at the desired height inside

the tank. Furthermore, the vertical motion of salt across the tubes simulates a cross-flow HX, potentially leading to more effective heat transfer.

Chapter 3

Photo-Thermal Optimization of a Parabolic Trough Collector

3.1 Overview

Selective coating plays a key role in a PTC system to harness solar energy efficiently by maximizing sunlight absorption and minimizing heat losses to the environment. In this regard, this chapter presents specific optimization strategies for implementing selective coatings on the absorber tube aimed at the photo-thermal enhancement of a PTC, thereby improving the overall performance of the system. The main objectives and scope of this work are outlined in Section 3.2, while Section 3.3 represents the methodology adopted. Then, a lumped-parameter model is introduced along the radial direction of the PTC receiver tube to obtain heat losses as a function of HTF temperature (Section 3.4). This model has been validated against experimental data for two different tubes (Section 3.4.2). Subsequently, a 1D model is represented to compute the energy balance along the tube axis to obtain required tube lengths using heat losses correlations (Section 3.5). Finally, the photo-thermal efficiency is computed for different scenarios to determine the most optimized configuration using multiple coatings along the receiver axis, and then, the respective tube length is calculated (Section 3.6). The content of this chapter is mostly based on the work published in [119].

3.2 Problem definition

The reference PTC considered in this study is depicted in Figure 3.1. As shown, the receiver tube includes an absorber tube made of the stainless-steel material, encapsulated by a borosilicate glass cover. The absorber tube transfers the energy of the concentrated solar radiation to the HTF, which is molten salt (60%wt. $NaNO_3$ + 40%wt. KNO_3 [120]) operating at the temperature range of 290-550 °C. The gap region between the absorber tube and the glass cover is kept under vacuum conditions with very low pressure (10^{-2} Pa) to ensure a high thermal insulation of the receiver tube. The geometrical specifications of the receiver tube are also outlined in Figure 3.1.

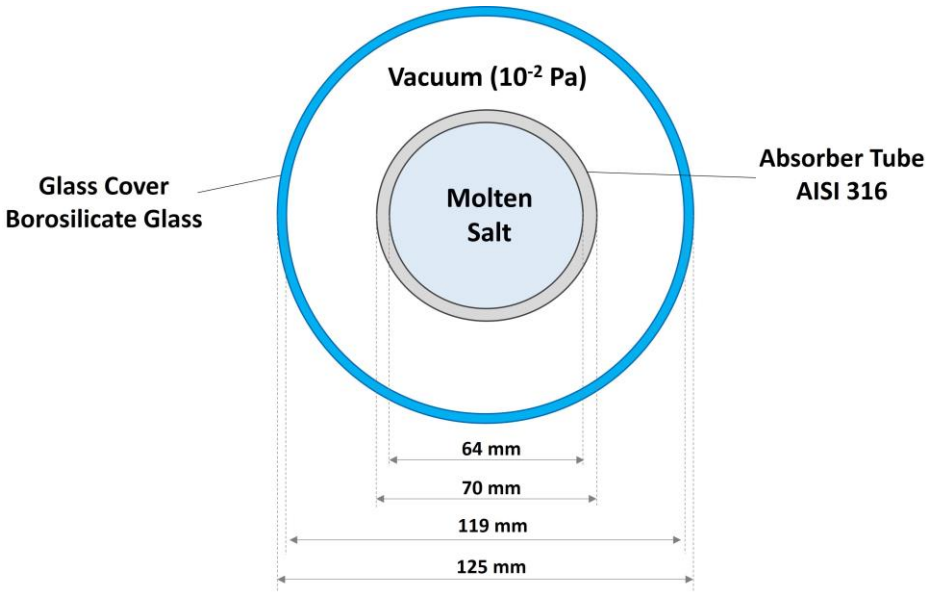

Figure 3.1: Cross-sectional view of the reference PTC receiver tube

In order to enhance the photo-thermal performance of the receiver tube, a selective coating is applied to the outer surface of the absorber tube. This selective coating is characterized by a high absorptivity in the solar spectral range and a low emissivity in the infrared range. Figure 3.2 shows the schematic of the multi-layer coating considered in this study, which has been developed by ENEA for CSP applications at high temperatures [73,121]. As shown, the first layer is a metallic layer with low emissivity and high reflectivity in the infrared range. The second layer represents a cermet layer made of ceramic and metallic materials, which ensures a high absorptivity in the solar spectral range. Finally, an anti-reflection layer is applied to the external side. In the selective coatings designed by ENEA,

the metallic layer can be molybdenum or tungsten [121], or alternatively, silver [73].

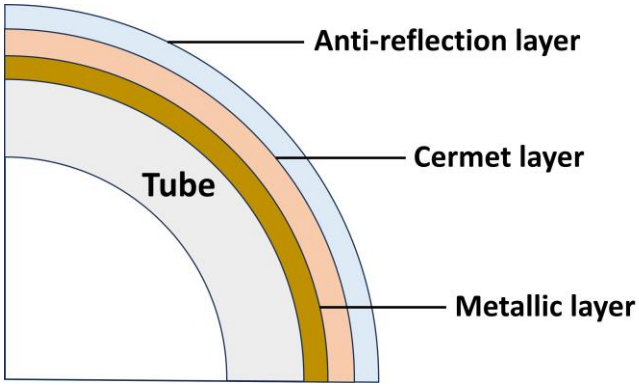

Figure 3.2: Schematic of the multi-layer coating of an absorber tube

This study aims to optimize the photo-thermal efficiency of the receiver tube in a PTC system. For this purpose, the strategy of implementing multiple selective coatings along the receiver tube is adopted in this work. This strategy depends on variations of the photo-thermal performance of selective coatings with respect to the operating temperature. In fact, it is expected that a selective coating representing a high photo-thermal efficiency at low temperatures (close to the receiver inlet section), would not be the best option at higher temperatures (close to the receiver outlet section). Therefore, it is essential to determine the best configuration of the receiver tube using multiple coatings based on the expected HTF temperatures along the collector line in order to achieve the highest photo-thermal efficiency. In this respect, six selective coatings were considered in this study with different absorptivity and emissivity data. The emissivity of the coatings is a function of temperature, which can be written as (T in [°C]):

$$\varepsilon = a_3 T^3 + a_2 T^2 + a_1 T + a_0 \tag{3.1}$$

The values of coefficients a_3, a_2, a_1, a_0 and the absorptivity data are given in Table 3.1 for the six coatings under investigation. Figure 3.3 also depicts the emissivity data for these six selective coatings with respect to the surface temperature. The absorptivity data provided for these coatings are sourced from [73]. However, it is worth noting that the emissivity data presented in [73] correspond to a specific temperature point (580 °C). Consequently, the emissivity correlations with respect to temperature were provided by ENEA through private communication.

Based on the photo-thermal efficiency obtained for the receiver tube using each selective coating at various ranges of the HTF temperature, the most efficient configuration will be introduced. This configuration represents the distribution of the coatings along the receiver tube to reach the highest photo-thermal efficiency.

Table 3.1: Absorptivity data and emissivity correlation coefficients for the six selective coatings considered in the photo-thermal optimization study.

Selective coating	Absorptivity	Emissivity correlation coefficients (Eq. (3.1))			
		a_3	a_2	a_1	a_0
Coating #1	0.9265	1.53E-10	9.95E-09	1.91E-05	0.023
Coating #2	0.9375	1.21E-10	5.56E-08	1.40E-05	0.025
Coating #3	0.9411	1.62E-10	3.21E-08	2.55E-05	0.021
Coating #4	0.9486	1.61E-10	6.95E-08	1.73E-05	0.023
Coating #5	0.9544	1.01E-10	1.49E-07	-9.80E-07	0.030
Coating #6	0.9665	1.42E-10	1.70E-07	2.66E-05	0.030

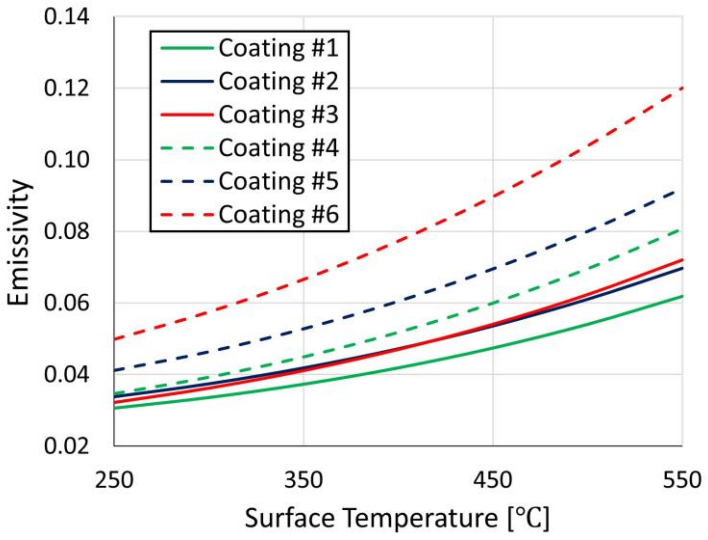

Figure 3.3: Emissivity of the six selective coatings as a function of temperature considered in the photo-thermal optimization study.

3.3 Methodology

The computational procedure implemented for the photo-thermal optimization of the PTC receiver tube is summarized in Figure 3.4. As shown, the main goal of this study is to determine the most efficient multi-coating configuration from a photo-thermal viewpoint. To attain this goal, the distribution of the selective coatings along the receiver tube must be outlined. This requires specifying the most effective coatings to be employed at different HTF temperatures, as well as the profile of the HTF temperature along the axial direction. While the former must be determined through the calculation of the photo-thermal efficiency for each coating based on the HTF temperature, the latter is provided by a 1D thermal model that solves the energy balance for the HTF along the receiver axis. This 1D model requires an accurate evaluation of heat losses as a function of HTF temperature, which is provided by a steady-state lumped-parameter model developed along the radial direction of the receiver tube. The lumped-parameter model also computes the temperature of the absorber tube wall required to calculate the photo-thermal efficiency. The boundary conditions required for this model include mass flow rate, HTF temperature, incident solar heat flux, ambient temperature and (transversal) wind speed.

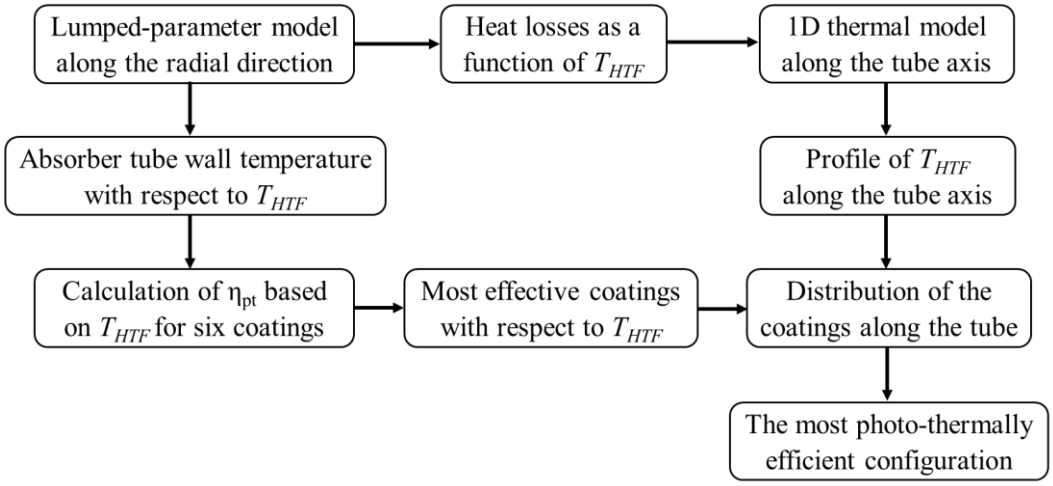

Figure 3.4: Methodology adopted for the photo-thermal enhancement of the PTC receiver tube.

3.4 Radial lumped-parameter model

In this section, the lumped-parameter model of the receiver tube is presented. This model was developed using the Modelica language, aiming at calculating the tube wall temperature and heat losses at different HTF temperatures.

3.4.1 Model description

The lumped-parameter model considers a cross section of the receiver tube characterized by a given HTF temperature and computes heat fluxes along the radial direction from the HTF to the external ambient, see Figure 3.5. The walls of the absorber tube and the glass envelope were discretized along the azimuthal direction, where 20 elements were sufficient to ensure a solution independent of the discretization. The applied boundary conditions include ambient temperature, (transversal) wind speed, HTF temperature, mass flow rate, and the azimuthal distribution of the incident solar heat flux on both the absorber tube and the glass envelope.

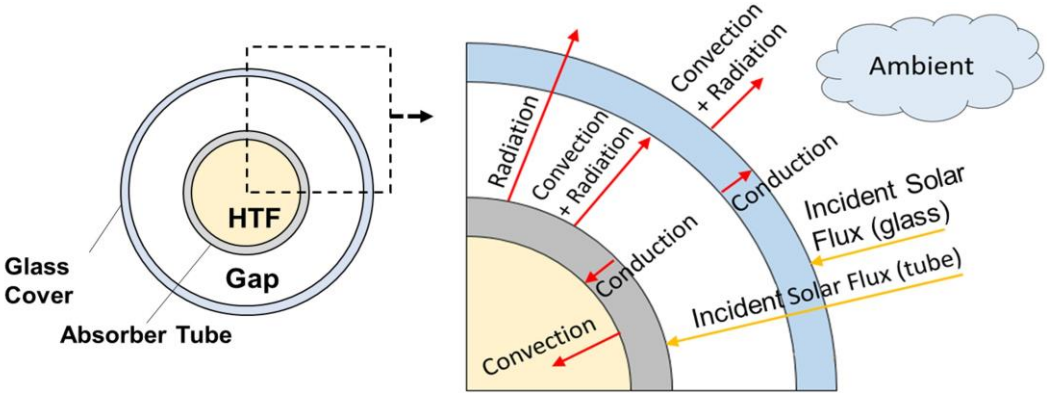

Figure 3.5: Heat fluxes in the radial direction considered in the lumped-parameter model [122].

As shown in Figure 3.6, the thermal driver required for the lumped-parameter model include the distribution of the incident heat flux along the azimuthal direction of the absorber tube (in [W/m^2]) and the azimuthal distribution of the absorbed power density by the glass cover (in [W/m^3]). These distributions have been computed through a ray-tracing code by ENEA for a reference case, corresponding to an incidence angle of 0°, a tracking and inclination error of 0° and a DNI of 900 W/m^2. The incidence angle of 0° could represent solar noon for an E-W oriented collector. However, various incidence angles have also been investigated for the

photo-thermal optimization purpose, and it was found that the final results would always remain consistent across different incidence angle values.

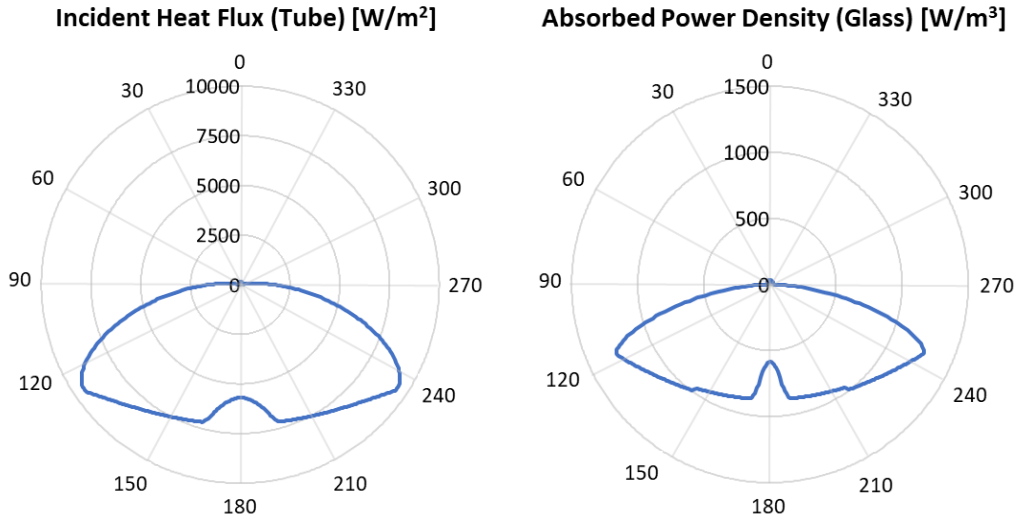

(a) (b)

Figure 3.6: Azimuthal distribution of: (a) the incident heat flux on the absorber tube, and (b) the absorbed power density by the glass envelope.

The lumped-parameter model of the receiver tube developed in this study is based on [122], incorporating the following assumptions:

- The conductive heat loss through the support structures of the receiver unit was ignored, as it can be negligible according to [123].
- The azimuthal thermal conductions within the absorber and the glass tube walls were neglected, according to [124].
- The glass envelope was not assumed to be completely opaque in the infrared range. Instead, a transmissivity of 0.11 was considered according to the Kirchhoff's law, based on the emissivity of 0.89, while the reflectivity is set equal to zero [71].

The HTF mass flow rate was imposed equal to 2.2 kg/s, according to the reference 1 MWe CSP-ORC pilot plant at the Green Energy Park in Morocco [125]. On the inner wall of the absorber tube, a Robin boundary condition is imposed, which requires defining the temperature of the HTF and the convective heat transfer coefficient. The latter is obtained, given the HTF mass flow rate, by means of the Gnielinski correlation [122].

The radial conduction in the glass and absorber tube walls can be calculated as (in [W/m]):

$$Q_{cond} = 2\pi k \frac{(T_{ext} - T_{int})}{ln(D_{ext}/D_{int})} \tag{3.2}$$

where k is the thermal conductivity of the wall, T_{ext} and T_{int} correspond to the wall temperatures on the external and internal surfaces, D_{ext} and D_{int} are the external and internal diameters of the tube, respectively.

The heat transfer between the absorber tube and the glass cover occurs by radiation and convection. The radiative term is obtained by:

$$Q_{rad} = (1 - \tau) \frac{\sigma\pi D_{ab,ext}\left(T_{ab,ext}^4 - T_{gl,int}^4\right)}{1/\varepsilon_{ab} + \left(1 - \varepsilon_{gl}\right)D_{ab,ext}/\left(\varepsilon_{gl}D_{gl,int}\right)} \tag{3.3}$$

where τ represents the transmissivity of the glass in the infrared, σ is the Stephan-Boltzmann constant, ε_{ab} and ε_{gl} are the emissivity of the absorber tube (given by the selective coating) and of the glass, $T_{ab,ext}$ and $T_{gl,int}$ indicate the temperatures of the external surface of the absorber tube and the internal surface of the glass, respectively. $D_{ab,ext}$ and $D_{gl,int}$ are the outer diameter of the absorber tube and the inner diameter of the glass envelope, respectively.

The convective heat transfer in the gap region is evaluated by means of the Newton's cooling law, which requires introducing a heat transfer coefficient, assumed to be equal to 1.115×10^{-4} W/m^{2}K [122,126].

Due to the partial transmissivity of the glass in the infrared, the absorber tube also loses heat by radiation directly to the external ambient. This contribution can be calculated by:

$$Q_{rad} = \tau\sigma\varepsilon_{ab}\pi D_{ab,ext}\left(T_{ab,ext}^4 - T_{amb}^4\right) \tag{3.4}$$

The heat losses from the outer surface of the glass to the external ambient occur by radiation and convection. The former is evaluated according to the Stefan-Boltzmann law, as a function of the glass emissivity and the temperature of the glass outer surface, given the temperature of the cold sink which is the sky temperature approximated to be 8 °C below the ambient temperature, according to [122]. The

convective heat losses are calculated by means of the Newton's law of cooling introducing a proper heat transfer coefficient. The latter can be determined by Churchill-Chu's and Zhukauskas' correlations for natural and forced convection, respectively [67].

3.4.2 Validation

The lumped-parameter model was validated against two sets of experimental data provided by ENEA for two different receiver tubes:

1. SCHOTT PTR®70 first generation (2005)
2. ASE HCEMS-11

In the first case, the experimental campaign was carried out at the ENEA Casaccia laboratory, while in the second case, the test was conducted by Archimede Solar Energy (ASE). The materials and the geometry of the tubes correspond to the configuration shown in Figure 3.1. The selective coatings adopted in the two cases are characterized by an emissivity as a function of temperature (see Figure 3.7) and an absorptivity equal to 0.95 for the SCHOTT tube and 0.9487 for the ASE tube.

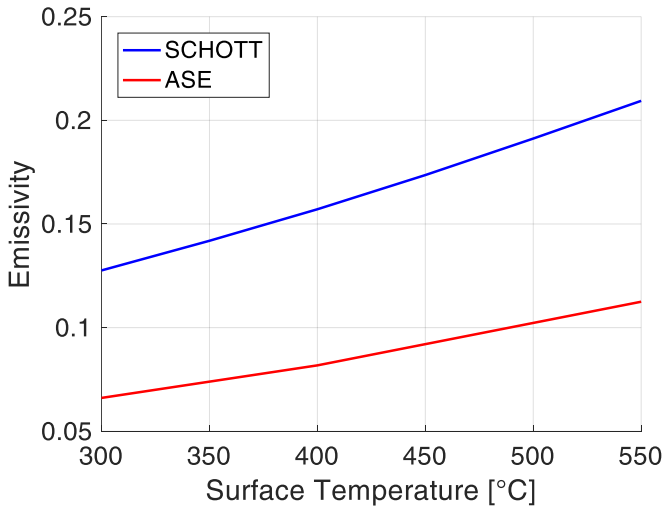

Figure 3.7: Emissivity of selective coatings applied to the SCHOTT and ASE absorber tubes.

Both tests were conducted by heating the absorber tube by the Joule effect until attaining a practically uniform tube temperature. At this point, the electrical power supplied to the absorber tube must correspond to the power dissipated towards the

external environment. The temperature of the absorber tube is measured by means of nine thermocouples positioned on the internal side. As depicted in Figure 3.8, there are three thermocouples positioned approximately 40 cm from one end of the tube, another set of three about 25 cm from the opposite end, and the remaining three at the center of the tube. These thermocouples are distributed at angular intervals of 120°, see Figure 3.8.

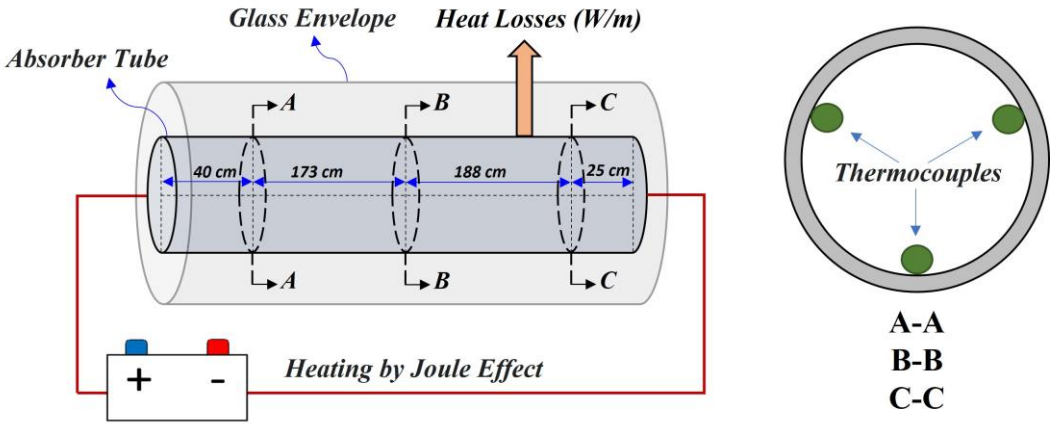

Figure 3.8: Experimental setup established to measure heat losses from the absorber tube to the environment, highlighting the schematic positions of the thermocouples.

In the experiment performed on the SCHOTT receiver, the inside of the absorber tube was well thermally insulated (adiabatic), while in the case of the ASE receiver, this information is not available; in agreement with ENEA experts, it was assumed that both ends of the tube are closed by metal plates to prevent the replacement of air inside the tube. This implies that thermal losses would also occur from the internal surface of the tube, although these losses would be minor. The results of the experimental tests are summarized in Table 3.2 and Table 3.3 for the SCHOTT and ASE receiver tubes, respectively.

To reproduce the experimental conditions, the lumped parameter model was modified as follows:

- The wind speed was set to zero (natural convection) as the tests were conducted inside the laboratories, i.e., a closed environment.
- The ambient temperature was set to be equal to that measured during the tests (Table 3.2 and Table 3.3).
- The cold sink temperature for the radiative heat loss from the outer surface of the glass to the external environment was assumed to be equal to the

ambient temperature since the tests were conducted inside the laboratories and the tube does not see the sky.

- The absorptivity and emissivity data (Figure 3.7) of the selective coatings were implemented in the model.

Table 3.2: Data collected from the experiments carried out on the SHOTT receiver tube

Absorber tube temperature [°C]	Glass tube temperature [°C]	Ambient temperature [°C]	Heat losses [W/m]
301.22	56.64	26.36	162.75
350.73	67.08	26.47	261.32
400.17	81.57	26.71	388.83
449.43	97.46	27.04	570.06
498.34	113.71	24.72	795.88
545.65	133.55	25.43	1108.25

Table 3.3: Data collected from the experiments carried out on the ASE receiver tube

Absorber tube temperature [°C]	Glass tube temperature [°C]	Ambient temperature [°C]	Heat losses [W/m]
300	44	23.2	110
400	63	23.8	255
550	109	24.7	762

- The thermal driver of the model was modified by replacing the solar flux with an imposed temperature on the internal surface of the absorber tube, according to the experimental data (Table 3.2 and Table 3.3). Therefore, the convective heat transfer with the molten salt was not considered. In the case of the ASE receiver tube, thermal losses due to natural convection between the internal surface of the tube and the stagnant air inside it were also considered, calculated using a proper correlation [127]. It was observed that the air trapped inside the tube in stationary conditions has a temperature significantly higher than the ambient temperature, close to that of the absorber tube.

Regarding the first case (SCHOTT receiver tube), a comparison was initially made between the lumped-parameter model and experimental results in terms of glass temperature. However, since the SHOTT tube belongs to the first generation (2005), it is expected that the emissivity of the glass could change over time. As shown in Figure 3.9a, it was found that an emissivity of 0.7 for the glass cover could reproduce the experimental results effectively, with a maximum deviation of about 8.6%. This model was then validated against experimental data in terms of heat losses towards the external environment. As can be seen in Figure 3.9b, there is a good agreement between the present model and the experimental data, with a maximum deviation of approximately 6%.

In the second case (ASE tube), the results obtained by the lumped-parameter model showed that the default value of 0.89, already proposed in the literature [71], correctly reproduces the glass temperature. As can be seen in Figure 3.10a, a good agreement can be observed between the present model and experimental results, exhibiting a maximum deviation of about 6.7%. In addition, a comparison in terms of heat losses revealed a satisfactory agreement between the model and the experiment, as shown in Figure 3.10b, with a maximum deviation of about 6.5%.

3.4.3 Results

After validation of the lumped-parameter model, it was employed to derive the data required for the 1D model and for computing the photo-thermal efficiency, as explained in Section 3.3. Firstly, heat losses must be correlated with the HTF temperature for different applied selective coatings to be used in the 1D model. For this purpose, the lumped-parameter model was run by varying the HTF temperature and incorporating the six selective coatings.

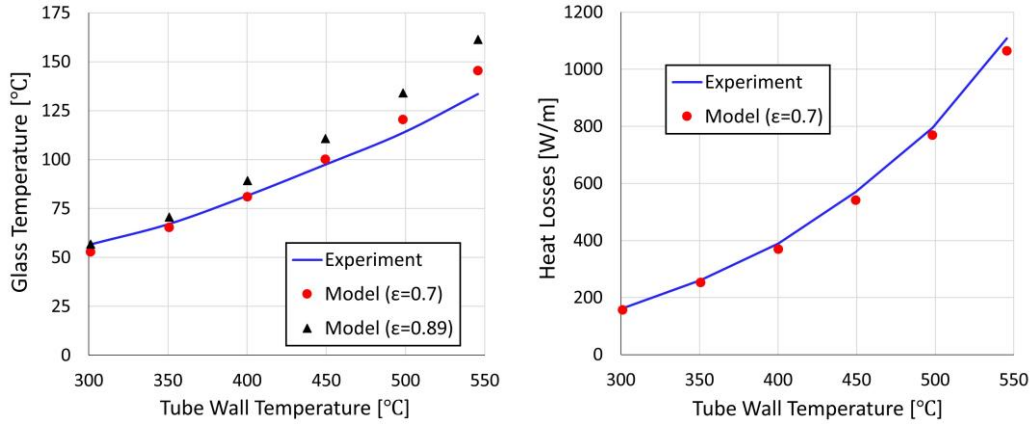

(a) (b)

Figure 3.9: Comparison between experimental data and model results for the SCHOTT tube in terms of: (a) glass temperature and (b) heat losses.

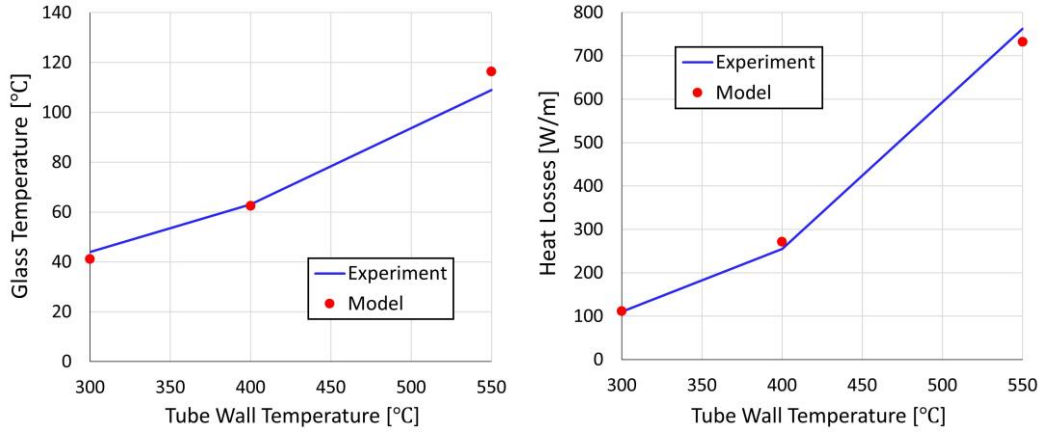

(a) (b)

Figure 3.10: Comparison between experimental data and model results for the ASE tube in terms of: (a) glass temperature and (b) heat losses.

Figure 3.11 depicts heat losses with respect to the HTF temperature using different coatings for wind speeds of 0 m/s (natural convection) and 15 m/s (forced convection with intense wind effects). As can be observed, using Coating #1 and Coating #6 provide the lowest and the highest heat losses from the absorber tube, respectively, at various HTF temperatures, which correspond to the emissivity data

provided in Figure 3.3. Furthermore, a small difference can be found between the cases of 0 m/s and 15 m/s due to the thermal insulation provided by the vacuum.

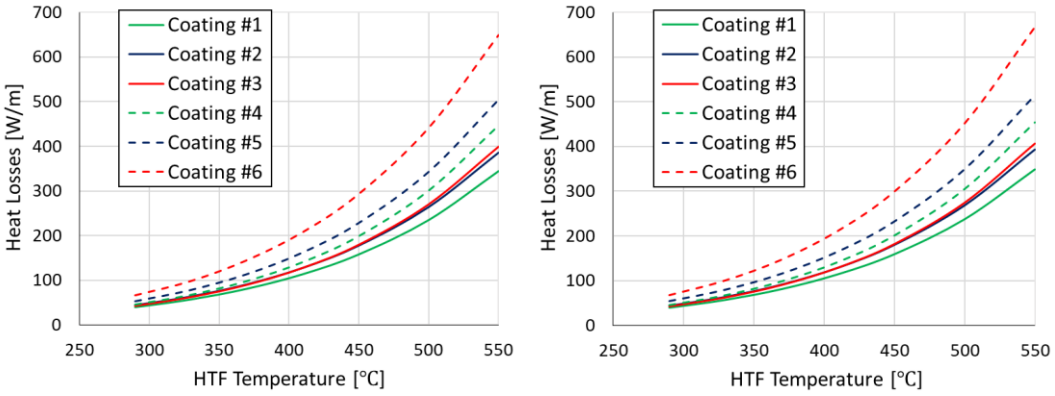

Figure 3.11: Heat losses from the absorber tube vs. HTF temperature, using different coatings, for a wind speed of (a) 0 m/s and (b) 15 m/s.

The curves illustrated in Figure 3.11 denotes correlations of heat losses as a function of HTF temperature, which can be written as (T_{HTF} in [°C]):

$$Q_{loss}(T_{HTF}) = aT_{HTF}{}^2 + \mathrm{b}T_{HTF} + c \tag{3.5}$$

The values of coefficients a, b and c are given in Table 3.4. These correlations were exploited by the 1D model to determine the HTF temperature profile along the tube axis, see Section 3.5.

Furthermore, in order to calculate the photo-thermal efficiency, it is essential to compute absorber tube wall temperatures at various HTF temperatures, as shown in Figure 3.12. The trend illustrated in Figure 3.12 remains consistent across all scenarios; implementing any selective coatings, whether in the presence or absence of wind, would lead to the same trend of the absorber tube wall temperature with respect to the HTF temperature, with a maximum difference of < 1 °C in the wall temperature among the cases. This is because the absorber tube wall temperature is mostly determined by the imposed HTF temperature due to a considerably higher heat transfer coefficient between the tube and the HTF compared to that between the tube and the gap region. This also leads to minor differences between the HTF

temperature and the absorber tube wall temperature for the whole receiver length, indicating a maximum difference of 4.4 °C.

Table 3.4: Coefficients of heat loss correlations using different selective coatings, obtained by the lumped-parameter model for a wind speed of 0 m/s and 15 m/s.

Applied selective coating	$V_w = 0$ m/s			$V_w = 15$ m/s		
	a	b	c	a	b	c
Coating #1	0.00406	-4.483	1281.8	0.00414	-4.575	1309.2
Coating #2	0.00451	-4.971	1416.6	0.00462	-5.100	1455.5
Coating #3	0.00483	-5.360	1534.2	0.00494	-5.493	1574.1
Coating #4	0.00546	-6.075	1740.4	0.00560	-6.237	1789.2
Coating #5	0.00599	-6.626	1889	0.00617	-6.836	1951.7
Coating #6	0.00775	-8.550	2431.4	0.00807	-8.945	2552

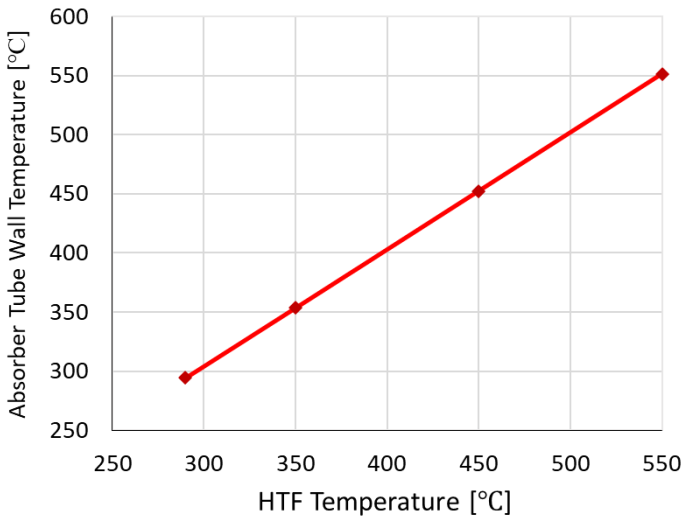

Figure 3.12: Absorber tube wall temperature with respect to the HTF temperature

3.5 Axial 1D model

This section introduces the simple 1D model discretized along the receiver axis. This model was developed to determine the profile of the HTF temperature along the tube and, consequently, the required tube length to ensure the desired temperature increase of the HTF (290-550 °C) at imposed mass flow rate (2.2 kg/s). The 1D model takes advantage of the results obtained by the lumped-parameter model namely, the correlations of heat losses with respect to the HTF temperature (Table 3.4).

Figure 3.13 provides a schematic representation of the 1D model, which basically solves the steady-state energy balance for the HTF along the receiver axis, see Eq. (3.6). The required boundary conditions include HTF inlet and outlet temperatures, mass flow rate and the heat flux transferred to the fluid, which corresponds to the absorbed heat flux net of the heat losses. Regarding the space discretization, the tube axis was divided in n control volumes of equal length; a length Δx of 1 m is sufficient to ensure the grid independence of the results. The actual number n of the control volumes depends on the computed receiver total length. Therefore, the final length of the receiver tube will be an integer multiple of Δx, which of course introduces an approximation that is negligible since Δx is significantly lower than the total tube length (always < 1%).

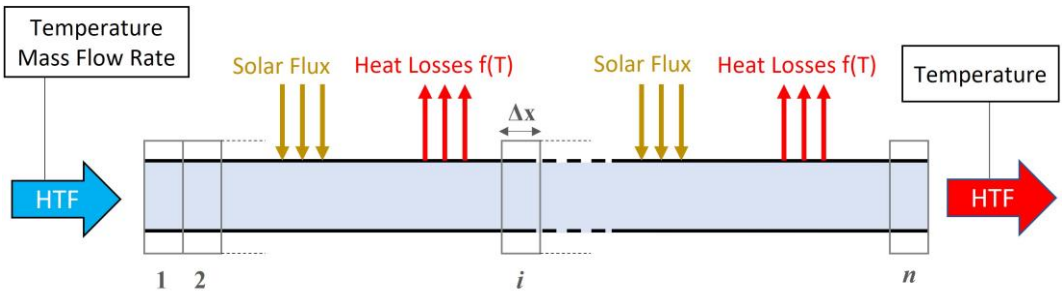

Figure 3.13: Schematic representation of the 1D model discretized along the tube axis, incorporating applied boundary conditions.

The energy balance equation for the HTF can be written as:

$$(Q_{abs} - Q_{loss}(T))\Delta x = \dot{m} \int_{T_i}^{T_o} c_p(T) dT \tag{3.6}$$

where Δx represents the length of the i-th control volume of the tube given by the space discretization, $\dot{m}$ is the imposed HTF mass flow rate, c_p denotes the specific heat as a function of HTF temperature, T_i and T_o represent HTF temperatures upon entering and leaving the control volume, respectively. Q_{abs} and Q_{loss} signify the absorbed solar power and the heat loss to the environment per unit length, respectively.

This simple model provides reliable results because it exploits the results of the validated lumped-parameter model presented in section 3.4. Particularly, the lumped-parameter model provides heat losses per unit length (Q_{loss} in Eq. (3.6)) as a function of HTF temperature.

The 1D model will be employed to determine the HTF temperature profile along the receiver axis and, consequently, the most photo-thermally efficient configuration of the receiver tube, as presented in Section 3.6.

3.6 Photo-thermal optimization of the parabolic trough system

This section aims to optimize the photo-thermal efficiency of the receiver tube in a PTC system, exploiting the results provided by the lumped-parameter and 1D models. The photo-thermal efficiency is defined as:

$$\eta_{pt} = \alpha - \varepsilon\left(\frac{\sigma T^4}{I}\right) \tag{3.7}$$

where α and ε are the absorptivity and emissivity of the selective coating, σ is the Stephan-Boltzmann constant, T represents the temperature of the external surface of the absorber tube (provided by the lumped-parameter model, see Figure 3.12), and I is solar irradiance, equal to 900 W/m^2 based on the ASTM G173-03 solar spectrum [128].

As shown in Figure 3.3, the emissivity of selective coatings depends on temperature, indicating considerable variations between the inlet and outlet sections of the receiver tube (HTF temperatures from 290 ℃ to 550 ℃). To achieve the highest photo-thermal efficiency, a strategy was adopted, in which multiple selective coatings were applied along the collector length based on their photo-thermal performance at different temperatures. In other words, for any particular segment of the collector length, the selective coating with the greatest photo-thermal efficiency was implemented. This strategy would facilitate attaining the

highest possible photo-thermal efficiency of the entire collector, incorporating the most efficient selective coatings at various temperature ranges along the tube.

In this approach, first, the lumped parameter model calculated the photo-thermal efficiency for various HTF temperatures, implementing the six selective coatings given in Table 3.1 and Figure 3.3. Subsequently, the most efficient selective coatings were chosen with respect to the photo-thermal efficiency achieved at various HTF temperature ranges. This result was then integrated with the HTF temperature profile along the receiver axis provided by the 1D model. Consequently, the distribution of the selective coatings along the tube was determined, which corresponds to the most photo-thermally efficient configuration of the collector line.

Figure 3.14 illustrates the photo-thermal efficiency with respect to the HTF temperature for the six selective coatings considered in the optimization study. The results shown in Figure 3.14 were obtained for an ambient temperature of 20 °C and wind speed of 0 m/s (natural convection). As can be observed, three temperature ranges are identified characterized by three different selective coatings to ensure the maximum photo-thermal efficiency:

- 290 - 436 °C → Coating #6
- 436 - 517 °C → Coating #4
- 517 - 550 °C → Coating #3

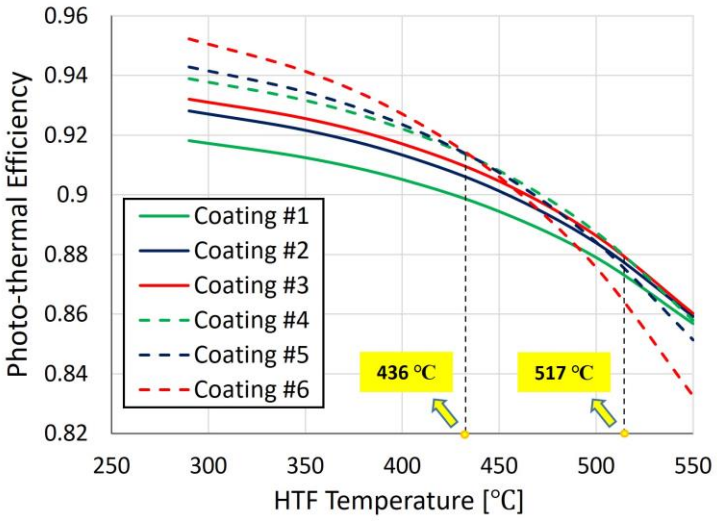

Figure 3.14: Photo-thermal efficiency for the six selective coatings considered in the optimization study.

In the next step, the spatial distribution of the selective coatings along the collector line must be determined. For this purpose, the respective tube lengths for each of the three segments identified in Figure 3.14 were calculated using the 1D model. Table 3.5 outlines the respective tube lengths for the three tube segments characterized by the corresponding selective coatings at certain temperature ranges. Moreover, Figure 3.15 depicts a schematic of the distribution of these selective coatings along the receiver tube, indicating the most photo-thermally efficient configuration. The total length of the optimized receiver tube is 1641 m and the overall photo-thermal efficiency is equal to 91.6%. This photo-thermal efficiency indicates a 0.5-1.9% increase compared to the single-coated receivers. It should be noted that the optimized configuration also allows reducing receiver costs since a coating that performs more effectively at high temperatures, typically demanding a higher price, is only applied to the final segment of the receiver tube.

Table 3.5: Results of the photo-thermal optimization, representing the temperature ranges characterized by the corresponding selective coatings and the respective lengths of the tube segments.

ΔT_{HTF} [°C]	Selective coating	Tube length [m]
290-436	#6	788
436-517	#4	563
517-550	#3	290

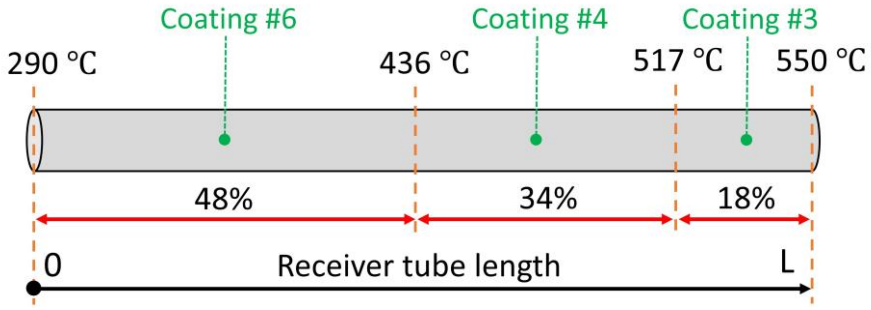

Figure 3.15: Distribution of the selective coatings along the receiver tube, representing the most photo-thermally efficient configuration.

In order to verify the wind effect on the solution obtained, the numerical procedure described above was repeated considering a wind speed of 15 m/s. The final length of the receiver tube in this case was calculated to be 1654 m, demonstrating less than 1% difference compared to the case of natural convection. This is due to the thermal insulation provided by the vacuum in the gap region, which protects the absorber tube against the wind effect. Furthermore, the distribution of the selective coatings along the collector line was obtained to be the same as the configuration illustrated in Figure 3.15.

3.7 Concluding remarks

This chapter presented a photo-thermally optimized configuration of a PTC system, adopting the strategy of arranging multiple selective coatings along the absorber tube. This arrangement is based on the photo-thermal performance of selective coatings at different HTF temperatures, ranging from 290 ℃ to 550 ℃. Six selective coatings were employed in this study, investigating wind speeds of 0 and 15 m/s.

At the initial step, a lumped-parameter model was developed along the radial direction of the receiver tube, aiming at computing absorber tube wall temperature and heat losses at various HTF temperatures. The model was validated against experimental data available for the two tubes of SCHOTT and ASE in terms of heat losses. Then, specific correlations were obtained by the lumped-parameter model for heat losses to be exploited by a 1D model, developed along the receiver axis to compute HTF temperature profile along the tube. In addition, absorber tube temperatures provided by the lumped-parameter model were exploited to compute photo-thermal efficiencies at different HTF temperatures, implementing the six selective coatings under investigation. The results of photo-thermal efficiencies determined the most efficient selective coatings for various HTF temperature ranges. This result was then integrated with HTF temperature profiles provided by the 1D model. Finally, the spatial distribution of the selective coatings were determined, representing the most efficient PTC configuration from a photo-thermal viewpoint.

According to the results, the most efficient configuration includes three HTF temperature ranges: for low HTF temperatures ranging from 290 ℃ to 436 ℃, coating #6 could provide the highest photo-thermal efficiency, requiring a tube length of 788 m. For medium temperatures from 436 ℃ to 517 ℃, coating #4 could be the best option, with a tube length of 563 m. For the final segment with HTF

temperatures from 517 ℃ to 550 ℃, coating #3 exhibited the highest photo-thermal performance, requiring a tube length of 290 m. The results were almost equal for wind speeds of 0 and 15 m/s because of the thermal insulation ensured by the vacuum in the gap region. The total length of the optimized receiver tube was obtained to be 1641 m and 1654 m for wind speeds of 0 and 15 m/s, respectively, representing a difference less than 1%. The optimized PTC configuration presented two main benefits: firstly, it resulted in an increase of 0.5-1.9% in the overall photo-thermal efficiency compared to the single-coated receivers; secondly, it could provide economic advantages owing to the implementation of more expensive coating only in the final segment.

Chapter 4

Comparative Techno-Economic Analysis of Linear CSP Technologies

4.1 Overview

Among linear CSP technologies, LFC system indicates remarkable economic advantages because of a simple and low-cost design; however, this technology suffers from a low optical efficiency compared to PTC system [129,130]. Moreover, while implementing an evacuated receiver tube for each PTC and LFC technology results in a higher thermal efficiency compared to a non-evacuated tube, higher expenses must be incured for the tube evacuation. Therefore, it is essential to perform a comprehensive comparison among different linear CSP systems. This chapter presents a comparative techno-economic analysis of PTC and LFC technologies using evacuated and non-evacuated tubes. In this regard, Section 4.2 introduces the reference systems considered for this study, while the methodology adopted is described in Section 4.3. Optical and thermal models are represented in Section 4.4 and Section 4.5, respectively. Finally, a comparative economic analysis is carried out in Section 4.6, encompassing a sensitivity analysis based on the key parameters affecting the LCOE (Section 4.6.1). The content of this chapter is mostly based on the work published in [131].

4.2 Description of the systems

The reference PTC system considered for the techno-economic analysis consists of one line of collector with the aperture width of 5.9 m and a receiver tube with the external diameter of 0.07 m and total length of 800 m. Regarding the reference LFC system, 10 rows of parallel mirrors with the aperture width of 0.625 m each and a receiver tube with the external diameter of 0.07 m, secondary concentrator of CPC type and total length of 800 m was assumed [132–135]. Table 4.1 outlines the main geometric and optical parameters of the PTC and LFC solar fields.

Table 4.1: Main geometrical and optical parameters for solar fields and receiver units

Parameter	LFC	PTC
Number of parallel mirror lines	10	1
Collector aperture width (m)	0.625	5.9
Collector focal length (m)	4	1.81
Distance between adjacent mirrors (m)	0.825	-
Total length of the receiver tube (m)	800	800
Outer/Inner absorber tube diameter (m)	0.070/0.064	0.070/0.064
Outer/Inner glass cover diameter (m)	0.125/0.119	0.125/0.119
Primary mirrors reflectivity	0.94	0.92
CPC reflectivity	0.90	-
Glass transmissivity	0.96	0.96
Glass refractive index	1.52	1.52
Glass extinction coefficient (m^{-1})	0.21	0.21
Receiver tube alignment	North-South	North-South

The scheme of the cross section of the LFC receiver unit is shown in Figure 4.1. It should be noted that the configuration is the same for both of the PTC and LFC technologies, except for the secondary concentrator, which does not exist in the case of the PTC technology (see Figure 3.1). While the gap region between the absorber tube and the glass cover is kept under vacuum conditions in the evacuated tube, this region is simply filled with air at ambient pressure in the case of the non-evacuated tube. The HTF is molten salt (60%wt. $NaNO_3$ + 40%wt. KNO_3 [120]) with the same operating temperature of 290-500 °C for both LFC and PTC systems to make the comparison as fair as possible.

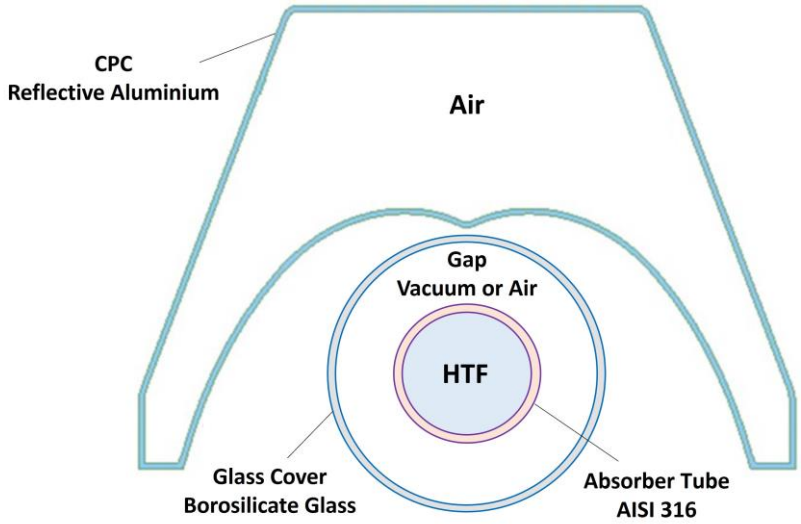

Figure 4.1: Cross-sectional view of the reference LFC receiver unit

Regarding the coating applied to the tube's outer surface, a commercially established selective coating (CERMET) was adopted in the case of the evacuated tube [136]. For the non-evacuated tube, a selective coating (AIR PLUS) under development at ENEA, which is suitable for working in air, was considered in this study. Absorptivity data and emissivity equations of these coatings are provided in Table 4.2 (T in [°C]). The emissivity equations are depicted in Figure 4.2.

Table 4.2: Properties of the two coatings considered in this study

Configuration	Coating	Absorptivity	Emissivity
Evacuated	CERMET	0.95	$\varepsilon = 0.07513 + 2.2E\text{-}7\ T^2$
Non-evacuated	AIR PLUS	0.943	$\varepsilon = 0.02339 + 1.38E\text{-}4\ T + 1.76E\text{-}7\ T^2$

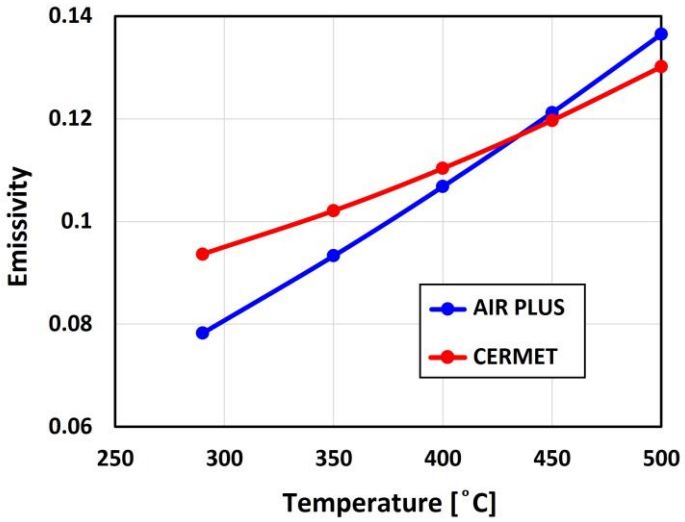

Figure 4.2: Emissivity of the two coatings as a function of temperature considered for evacuated and non-evacuated tubes.

4.3 Methodology

Figure 4.3 outlines the global view of the methodology implemented in this study to conduct a comprehensive assessment of linear CSP technologies from comprising optical, thermal and economic perspectives. In order to carry out a comparative economic analysis based on the LCOE (Section 4.6), essential requisites include cost data and net annual energy yield. While cost data can be collected from existing literature, net annual energy yield must be determined by a specific approach. In this respect, a one-dimensional thermal model was developed to solve the energy balance for the HTF along the receiver axis (Section 4.5.1). This model considers hourly ambient temperature, wind speed and DNI data as the input data for the whole year. Boundary conditions for this 1D model include a thermal driver and heat losses. The thermal driver, consisting of the solar power incident on the receiver tube, is provided by using an optical ray-tracing model developed by a ray-tracing code (Tonatiuh) computing the incident angle modifier (IAM) and the reference optical efficiency for a given PTC or LFC plant (Section 4.4). Regarding heat losses, a steady-state lumped-parameter model, presented in Section 3.4, was developed in the radial direction to provide an accurate evaluation of heat losses for any given HTF temperature. The boundary conditions required for this model include HTF temperature, mass flow rate, incident solar heat flux, ambient temperature and wind speed. As described, this model relies on correlations to assess heat transfer phenomenon; in particular, the convective heat transfer between

the glass tube and the environment in the case of PTC can be approximated using literature-based correlations for the cylinder in cross flow. However, in the case of LFC, the presence of the secondary concentrator necessitates the development of a CFD model to evaluate convective heat losses (Section 4.5.3).

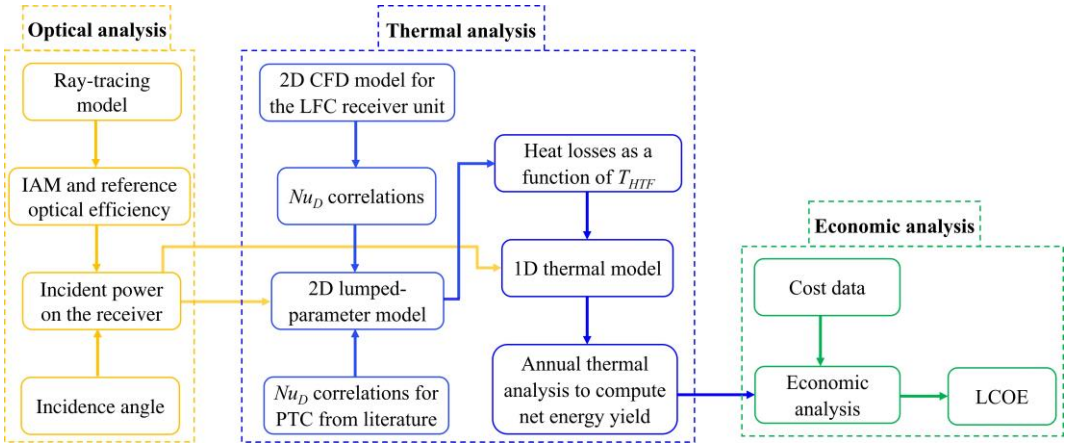

Figure 4.3: Methodology of the techno-economic analysis comprising an optical analysis (Section 4.4), a thermal analysis (Section 4.5) and an economic analysis (Section 4.6).

4.4 Optical analysis

The optical analysis aims at determining the thermal driver for the thermal analysis; particularly, the solar power incident on the absorber tube per unit meter, which can be obtained by

$$q_{inc} = DNI \times A_c \times \eta_0 \times IAM \times \eta_{end} \times \eta_{shd} \times \eta_{cln} \tag{4.1}$$

where DNI is the direct normal irradiance in W/m^2, A_c represents the collector aperture area in m^2, IAM is the incidence angle modifier, η_{end} is the end-loss efficiency, η_{shd} and η_{cln} represent the shadow efficiency and the mirror cleanliness efficiency, respectively (both assumed equal to 1 in this study). The term η_0 is the reference optical efficiency, which is the optical efficiency considering the sun at the zenith. This term can be obtained by an optical ray-tracing model (explained below), and computed using Eq. (4.3) with q_0 equal to the absorbed solar flux with the sun at the zenith.

The end-loss efficiency takes into account the non-irradiated receiver length at the solar field border depending on the sun position. This term can be computed by

$$\eta_{end} = 1 - \frac{F}{L} \times tan(\theta_l) \tag{4.2}$$

where F is the focal length, L is the collector length and θ_l is the longitudinal incidence angle.

The IAM presents the ratio between the optical efficiency (Eq. (4.3)) at a given incidence angle, and the reference optical efficiency, considering equal DNI and aperture width. The IAM is typically divided into the longitudinal component (IAM_L) and the transversal component (IAM_T), as given in Eq. (4.4).

$$\eta_{opt} = \frac{q_0}{DNI \times w} \tag{4.3}$$

$$IAM = IAM_T(\theta_t) \times IAM_L(\theta_l) \tag{4.4}$$

where q_0 is the absorbed solar flux in *W/m*, and w is the mirror aperture width in *m*.

To compute the IAM components and the reference optical efficiency (sun at zenith), an optical ray-tracing model has been developed by using Tonatiuh [137] for both the LFC and PTC systems. This model computes the solar power incident on the absorber tube for any given sun position, considering mirror quality defined through the slope error of the mirror. The model is based on the geometrical and optical properties provided in Table 4.1, except for the collector length, which is 20 m. Moreover, the receiver is 10 m long, and it is translated along the axial direction, depending on the sun position, to maintain the absorber tube in the irradiated area. This removes any border effects, which are not considered in the IAM since they are included in Eq. (4.2). Figure 4.4 shows an example of the LFC optical model.

The reference optical efficiencies for the LFC and the PTC were computed to be 0.839 and 0.878, respectively. Expectedly, the LFC indicates a lower efficiency since it only approximates a parabolic collector. To determine IAM_L and IAM_T, a set of simulations were performed considering the sun belonging to the collector longitudinal and transversal plane, respectively, and changing the sun altitude. Figure 4.5 displays the computed IAM_L and IAM_T as a function of the incidence angle for the PTC and LFC technologies. As shown, the transversal IAM component is always equal to 1 for the PTC system independent of the incidence angle of the sun. This is due to the fact that, while tracking the sun, the normal vector to the PTC aperture is always in the same plane as the solar rays, and therefore, the transversal angle is 0º (±tracking uncertainty).

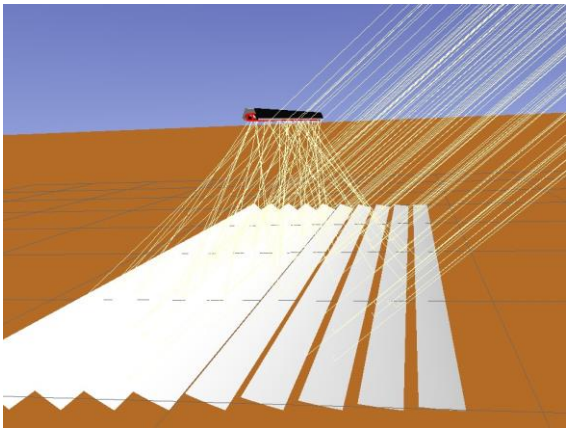

Figure 4.4: The LFC system simulated in Tonatiuh assuming the sun in the east and the sun altitude equal to 40° (number of photons are reduced for visualization purpose).

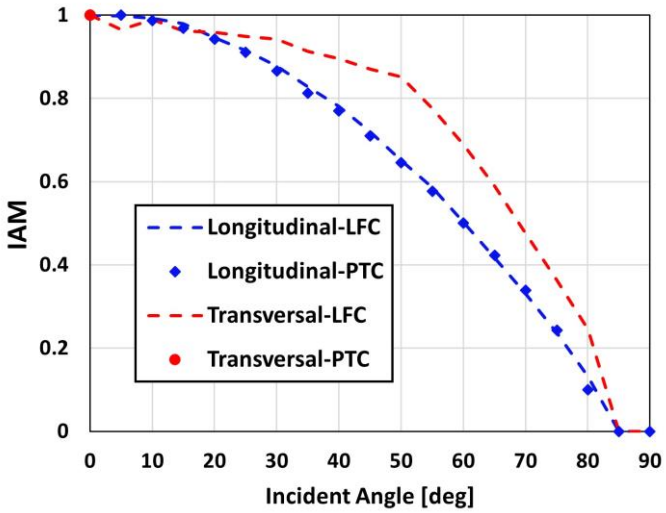

Figure 4.5: Incidence angle modifier components for the LFC and PTC technologies.

4.5 Thermal analysis

The main goal of the thermal analysis is to compute net annual energy yield, which is a crucial parameter for the economic analysis of LFC and PTC. This parameter must be calculated by a 1D model solving the energy balance for the HTF along the axial direction, which is described in Section 4.5.1. The 1D model requires appropriate correlations for heat losses from the absorber tube to the environment, which can be provided by a lumped-parameter model in the radial direction (Section 4.5.2). In the case of the LFC, the lumped-parameter model exploits ad-hoc correlations for the convective heat transfer coefficient obtained by a CFD model simulating the air external flow in the presence of the secondary concentrator

(Section 4.5.3). Finally, net annual energy yields are presented for different technologies in Section 4.5.4.

The thermal performance of the receiver tube can be quantified by means of the thermal efficiency, defined as:

$$\eta_{th} = 1 - \frac{Q_{loss}}{Q_{abs}} \tag{4.5}$$

where Q_{loss} and Q_{abs} represent the heat loss to the environment and the absorbed solar power per unit length, respectively.

4.5.1 1D model for annual-based analysis

To conduct a techno-economic analysis, it is essential to obtain net annual energy yield. In this regard, a 1D model was developed along the axial direction of the receiver tube to solve a steady-state energy balance equation for the HTF, see Eq. (3.6). Although this model has been considered for an annual-based scenario, the steady-state assumption would still be justified since the model continuously regulates mass flow rate based on DNI, keeping the HTF temperature profile consistent along the receiver tube during the daytime.

The 1D model considered in this section is based on the model described in Section 3.5. However, different boundary conditions were applied to this model to simulate an annual-based scenario; instead of implementing a constant mass flow rate, it was consistently regulated based on DNI. This mass flow rate regulation ensures reaching desired outlet HTF temperatures during the day/night for a certain tube length (800 m) and a certain inlet HTF temperature (290 °C). During the night, a minimum outlet HTF temperature of 260 °C was imposed to prevent the molten salt from freezing, keeping it 20 °C higher than the freezing point [138]. Accordingly, the minimum mass flow rate was also computed to meet this outlet temperature. Nevertheless, during the day, the desired outlet temperature would be 500 °C. Once DNI starts to increase in the daytime, HTF outlet temperature increases accordingly to achieve the maximum outlet temperature of 500 °C. Upon reaching this desired temperature, mass flow rate must be regulated continuously based on DNI variations. The strategy adopted for the regulation of mass flow rate consists of a few steps: firstly, the model solves the energy balance equation for the whole receiver tube as a single control volume, implementing the receiver inlet/outlet temperature, mean heat loss and absorbed solar power. This solution would provide an initial estimation of the mass flow rate. This initial guess was then exploited by Eq. (3.6) to calculate the tube length required to reach the desired HTF

temperature at the outlet (500 °C). The deviation between the actual tube length (800 m) and the computed length was employed to refine the previous evaluation of mass flow rate. The solution was repeated to obtain a new tube length adopting the updated mass flow rate. This procedure continued until achieving a computed length equal to the actual length of the receiver tube, implying the accurate value of mass flow rate for a given DNI. Thanks to an appropriate initial guess, three iterations would be enough to attain a convergence in the solution.

In order to calculate net annual energy yield, i.e., net annual electricity output, by the 1D model, the efficiency of the power cycle was assumed to be 38% in this study. This value corresponds to a Rankine cycle considering a maximum HTF temperature of 500 °C [52,139].

The 1D model exploits the results of the optical model in terms of incident solar flux (to obtain absorbed solar flux) described in Section 4.4, and of the lumped-parameter model in terms of heat losses, as presented in Section 4.5.4.

4.5.2 Lumped-parameter model of the linear Fresnel receiver unit

The lumped-parameter model provides correlations of heat losses from the absorber tube to the external environment to be employed by the 1D model. The lumped-parameter model considered in this section is the same as the model already presented in Section 3.4, developed based on correlations to evaluate heat transfer phenomenon. As described in Section 4.3, while the convective heat transfer between the glass tube and the environment can be approximated using literature-based correlations for the cylinder in cross flow in the case of PTC, it needs ad-hoc correlations in the case of LFC due to the presence of the secondary concentrator. These correlations were provided by a CFD model developed for the LFC receiver unit, investigating natural and forced convection (see Section 4.5.3).

4.5.3 Computational fluid dynamics (CFD) model of the linear Fresnel receiver unit

The LFC receiver unit was investigated by a 2D steady-state CFD model using the STAR-CCM + software [140]. The computational domain includes the external air flow and the CPC unit, as shown in Figure 4.6; therefore, it does not include the receiver tube consisting of the absorber tube encapsulated in a glass envelope, and the internal oil flow. The presence of the receiver tube was replaced by a boundary condition applied on the glass outer surface, where a uniform temperature is

imposed. The latter is a valid assumption because of the slight temperature difference in the azimuthal direction within the glass envelope [71]. On the left side of the computational domain, the transversal wind speed is imposed together with the (ambient) temperature of the incoming air, while in the opposite side of the domain the ambient pressure is imposed by means of a "pressure outlet" boundary condition. It can be noted that the receiver unit is not placed in the center of the external air domain, but it has been put towards the inlet section of the wind to ensure that the vortices released downstream the receiver unit are solved within the computational domain. In the case of no wind (pure natural convection), the ambient pressure is imposed on the top and the bottom sides of the domain, while the left and the right sides are set to be symmetry planes. The air inside the CPC was kept at the atmospheric pressure.

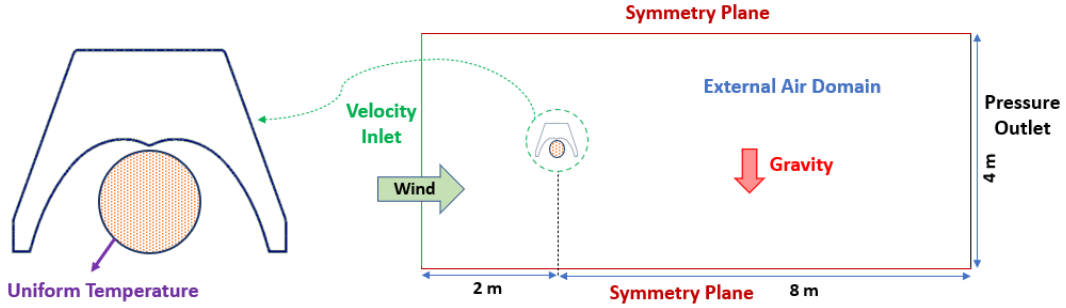

Figure 4.6: Computational domain and boundary conditions of the CFD model

The computational domain was discretized generating a mesh consisting of polygonal cells. The mesh was structured to be more refined close to the receiver unit in order to ensure the accurate solution of the velocity and thermal gradients at the near-wall regions. The mesh was also structured with different sizes in the whole domain to capture the vortices established close and downstream the receiver. A mesh sensitivity analysis was conducted and the minimum number of polygonal cells in the domain to achieve mesh independent results was 1.9×10^5. The adopted computational mesh is illustrated in Figure 4.7.

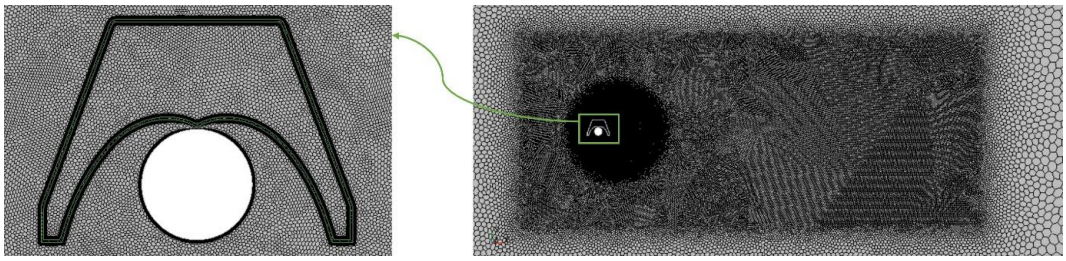

Figure 4.7: Generated mesh for the CFD model

In order to simulate the turbulence for the two cases, the SST k-ω (Menter) turbulence model [141] was applied to the air regions, which is the appropriate model to simulate air flows around complex shapes [142]. The effect of the gravity has also been considered in the model.

The CFD model was exploited to obtain appropriate correlations for the convective heat transfer between the glass and the environment in terms of Nusselt number. This study includes natural convection (absence of wind) and forced convection (presence of wind). Once the Nusselt number (Nu_D) is obtained, the convective heat transfer coefficient can be determined by using Eq. (4.6):

$$h = \frac{k}{D} Nu_D \tag{4.6}$$

where k is the thermal conductivity at film temperature in *W/m.K* and D is the outer diameter of the receiver tube.

In this regard, a wide parametric space was considered for the CFD analysis in terms of wind speed, ambient temperature and glass temperature. The specified limits for these parameters are provided in Table 4.3. Regarding wind speed and ambient temperature, the ranges of values were determined according to the meteorological data of the reference locations considered in this study (refer to Figure 4.19). For the glass temperature, the range was specified based on the HTF operating temperature in this study (290-500 °C).

Table 4.3: Ranges of values for the parameters in the CFD model

Parameter	Minimum value	Maximum value
V_w (m/s)	0	10
T_{amb} (K)	273	313
T_{glass} (K)	300	450

The results of the CFD model are represented for natural and forced convection in Section 4.5.3.1 and 4.5.3.2 respectively.

4.5.3.1 Natural convection

The results of the CFD model for the case of natural convection (absence of wind) have been first verified against the correlations provided for natural convection around a long horizontal circular cylinder by Churchill and Chu (Eq. (4.7)) and by Morgan (Eq. (4.8)) [67]. To perform this comparison, the CPC was removed from the computational domain.

$$Nu_D = \left\{0.60 + \frac{0.387\, Ra_D^{1/6}}{[1 + (0.559/Pr)^{9/16}]^{8/27}}\right\}^2 \tag{4.7}$$

$$Nu_D = C\, Ra_D^n \tag{4.8}$$

where Ra_D is the Rayleigh number based on the glass outer diameter, Pr represents the Prandtl number at film temperature, C and n are given in [67].

Figure 4.8 represents comparisons between the Nusselt numbers computed by the CFD model and those obtained by the two correlations for natural convection around a cylinder. This comparison was performed considering five different combinations of the parameters in Table 4.3 that result in as many values of the Rayleigh number. As can be seen, the Nusselt numbers obtained by the CFD model are in good agreement with those provided by the two correlations. The maximum deviation between the results of the CFD model and those of the two correlations is about 7.76%, which is quite acceptable since, according to [67], the error bar for the correlations is about 20% (as shown in Figure 4.8).

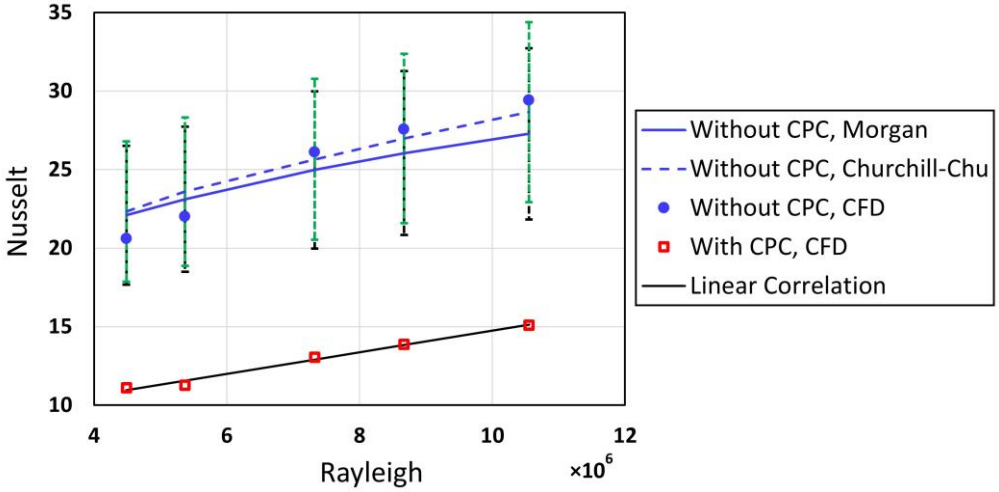

Figure 4.8: Nusselt vs. Rayleigh numbers in the case of the Fresnel collector: Comparison of the CFD model results against the results of two correlations for natural convection around a circular cylinder (green dotted-line for Churchill-Chu and black dotted-line for Morgan), with the respective error bars.

At this point, the CPC was reintroduced in the computational domain to simulate the Fresnel receiver unit. Figure 4.9a demonstrates the air velocity field for the whole computational domain, and Figure 4.9b shows it focusing on the regions around the receiver unit for an ambient temperature of 293 K and an imposed glass temperature of 325 K. As expected, the velocity magnitude is extremely low due to the absence of the wind. The impact of the presence of the CPC is clearly observed in the contour of velocity around and above the receiver unit. However, the velocity field is not completely symmetric in this region since the solution shows rather periodic behavior intrinsically. The air temperature field around the receiver unit is depicted in Figure 4.9c. As can be seen, the imposed uniform temperature of the glass wall keeps the air under the CPC hotter compared to the other regions in the external air domain. The secondary concentrator acts as an obstacle for the hot air moving upward, which is trapped under the CPC. This should lead to a reduced heat loss by convection from the glass envelope.

The CFD model of the Fresnel case was run again considering the same Rayleigh numbers as the previous case. The computed Nusselt numbers with and without the CPC unit are displayed in Figure 4.8; as expected, a significant difference can be detected. The obtained Nusselt numbers are considerably lower for the Fresnel case because of lower convective heat transfer around the glass cover in the presence of the CPC unit. As shown in Figure 4.8, in the Fresnel case a linear equation can be found for the Nusselt number as a function of the Rayleigh number. This linear correlation well explains the data with the coefficient of determination (R^2) about 0.99, which is expressed as:

$$\overline{\boldsymbol{Nu}}_{\boldsymbol{D}} = \mathbf{6.90 \times 10^{-7}} \boldsymbol{Ra}_{\boldsymbol{D}} + \mathbf{7.85} \tag{4.9}$$

4.5.3.2 Forced convection

Similarly, in the case of forced convection, the CFD model was initially compared with a well-established correlation found in literature for the cylinder in cross flow, excluding the CPC. In this respect, the Zhukauskas' correlation [67] was considered, which is expressed as:

$$\overline{Nu}_D = C\, Re_D^m\, Pr_a^n \left(\frac{Pr_a}{Pr_g}\right)^{1/4} \tag{4.10}$$

where Re_D represents the Reynolds number based on the glass outer diameter, Pr_a and Pr_g are the Prandtl numbers at the atmospheric and the glass temperatures respectively, C, m and n are given in [67] as a function of *Re* and *Pr* numbers.

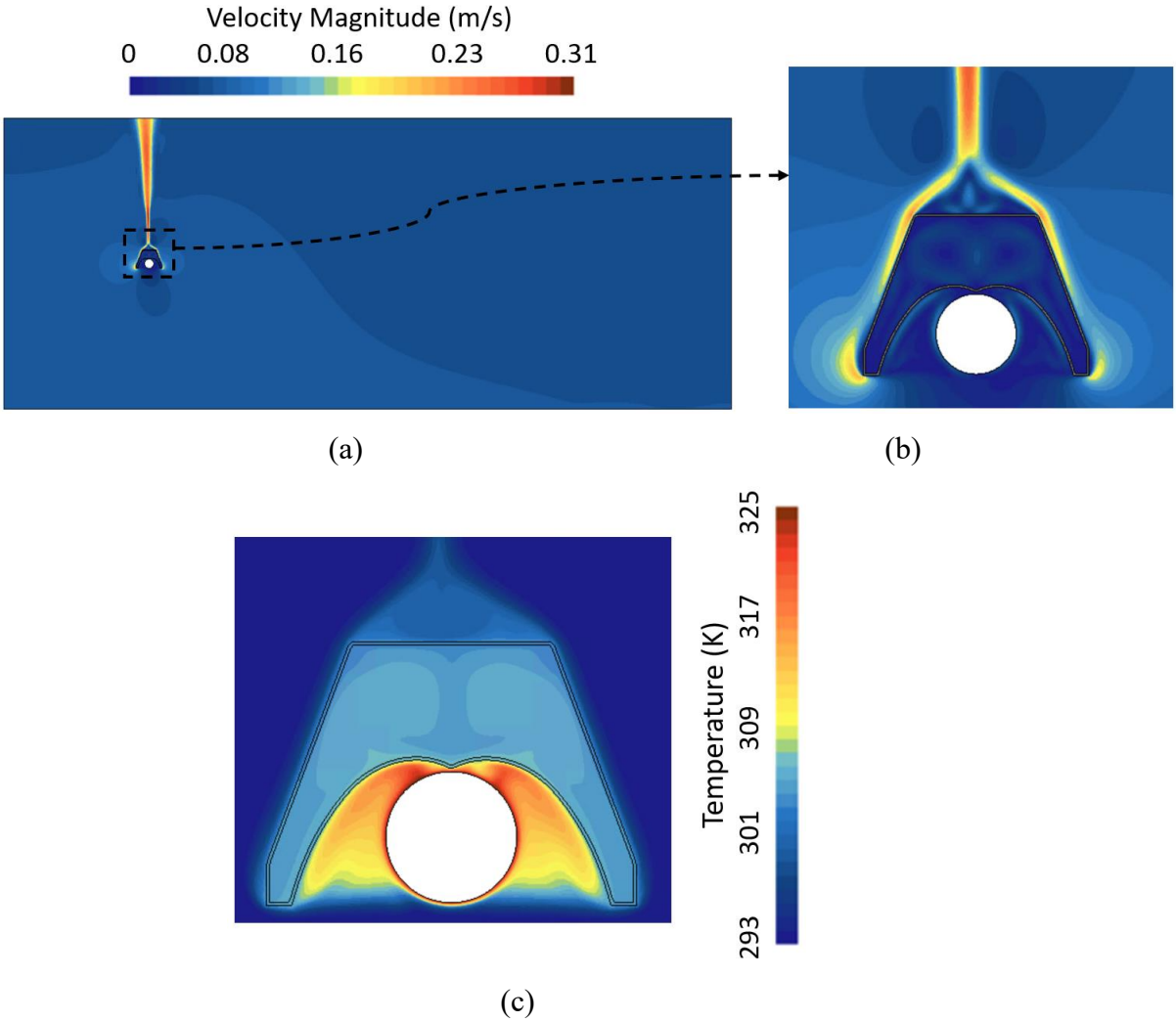

Figure 4.9. Results of the CFD model in the case of absence of wind for an ambient temperature of 293 K and a glass temperature of 325 K: (a) contour of velocity magnitude in the whole computational domain, (b) contour of velocity magnitude focusing on the receiver unit, (c) air temperature field.

Figure 4.10 compares the Nusselt numbers computed by the present CFD model and those obtained by the Zhukauskas' correlation. This comparison was performed considering 12 different combinations of the parameters provided in Table 4.3 that result in as many values of the Reynolds number. As shown in Figure 4.10, the CFD model reproduces well the Nusselt numbers obtained by the

Zhukauskas' correlation for different Reynolds numbers. The maximum deviation between the CFD model and the correlation is about 9.49%, which is quite acceptable since the error bar for this correlation is about 20% (as shown in Figure 4.10), according to [67].

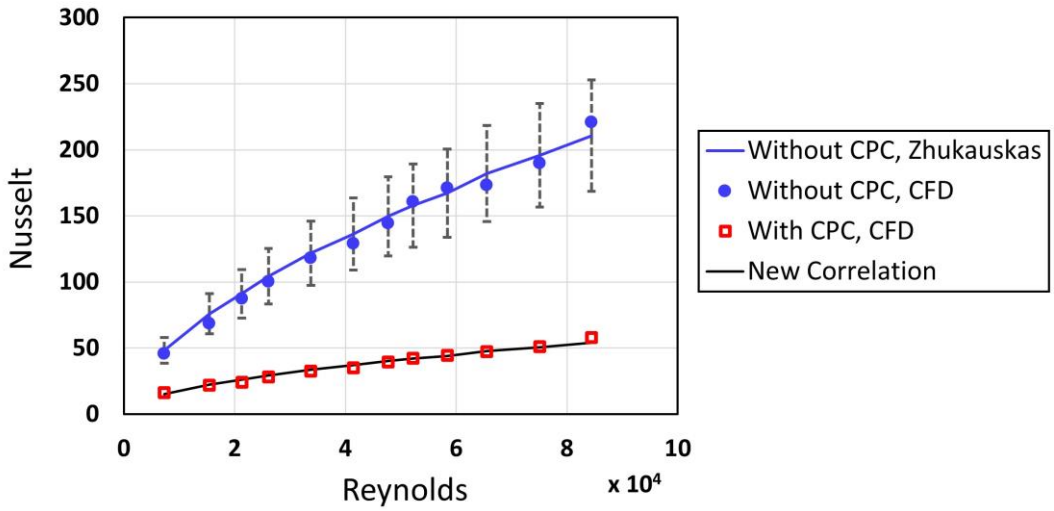

Figure 4.10: Comparison of the CFD model and the Zhukauskas' correlation for the cylinder in cross flow with the respective error bars, and obtained Nusselt numbers in the case of the Fresnel collector.

At this point, the CPC was reintroduced in the computational domain to simulate the Fresnel receiver unit. Figure 4.11a shows the computed air velocity magnitude contours in the whole computational domain, and Figure 4.11b displays it focusing on the receiver unit for a wind speed of 6 m/s, which is a reasonable value at ground level, an ambient temperature of 288 K and a glass temperature of 370 K. As can be observed, the velocity contours above and below the receiver unit are rather symmetrical and the computational domain is large enough to cover the whole turbulent regions well. The stagnation point, as expected, is established on the side of the CPC unit hit first by the wind, while the separated region is established behind the receiver unit. The CPC unit actually shields the receiver tube against the wind, which results in a very low speed of the air surrounding the receiver. Therefore, the presence of the CPC unit determines a semi-cavity effect.

The contour of the air temperature around the receiver unit is illustrated in Figure 4.11c. Expectedly, the air temperature is higher close to the glass tube, which is hotter than the ambient air. The semi-cavity effect provided by the CPC unit can be appreciated, which reduces the replacing of the heated air close to the receiver

with fresh air at ambient temperature. The hot air stratifies on the top of the glass cover, where it is trapped by the presence of the secondary reflector. The expected effect is a remarkable reduction of the heat lost by convection from the glass tube towards the environment, especially on the top side of the glass because of the higher air temperatures.

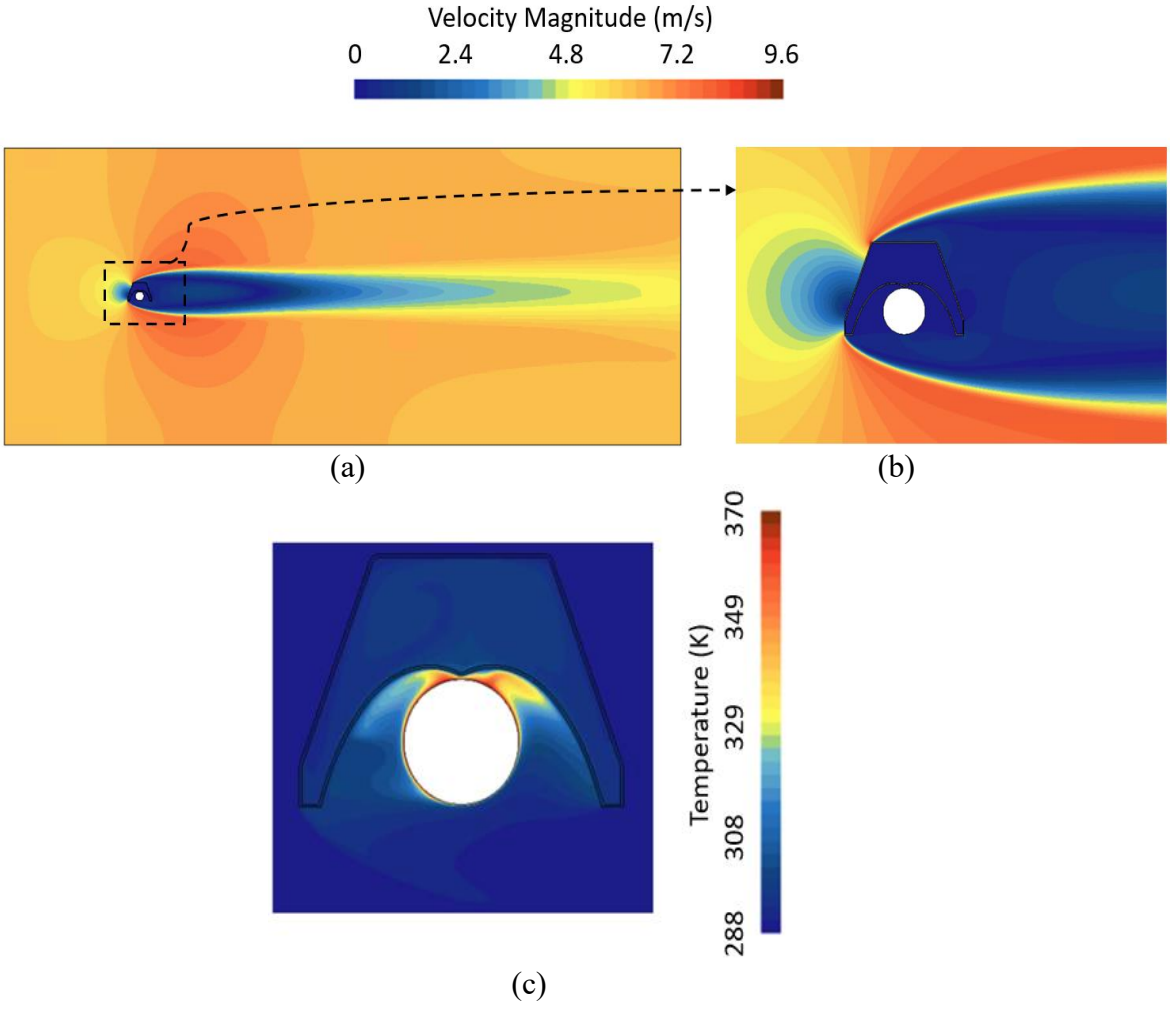

Figure 4.11. Results of CFD model for a wind speed of 6 m/s, an ambient temperature of 288 K and a glass temperature of 370 K: (a) contour of velocity magnitude in the whole computational domain, (b) contour of velocity magnitude focusing on the receiver unit, (c) air temperature field.

The CFD model of the Fresnel case was run again considering the same Reynolds numbers as the previous case. Figure 4.10 displays the Nusselt numbers computed with and without the CPC unit. According to what discussed above (Figure 4.11), the Nusselt number is significantly lower in the presence of the CPC

unit. This is due to a lower convective heat transfer around the glass envelope provided by the CPC semi-cavity effect. This difference is more significant for forced convection compared to natural convection (Figure 4.8 vs. Figure 4.10) owing to major variation in the heat transfer coefficient at higher air velocity magnitude; However, in terms of percentage, the difference is relatively comparable (~50% vs. ~70% on average for natural and forced convection, respectively).

To develop an appropriate correlation for the Fresnel case, the format of the Zhukauskas correlation (Eq. (4.10)) was considered. Then, the coefficients C, m and n were determined based on the results of the CFD model for the Fresnel receiver unit. In this regard, with the best interpolation of the data, the coefficients C, m and n were computed to be 0.165, 0.52 and 0.37, respectively. The coefficient of determination (R^2) for this approximation is about 0.99, which represents a sufficient accuracy. Therefore, the new correlation for the Fresnel case can be expressed as:

$$\overline{Nu}_D = 0.165\, Re_D^{0.52}\, Pr_a^{0.37} \left(\frac{Pr_a}{Pr_g}\right)^{1/4} \tag{4.11}$$

4.5.4 Results of the thermal analysis

Figure 4.12 compares radiative heat losses computed by the lumped-parameter model for various configurations considering wind speeds of 0 m/s (natural convection) and 10 m/s (extreme wind effects). As shown, the radiative heat loss is slightly higher for the evacuated tubes at lower HTF temperatures. This is because the selective coating applied in the case of the evacuated tube (CERMET) presents a higher emissivity at low temperatures with respect to the case of the coating stable in air (see Figure 4.2). Figure 4.12 also suggests that the radiative heat loss is weakly affected by the wind and by the receiver technology (PTC or LFC). This is because the absorber tube temperature does not change appreciably with the wind and with the receiver technology (see Figure 4.13); it is mostly determined by the imposed temperature of the HTF because the heat transfer coefficient between the absorber tube and the HTF is substantially higher than that between the absorber tube and the gap region.

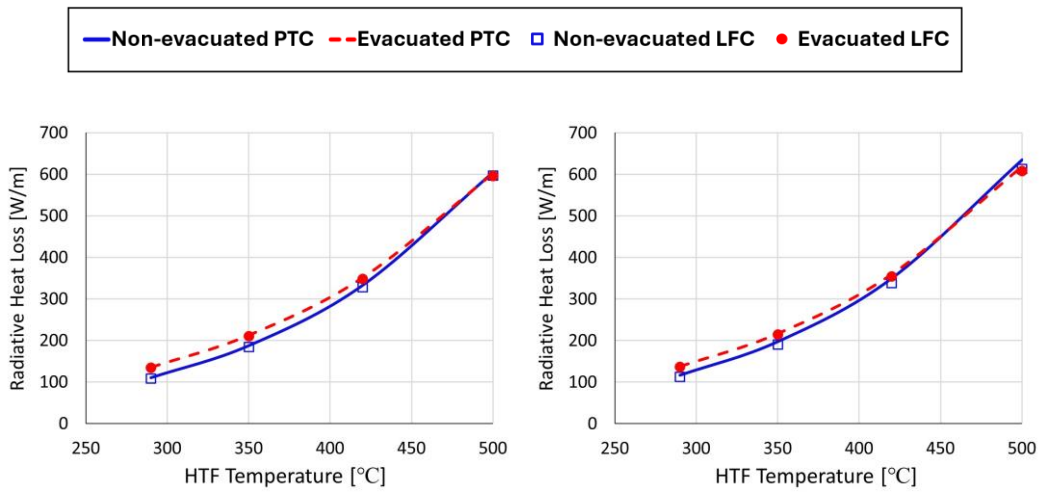

Figure 4.12: Radiative heat loss from the absorber tube for different technologies considering wind speeds of (a) 0 m/s and (b) 10 m/s.

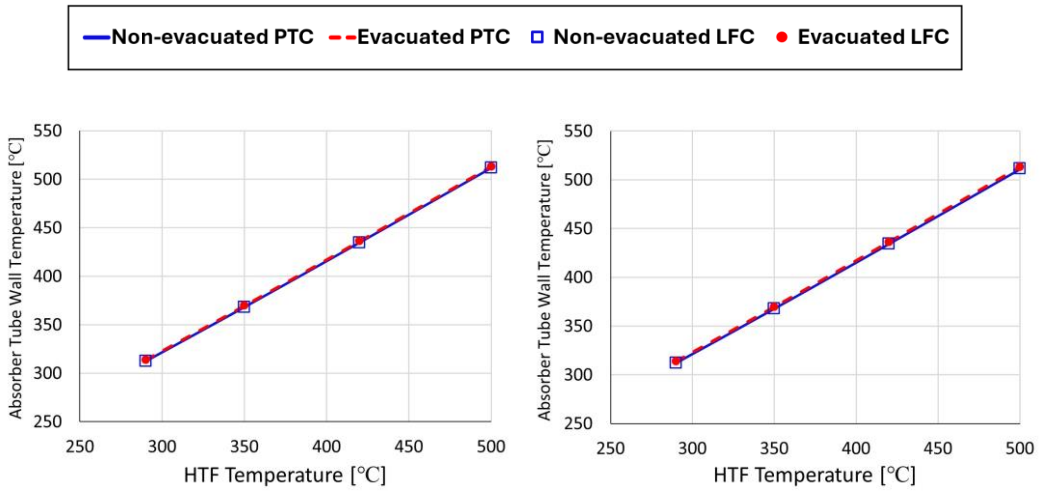

Figure 4.13: Absorber tube wall temperature with respect to HTF temperature for various technologies considering wind speeds of (a) 0 m/s and (b) 10 m/s.

Figure 4.14 compares convective heat losses for various configurations considering wind speeds of 0 and 10 m/s. As expected, evacuating the receiver tube is very effective in reducing the convective heat losses, which is nearly zero in all the cases. Particularly, the thermal insulation provided by the vacuum in the gap makes the effect of the wind on the convective heat loss negligible. Regarding non-

evacuated tubes, the LFC presents less convective heat losses than the PTC, which is a consequence of the semi-cavity effect provided by the secondary concentrator (refer to Section 4.5.3). Furthermore, it can be noticed from Figure 4.14 that the presence of the wind leads to a relatively considerable increase of the convective heat losses. However, the wind effect is less noticeable for the LFC receiver, taking advantage of the protection offered by the CPC, while the PTC receiver is directly exposed to the external air flow. The semi-cavity effect can also be appreciated looking at the glass temperature (Figure 4.15), which is higher in the case of the LFC receiver because of the reduced replacement of hot air with fresh air at ambient temperature close to the receiver.

Now, total heat losses can be presented, equal to the sum of the radiative and convective heat losses. Figure 4.16 depicts total heat losses for various technologies considering wind speeds of 0 and 10 m/s. As discussed above, differences in total heat losses among the configurations mainly arise from the convective share. As a result, non-evacuated tubes dissipate greater heat losses in total compared to evacuated ones, and non-evacuated PTC demonstrates higher total heat losses compared to non-evacuated LFC.

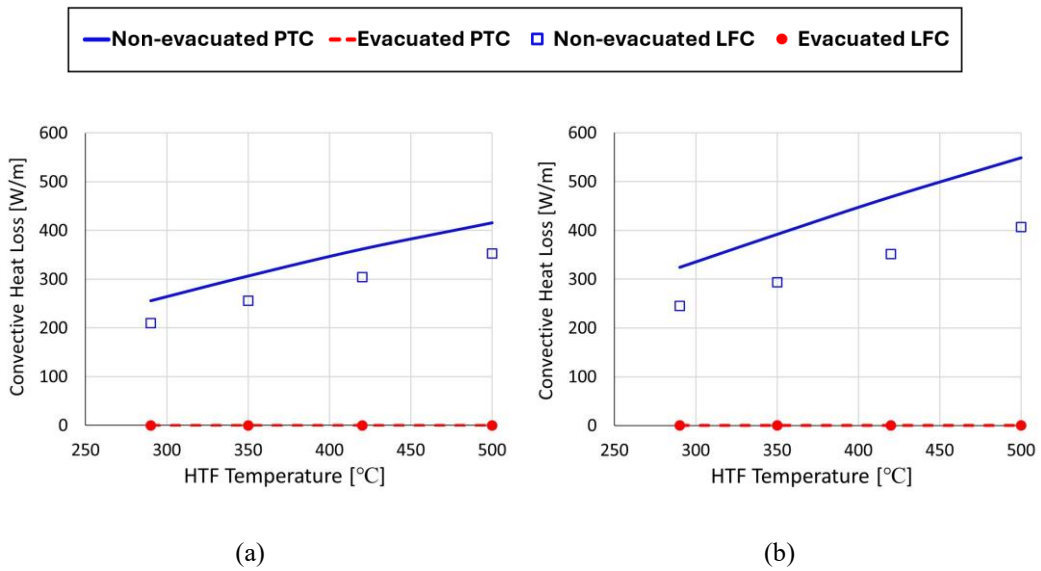

Figure 4.14: Convective heat loss from the absorber tube for different configurations considering wind speeds of (a) 0 m/s and (b) 10 m/s.

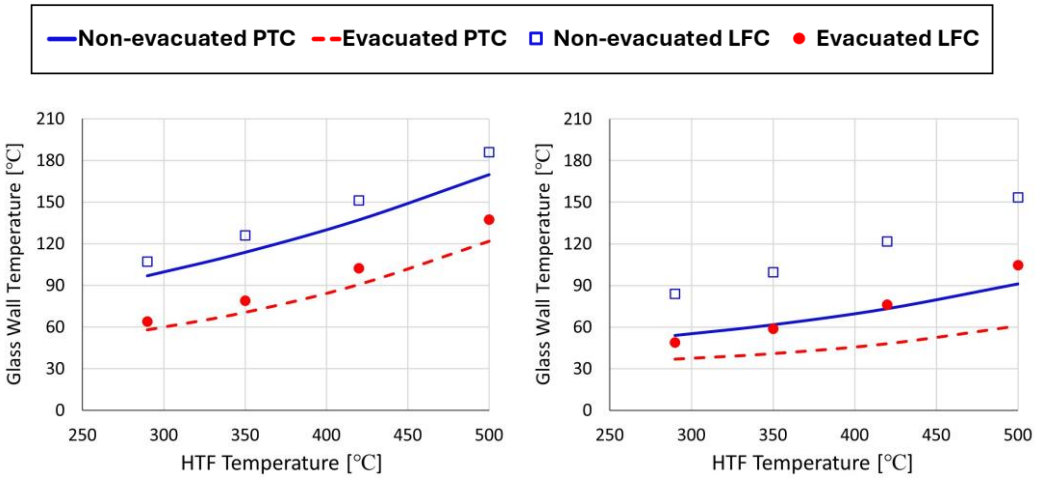

Figure 4.15: Glass wall temperature for various configurations considering wind speeds of (a) 0 m/s and (b) 10 m/s.

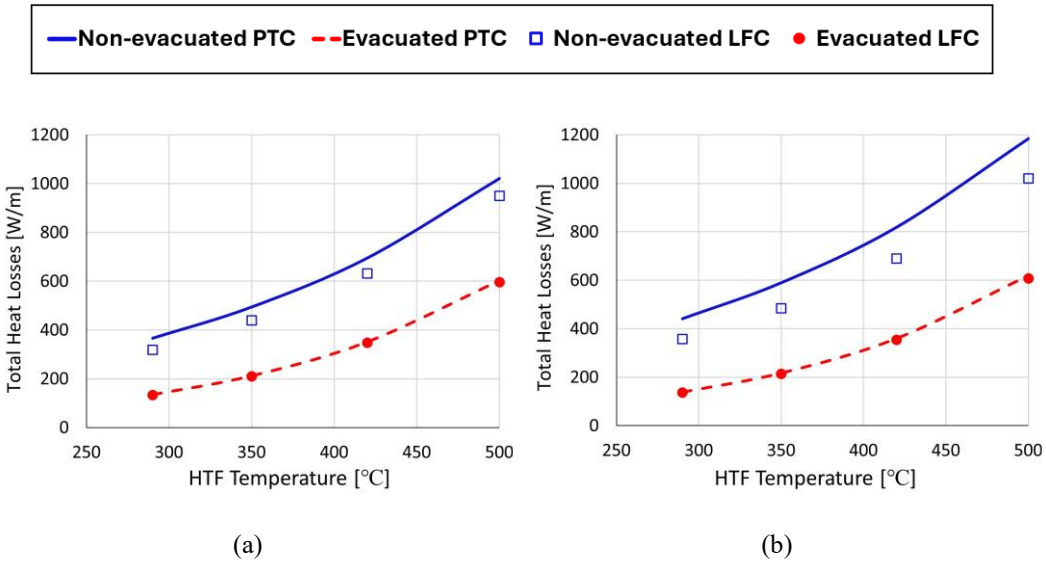

Figure 4.16: Total heat losses from the absorber tube for different configurations considering wind speeds of (a) 0 m/s and (b) 10 m/s.

Figure 4.16 signifies correlations of heat losses to be obtained as a function of HTF temperature. Table 4.4 provides the coefficients of heat losses correlations (a, b and c in Eq. (3.5)) for various configurations considering wind speeds of 0 and 10 m/s.

Table 4.4: Coefficients of heat losses correlations (see Eq. (3.5)) for various configurations, obtained by the lumped-parameter model for wind speeds of 0 and 10 m/s.

Technology	$V_w = 0$ m/s			$V_w = 10$ m/s		
	a	b	c	a	b	c
Non-evacuated PTC	0.00705	-6.307	1684.1	0.00759	-6.619	1760.9
Evacuated PTC	0.00671	-6.755	1812	0.00699	-7.056	1896.9
Non-evacuated LFC	0.00702	-6.383	1689.2	0.00729	-6.598	1762.4
Evacuated LFC	0.00663	-6.665	1787	0.00678	-6.822	1830.3

The correlations of heat losses provided in Table 4.4 have been employed by the 1D model to perform an annual-based analysis. In this regard, the 1D model focuses on the thermal performance of various configurations and evaluates the net annual energy yield.

The meteorological data (DNI, wind speed and ambient temperature) are illustrated in Figure 4.17 for a reference location (Karas, Namibia) and for a reference day (13 November) with high DNI values during the daytime characterized by considerable fluctuations, and the thermal performances of the systems are shown in Figure 4.18 considering this reference case. As shown in Figure 4.18a, the receiver outlet temperature starts increasing early in the morning because of the increase of the DNI (Figure 4.17). However, the temperature increase exhibits a delay for the LFC owing to its optical performance as the LFC is affected by the transversal effects early in the morning when the incidence angle is higher (refer to Figure 4.5). The temperature rise is more pronounced for evacuated tubes due to a lower heat loss compared to non-evacuated tubes (Figure 4.18c). This higher heat loss from non-evacuated tubes also results in lower thermal efficiencies during the daytime compared to evacuated tubes (Figure 4.18d). Once the receiver outlet fluid attains the desired temperature (500 °C), the mass flow rate begins to increase, continuously regulated based on DNI values during the daytime (Figure 4.18b). A higher minimum mass flow rate is required for non-evacuated tubes due to a more significant temperature drop along the receiver tube during the night caused by higher heat losses.

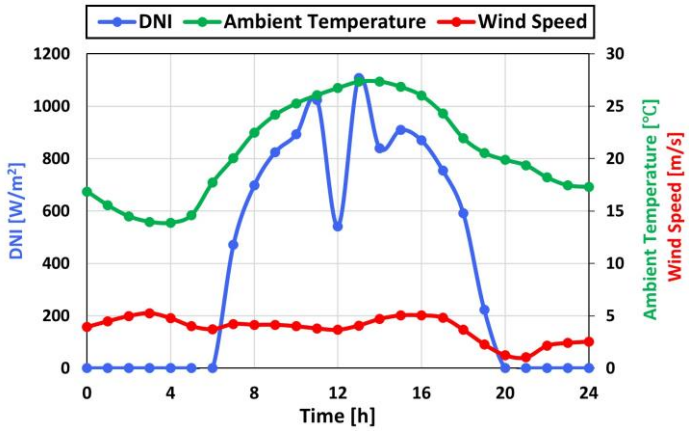

Figure 4.17: Meteorological data comprising DNI, wind speed and ambient temperature for a reference location (Karas, Namibia) and a reference day (13 November).

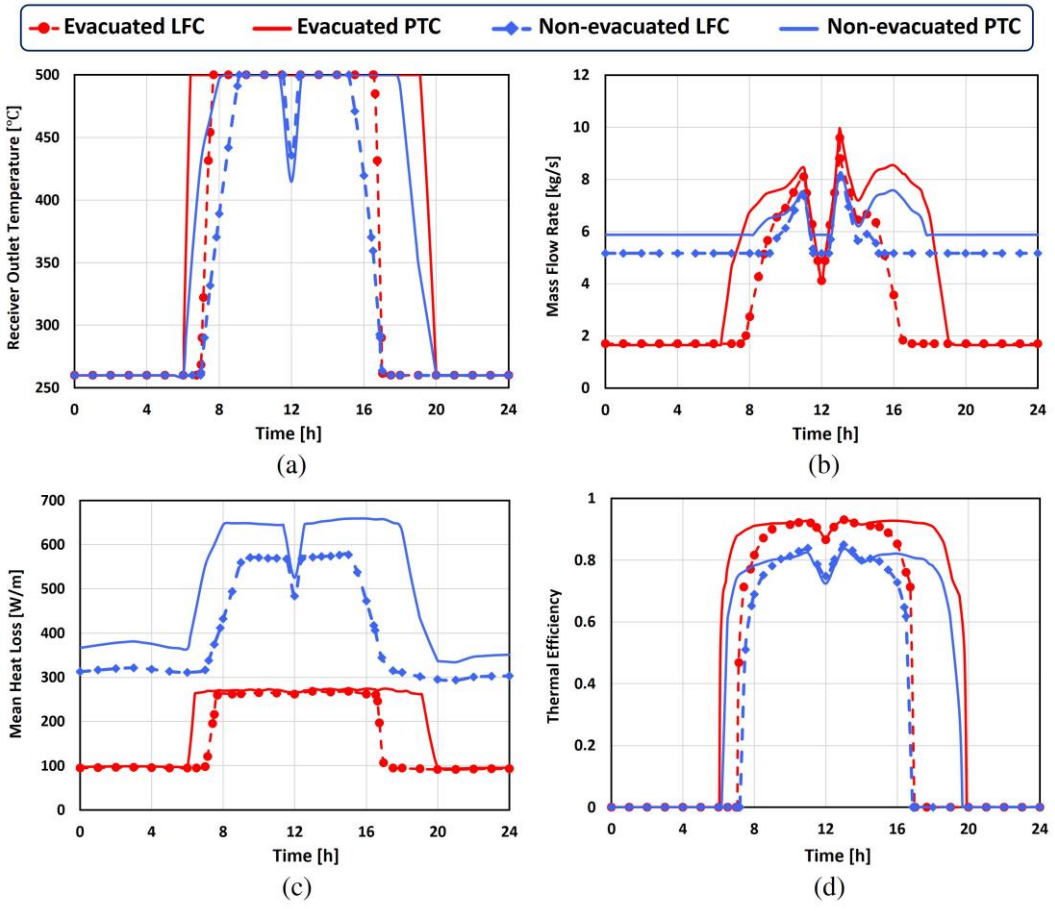

Figure 4.18: Thermal performance of various configurations during a reference day (13 November) in terms of: (a) HTF outlet temperature, (b) mass flow rate, (c) mean heat loss, and (d) thermal efficiency.

To perform an annual-based comparison, the 1D model explained in section 4.5.1 was employed. In this regard, hourly meteorological data of different locations were considered to compute net annual energy yield by employing an hour-by-hour simulation. For this purpose, the assumptions and the boundary conditions described in section 4.5.1 were applied to the 1D model to simulate an annual-based scenario. The model was developed using the Modelica language. The hourly meteorological data, including DNI [W/m^2], ambient temperature [°C], and wind speed [m/s] were implemented in the model for each location. In this study, four different geographical regions of the world were considered. Figure 4.19 depicts the monthly values of the meteorological data for the reference locations, namely, Calama (Chile), Karas (Namibia), Leinster (Australia) and Adam (Oman) (data from [143]). The highest and the lowest yearly solar direct beam potentials are observed in Chile (3409 kWh/m^2) and Oman (2183 kWh/m^2), respectively. The latitudes of the locations are as follows: Calama (Chile) at 22.49° S, Karas (Namibia) at 25.63° S, Leinster (Australia) at 27.79° S and Adam (Oman) at 22.51° N.

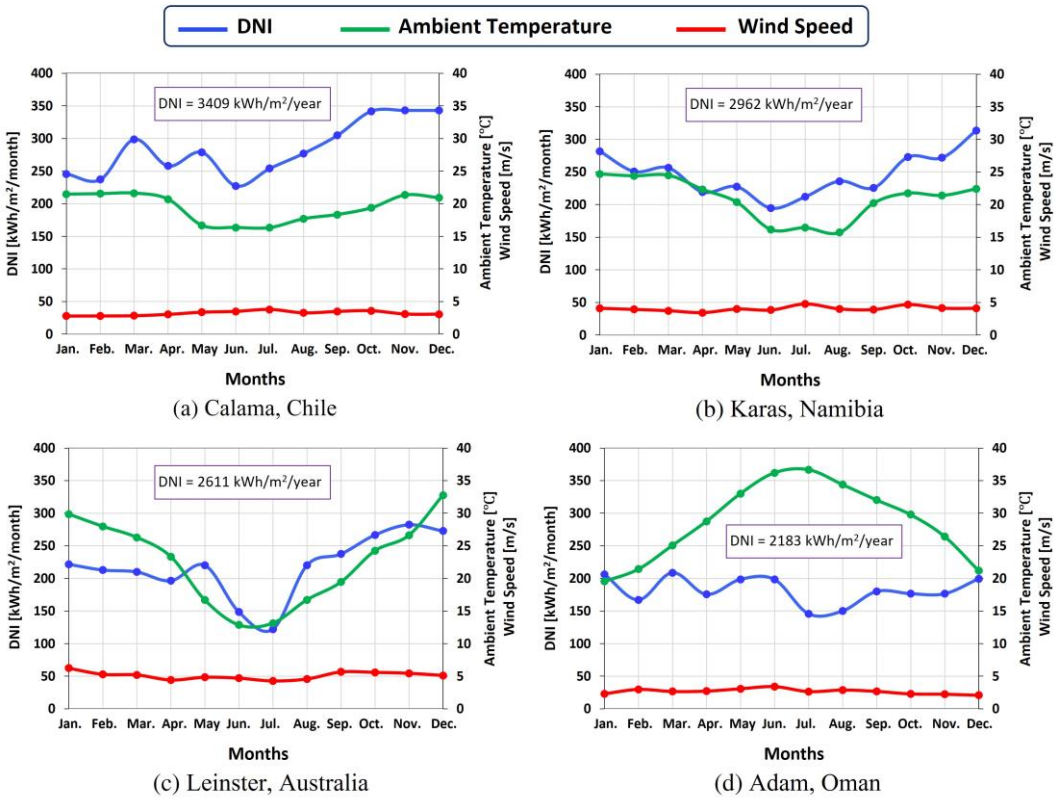

Figure 4.19: Reference meteorological data for different locations under investigation.

Net monthly energy yield is shown in Figure 4.20 for the reference locations. With regard to the N-S alignment of the collector, during the summer months, receiver tubes experience longer duration of high (transversal) angle sunlight early in the morning and late in afternoon. This phenomenon significantly impacts on the optical performance of the LFC during this period, in contrast to the PTC which is not influenced by this phenomenon (refer to Figure 4.5). Consequently, PTC performs more efficiently at the beginning/end of the year in locations situated in the southern hemisphere, as shown in Figure 4.20. Nevertheless, the reference location in Oman, closer to the equator, experiences slight fluctuations in daytime duration throughout the year. This fact leads to a more balanced ratio of PTC/LFC in terms of the net monthly energy yield for this location. Moreover, consistent variations can be observed throughout the year for evacuated and non-evacuated tubes of each individual technology (PTC or LFC), irrespective of the location. This uniformity is caused by the nearly constant difference in the thermal performance of evacuated and non-evacuated tubes due to the same wind speed patterns throughout the year for both tubes regarding each location (refer to Figure 4.19).

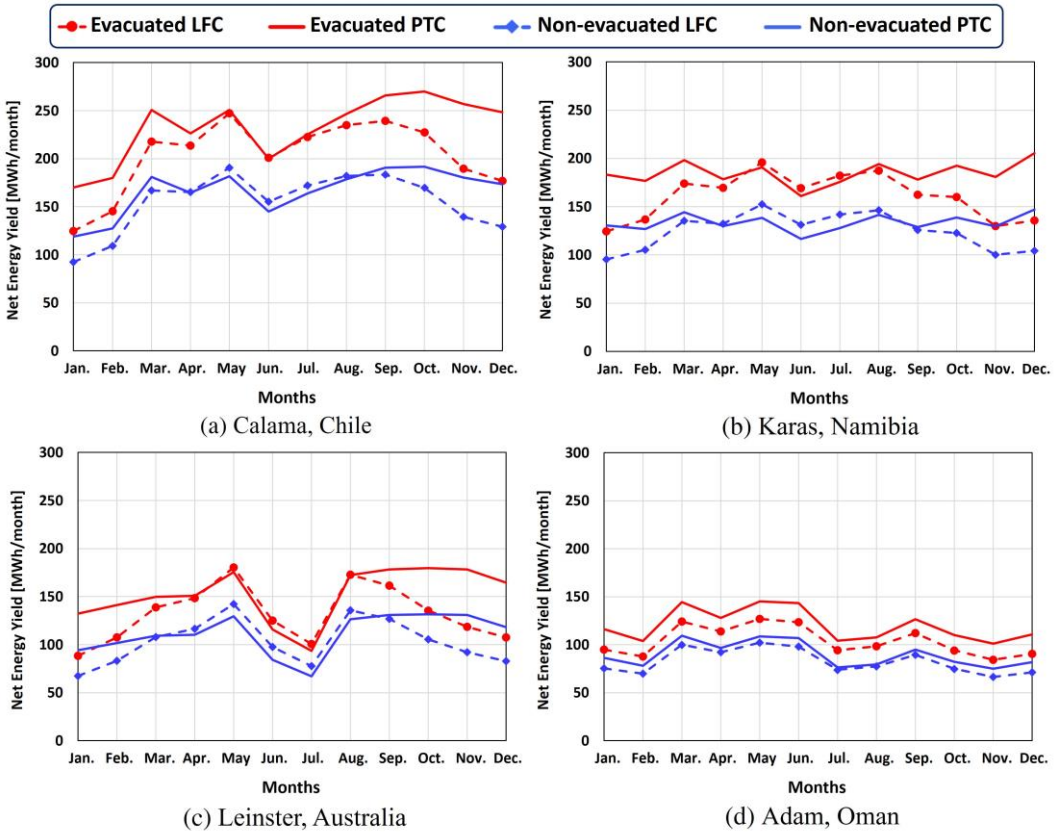

Figure 4.20: Net monthly energy yield computed for the reference locations

Net annual energy yields are outlined in Figure 4.21 for the reference locations and for the different technologies. Expectedly, the evacuated tube yields a greater net annual energy compared to the non-evacuated tube, attributed to lower heat losses provided by the evacuation. This fact applies to both LFC/PTC technologies, regardless of the geographical location. The PTC provides higher net annual energy yield for both evacuated/non-evacuated tubes, which is mainly due to a more efficient optical performance compared to the LFC. However, the advantage of the PTC over the LFC is less considerable than the performance improvement achieved by utilizing an evacuated tube rather than a non-evacuated one. Furthermore, the difference between the net annual energy yield generated by the PTC and that of the LFC is less notable for the non-evacuated tubes compared to the evacuated ones for each location. This is due to the fact that the LFC receiver tube is shielded against wind by the secondary concentrator. As a result, the LFC is less affected by the convective heat loss, which instead considerably influences the PTC without the thermal insulation provided by the vacuum.

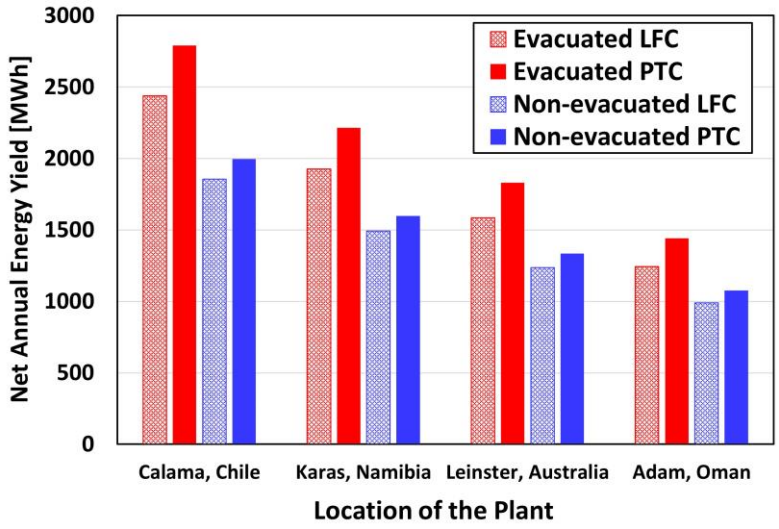

Figure 4.21: Net annual energy yield computed for the reference locations considering different configurations.

By comparing various locations, it can be concluded that the ratio of net annual energy yield obtained by non-evacuated tubes to that of evacuated tubes is almost equal across the locations (about 0.72 for the PTC). This arises due to the nearly identical wind speeds for different locations throughout the year (Figure 4.19), which leads to a negligible impact of the location on the difference between the two technologies in terms of the thermal performance. Furthermore, the ratio of LFC to

PTC in terms of the net annual energy yield is also unaffected by the location (about 0.86) because of a consistent proportional optical performance. As expected, the net annual energy yield aligns with the DNI values (Figure 4.19).

4.6 Economic analysis

In order to conduct a thorough comparison of different linear CSP technologies (PTC or LFC with evacuated or non-evacuated receiver tubes), an economic analysis was performed by exploiting the thermal analysis results in terms of the net annual energy yield. The economic feasibility assessment conducted in this work is based on the cost data outlined in Table 4.5.

Table 4.5: Assumed cost data for the economic analysis

Parameter	Value	Reference
PTC Solar field (€/m^2)	161 *	[90,144]
LFC Solar field (€/m^2)	138 *	[145,146]
Evacuation of the tube (€/m)	32	[88]
Site improvement (€/m^2)	18 *	[145,146]
HTF system (€/m^2)	43 *	[145,146]
Power block (€/kW_e)	1010 *	[145,146]
TES system (€/kWh_t)	29 *	[145,146]
Contingency (% of direct cost)	7	[43,89]
EPC and owner cost (% of direct cost)	10	[43,89]
Discount rate	0.1	[147–149]
Useful life of the plant (years)	30	[147–149]
Annual cost of O&M (% of CAPEX)	2	[147–149]

** Currency conversion (30.08.2023): 1.00 € ↔ 1.09 $*

It should be noted that although economic parameters may vary across the locations due to factors such as labor cost, land cost or governmental regulations and incentives, considering equal cost data across the locations can still be a reasonable assumption. This can be primarily justified by the fact that a substantial portion of the capital expenditure, encompassing equipment cost provided by global suppliers, is equal worldwide. In addition, a sensitivity analysis was carried out in this work (refer to Section 4.6.1), accounting for the potential variability in cost data across the locations.

The techno-economic analysis performed in this study is based on the LCOE, expressed in €/MWh. The LCOE is a key parameter in the economic feasibility assessment of power plants since it provides a standard criterion for evaluating long-term financial viability of the system by considering factors such as initial investment, operational expenditure, discount rate, power plant lifetime and net annual energy yield. The LCOE can be defined as [148,149]:

$$LCOE = \frac{CAPEX \times \left(\frac{d(1+d)^n}{(1+d)^n - 1}\right) + OPEX}{NAEY} \tag{4.12}$$

where CAPEX represents the capital expenditure of the plant, d is the discount rate, n is the useful lifespan of the plant, OPEX represents the annual cost of operation and maintenance and NAEY is the net annual energy yield in MWh. To compute the LCOE by Eq. (4.12), the NAEY was provided by the thermal model (Section 4.5.4) for various configuration, while the remaining parameters are given in Table 4.5.

Figure 4.22 displays the LCOE for various linear CSP technologies considering the reference locations. It is noteworthy that, although equal cost data was considered for different locations, the economic portion in the LCOE (Eq. (4.12)) varies in proportion to the net annual energy yield obtained for each location. This variation in the economic portion in the LCOE arises from the power block and TES system costs (refer to Table 4.5), both of which are primarily dependent on the available annual solar resource for each location. As shown in Figure 4.22, the evacuated PTC is more economical compared to the evacuated LFC since a higher optical efficiency (and consequently a higher net annual energy yield) for the PTC outweighs its higher capital cost compared to the LFC. This result is influenced by the fact that LFC technology is less mature than PTC, allowing room for further enhancement [150]. With regard to the non-evacuated tubes, the scenario is

different; the LFC technology demonstrates a slightly lower LCOE in contrast to the PTC technology, implying that a lower optical efficiency (and consequently a lower net annual energy yield) for the non-evacuated LFC is compensated by its lower capital cost compared to the non-evacuated PTC. This is due to the fact that the difference in the net annual energy yield between LFC and PTC technologies is less considerable for the non-evacuated cases compared to evacuated ones for each location (as discussed in Figure 4.21). Furthermore, Figure 4.22 suggests that, despite the additional cost of evacuation of receiver tube, an evacuated tube attains a lower LCOE compared to a non-evacuated tube. It can be concluded that the thermal performance improvement caused by the vacuum justifies the evacuation cost.

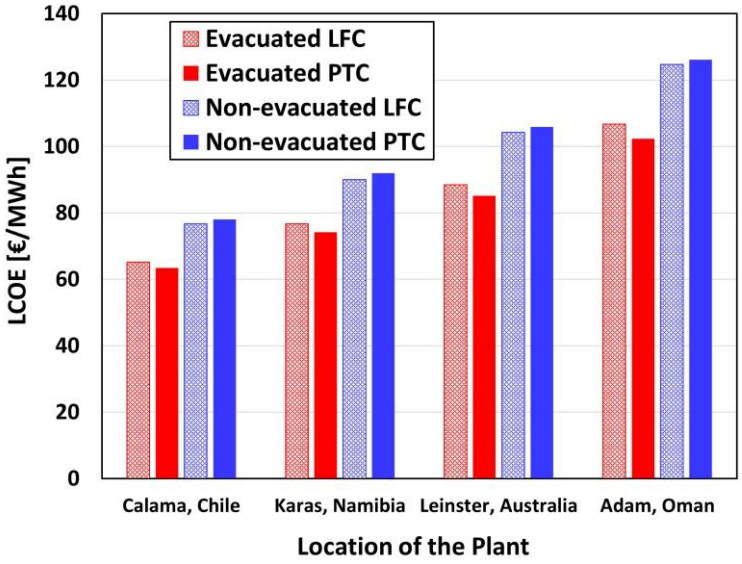

Figure 4.22: LCOE computed for the reference locations considering different configurations.

4.6.1 Sensitivity analysis

In this section, the impact of key parameters on the LCOE was investigated by conducting a sensitivity analysis based on optical efficiency (and corresponding net annual energy yield), solar field HTF, CAPEX, OPEX and discount rate. This analysis also takes into account potential variations in cost data across the locations. The reference location for this study is Namibia with a DNI of 2962 kWh/m2/year (refer to Figure 4.19b).

4.6.1.1 Optical efficiency

The annual optical efficiency for the PTC and the LFC were computed to be about 61% and 47%, resulting in the net annual energy yield of 2235 MWh and 1926 MWh, respectively. In fact, the difference in the optical efficiency is the main cause of a lower annual energy yield provided by the LFC in comparison with the PTC. In this respect, a sensitivity analysis was conducted by varying the LFC annual optical efficiency to evaluate the impact of this parameter on the LCOE. This study was carried out through an analytic approach to determine the minimum LFC annual optical efficiency that would lead to an equivalent LCOE to that of the PTC. As shown in Figure 4.23, the analysis revealed that an over 6% increase in the LFC annual optical efficiency would result in an increase of 245 MWh in the net annual energy yield. This variation would result in a reduction of over 3 €/MWh in the LCOE of the LFC, making it as economical as the PTC. However, such an enhancement in the optical efficiency must be attained without an increase in the capital cost of the plant.

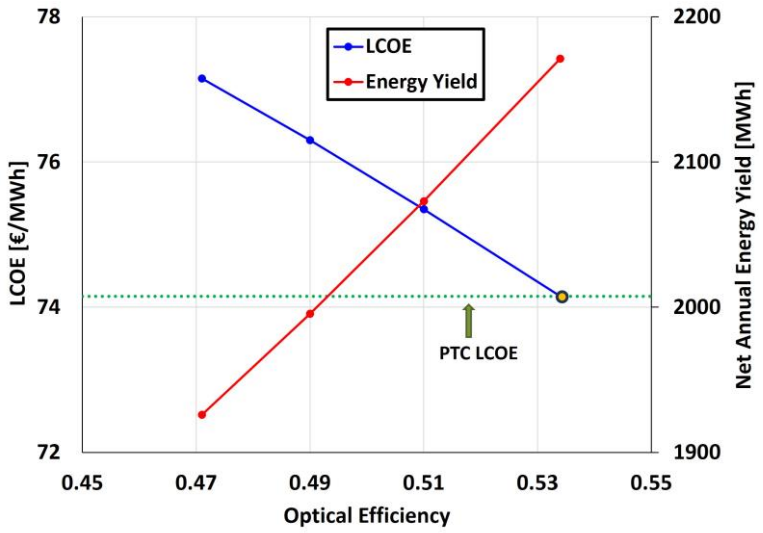

Figure 4.23: Sensitivity analysis representing the impact of the LFC optical efficiency on equalizing the LCOE for LFC and PTC technologies.

The improvement in the optical efficiency shown in Figure 4.23 could be achievable as it was demonstrated by Cheng et al. [151] that the LFC annual optical efficiency would increase by 13% through a specific optimization measure to reach over 60%. For this purpose, Cheng et al. [151] developed a novel optical optimization model by combining Monte Carlo ray-tracing method with particle swarm optimization algorithm. This approach could enhance the annual optical

efficiency through optimizing critical geometric parameters including the position and the size of the receiver tube, mirror width, spacing, and CPC geometry. These optimization measures resulted in minimizing optical losses caused by shadowing, blocking, and CPC interception. The study also suggested employing flat mirrors, which are simpler and cheaper to manufacture compared to parabolic or cylindrical mirrors. However, potential economic implications of such an optimization strategy were not investigated.

4.6.1.2 Heat transfer fluid

As mentioned in Section 4.2, molten salt (60%wt. $NaNO_3$ + 40%wt. KNO_3) was considered as the HTF for various CSP systems in this techno-economic analysis, operating within the temperature range of 290-500 °C. Nonetheless, linear CSP technologies can also operate at lower HTF temperatures. As already shown in Figure 4.14, although convective heat loss from the absorber tube is negligible for the evacuated tubes, it is a function of the HTF temperature for the non-evacuated tubes. Thus, it is expected to observe a remarkable decrease in convective heat loss from the non-evacuated tubes at lower temperatures. As a result, the difference in the LCOE between non-evacuated and evacuated tubes might become lower. This means that the positive effect of the evacuation (which results in negligible convective heat losses) on the LCOE may be less noticeable at lower temperatures.

In this regard, a sensitivity analysis was conducted based on the HTF operating temperature to evaluate its impact on the LCOE. For this purpose, employing two other HTFs were investigated: a medium-temperature HTF (thermal oil, Therminol VP-1) operating at the temperature range of 290-400 °C, and a low-temperature HTF (thermal oil, DelcoTerm Solar E15) operating at the temperature range of 180-300 °C. The power cycle efficiencies of 35% and 31% were assumed for the medium-temperature and low-temperature plants, respectively. These values are sourced from [52,139], which indicate that the power cycle efficiency in medium-temperature and low-temperature plants typically ranges from 28% to 38%, depending on the peak cycle temperature. In this respect, the power cycle efficiencies of 35% and 31% align with the peak temperatures of the medium-temperature plant (400 °C) and the low-temperature plant (300 °C).

Figure 4.24 depicts variations in the LCOE for the plants with low, medium and high HTF temperatures. As anticipated, employing a low-temperature HTF would increase the LCOE due to a reduction in the electricity production caused by

a lower power cycle efficiency. However, the difference in the LCOE between the non-evacuated LFC and the non-evacuated PTC is smaller at low HTF temperatures compared to high HTF temperatures. This implies that the benefit of the LFC is relatively greater at higher operating temperatures. In fact, the percentage increase in the net annual energy yield with the rise in the HTF temperature is slightly greater for the LFC in comparison with the PTC. This aligns with the trend of annual thermal efficiencies, where, as heat losses increase with the rise in the HTF temperature, the LFC experiences a relatively lower decrease in the thermal efficiency compared to the PTC. This can be attributed to the advantage of the secondary concentrator in the LFC technology. However, in the case of the evacuated tubes, the decrease in the LCOE at high HTF temperatures is more substantial compared to the non-evacuated ones. While the ratio of the LCOE for the evacuated PTC to that for the non-evacuated PTC stands at 86% at a low HTF temperature, it decreases to 80.7% at a high HTF temperature.

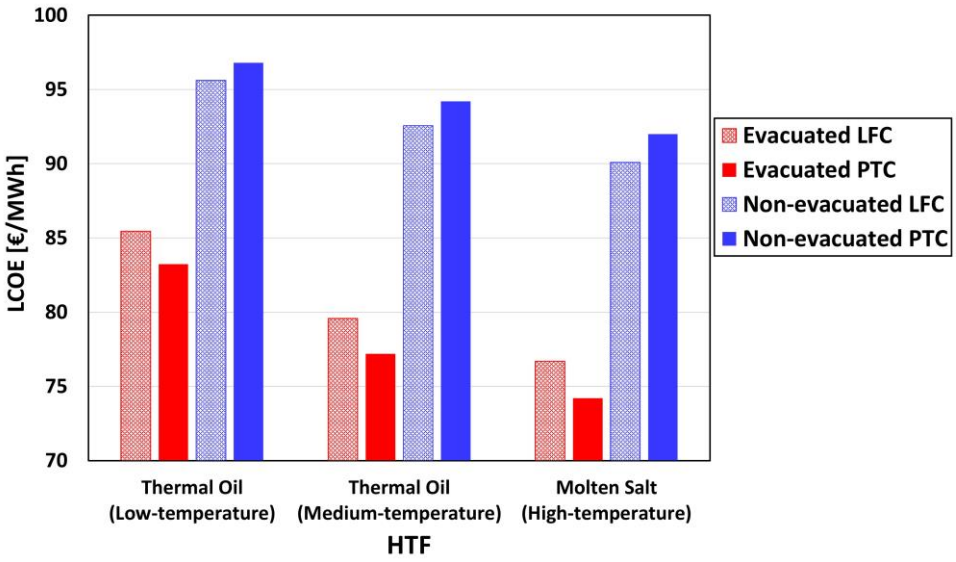

Figure 4.24: LCOE variations using HTFs at low, medium and high temperatures for different configurations.

4.6.1.3 Economic parameters

Since the input cost data (financial parameters given in Table 4.5) may vary depending on the economic conditions of any CSP projects, a sensitivity analysis is necessary to take into account the variability of these parameters. In this analysis, CAPEX, OPEX and discount rate were investigated as the most crucial economic

parameters in the LCOE, as presented in Eq. (4.12), considering a variation of 20% [152] for each parameter.

Figure 4.25 shows the impact of the key economic parameters on the LCOE for different CSP systems. As can be observed, Figure 4.25a evaluates the impact of the capital cost on equalizing the LCOE for the evacuated LFC and PTC. According to Figure 4.25a, a reduction of over 4% in the capital cost of the reference evacuated LFC would equalize the LCOE for the evacuated LFC and PTC, assuming that this reduction in the LFC capital cost can be achieved at equal performance of the plant. Furthermore, it should be noted that since the input economic data in this study comprising the capital costs given in Table 4.5, collected from literature, may be variable due to any unpredictable conditions, Figure 4.25a takes into account the variability of these input parameters for different linear CSP technologies.

The influence of the operational expenditure on the LCOE is illustrated in Figure 4.25b. As shown, the operational cost represents a minimal impact on the LCOE; the decrease/increase of the OPEX by 20% leads to the slight decrease/increase of the LCOE by 3% on average for the different configurations.

As given in Table 4.5, the discount rate was considered to be 0.1 in this work, according to [149]. Figure 4.25c shows the impact of the discount rate on the LCOE for different systems. It can be observed that the decrease/increase of the discount rate by 20% results in the considerable decrease/increase of the LCOE by nearly 14% on average for different configurations. However, this variation is still relatively less noticeable compared to the CAPEX that influences the LCOE by the decrease/increase of nearly 17% (Figure 4.25a).

4.7 Concluding remarks

In this chapter, a comparative techno-economic assessment of various linear CSP systems was represented, encompassing PTC and LFC with evacuated and non-evacuated receiver technologies. In this respect, a 1D receiver model was developed along the collector axis to compute the net annual energy yield, incorporating hourly meteorological data for a year. This model was supported by an optical ray-tracing model to calculate incident power on the receiver tube and by a lumped-parameter model to compute heat losses for different HTF temperatures. While the former computes the incident angle modifier (IAM) and the reference optical efficiency for a given PTC or LFC plant, the latter requires appropriate correlations to determine the convective share of heat losses.

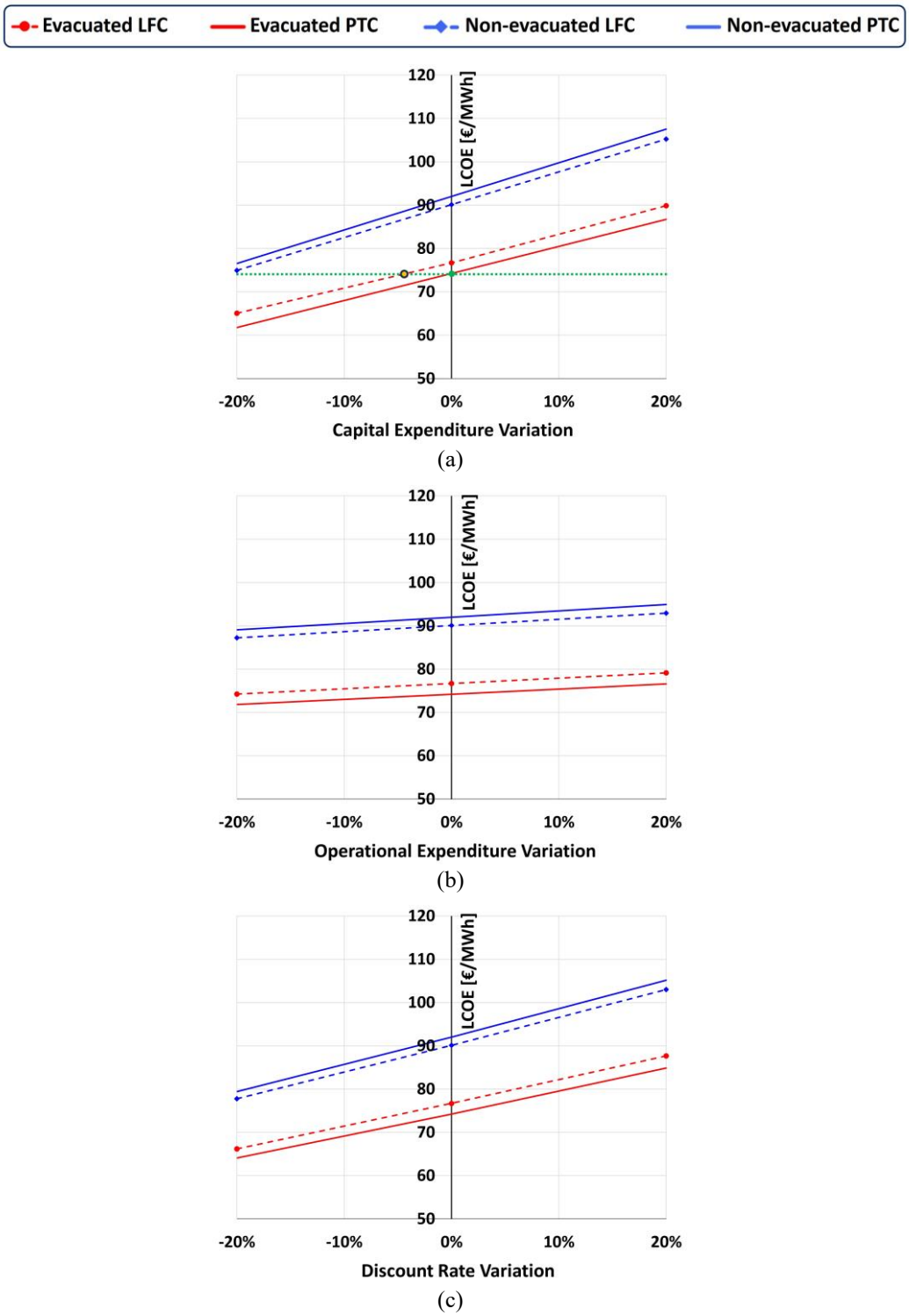

Figure 4.25: Sensitivity analysis representing the impact of the economic parameters on the LCOE for various linear CSP technologies.

For the LFC receiver unit, the existence of a secondary concentrator does not allow employing common correlations applicable to cylinders in cross flow. Therefore, a 2D steady-state CFD model was developed to generate suitable correlations for the convective heat transfer between the glass cover and the environment in the LFC case. According to the results obtained by the CFD model, the LFC receiver tube experiences significantly lower convective heat loss compared to the PTC, attributed to the semi-cavity effect of the CPC unit which protects the receiver against wind. Furthermore, under conditions of no wind (natural convection), the CPC unit effectively minimizes convective heat losses by capturing the heated air moving upward, thereby constraining the replacement of the hot air with a fresh cold air.

Thermal performance analysis, exploiting the 1D receiver model, investigated four reference locations with varying annual DNI values from 2183 kWh/m^2 to 3409 kWh/m^2. The results proved that the PTC yields higher net annual energy than the LFC because of a more effective optical performance of the parabolic collector. However, the difference in the net annual energy yield between the PTC and the LFC is less considerable with non-evacuated tubes, attributed to lower heat losses from the LFC receiver tube. As expected, evacuated tubes could yield higher net annual energy compared to non-evacuated ones due to lower heat losses ensured by the evacuation.

Exploiting the net annual energy yield computed by the thermal model for each location, an economic analysis was carried out based on the LCOE considering cost data collected from literature. It was concluded that a PTC system with an evacuated tube is the most economical linear CSP technology, with the lowest LCOE of 63.4 €/MWh for the highest DNI location (Chile). This is attributed to a higher optical efficiency, which outweighs a higher capital cost of an evacuated PTC. Conversely, in the case of non-evacuated receiver tubes, LFC systems exhibited slightly lower LCOE compared to PTC systems for each location, representing the dominance of a lower capital cost over a lower net annual energy yield. In addition, evacuated tubes indicated a lower LCOE compared to non-evacuated tubes, justifying the cost of evacuation through an enhanced thermal performance. The comparison of locations considering each individual configuration reveals the lowest and highest LCOE in Chile and Oman, respectively, aligning with the trend in the net annual energy yield.

Finally, a sensitivity analysis was conducted considering the key parameters affecting the LCOE, comprising optical efficiency, solar field HTF, CAPEX, OPEX

and discount rate. It was proven that an increase of approximately 6% in the annual optical efficiency of an evacuated LFC could lead to a rise of 245 MWh in the net annual energy yield and a reduction of over 3 €/MWh in the LCOE. This enhancement in the LFC performance would potentially make it as economical as the PTC system, assuming that it could be achieved without a further increase in the capital cost. Furthermore, an investigation into the variability of the capital cost revealed that a nearly 4% reduction in the capital cost of an evacuated LFC would result in the same LCOE as an evacuated PTC. It is important to note that while some uncertainties were addressed in this work through the inclusion of contingency, EPC and owner cost, challenges related to governmental regulations and incentives may vary across different countries.

Chapter 5

Enhancement of a Thermocline Energy Storage System: Geometrical and Phase Change Material (PCM) Strategies

5.1 Overview

In this chapter, a single-medium indirect molten salt thermocline TES system developed by ENEA [104,105] is considered as the case study for improvement purposes (Section 5.2). This case study was improved by performing two enhancement measures in terms of geometrical modification and PCM integration. Geometrical modification aimed at involving the entire tank volume in the thermal stratification inside the tank as well as minimizing undesirable heat transfers within the tank body during the charge and discharge processes (Section 5.3). Moreover, PCM integration could further increase the potential storage capacity of the TES system, while expected to help temperature stabilization inside the tank. This was carried out by inserting sets of PCM toroidal tubes at different positions within the tank (Section 5.4). A validated CFD model was developed to investigate the thermal performance of the TES systems (Section 5.5). This model was linked with a PCM lumped-parameter model (Section 5.6), which has been validated against experimental data (Section 5.7). Finally, a comparative performance analysis is

presented to determine the most effective configuration for the TES system under investigation (Section 5.8). The content of this chapter is mostly based on the work published in [153].

5.2 Thermocline energy storage system: case study

Figure 5.1 shows the configuration of the experimental setup and the 2D sketch of a single-medium indirect thermocline TES system. This system includes a cylindrical storage tank, two helically coiled heat exchangers (HXs) and an internal vertical channel. The two HXs are placed at the channel ends for charging (bottom serpentine) and for discharging (top serpentine). The internal channel has been designed to facilitate the buoyancy-driven motion of molten salt, preventing disturbances in the thermal stratification inside the tank. To minimize heat losses to the environment, the outer walls of the tank are appropriately insulated. The tank is filled to 93% of its height with a molten salt mixture (HITEC XL), while the region above the salt is occupied by atmospheric pressure air. ENEA developed and tested the experimental prototype at the Casaccia research center [104], designed for CSP plants with mineral oil at medium-low temperatures (205-300 °C) connected to an organic Rankine power cycle (ORC) with the operating temperatures ranging from 175 to 270 °C. The prototype also included electrical heaters installed at the bottom region to provide heat for the charging test. In addition, a heat tracing system can be incorporated into the tank to avoid salt freezing or cold spots within the tank, especially within the heat exchangers.

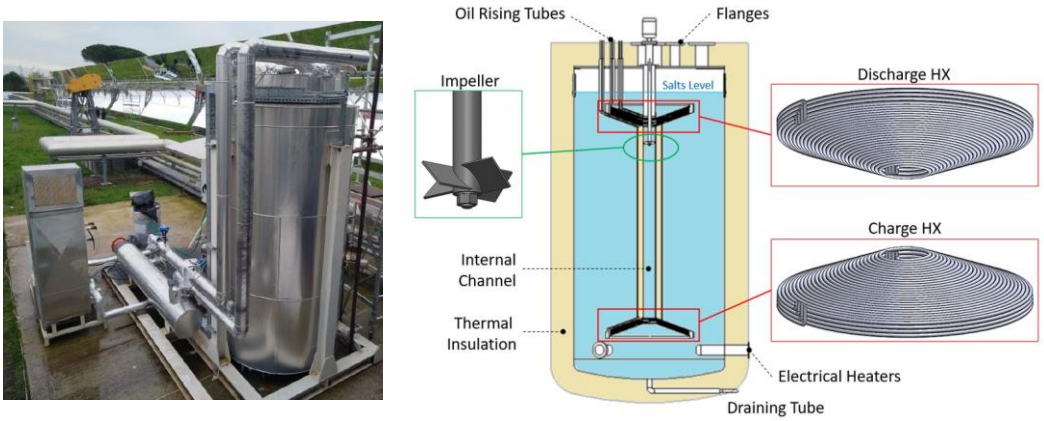

(a) (b)

Figure 5.1: Thermocline TES system considered as a case study, developed by ENEA: (a) experimental setup and (b) sketch.

Considering the thermocline TES system depicted in Figure 5.1 as the reference case, two improvement approaches were conducted in this study. In this respect, Section 5.3 represents a geometrically modified configuration of the TES system, addressing potential disadvantages of the tank geometry. Then, Section 5.4 outlines PCM integration strategy aimed at further enhancing the storage capacity of the TES system.

5.3 Geometrical improvement

The thermal performance of the case study shown in Figure 5.1 indicated several drawbacks, as outlined below [105]:

- During the charge process, the heated salt was confined beneath the charge HX.
- The molten salt at the tank bottom could not participate in the natural convection-driven motion.
- Lack of insulation for the HX shells could lead to undesirable heat losses from serpentines.

To mitigate these issues, an improvement approach was employed. Figure 5.2 illustrates the experimental configuration as the reference case (Case 1) and the optimized system (Case 2). As shown in Figure 5.2b, the following modifications were implemented:

- Thermal insulation was provided for the conical regions in the lower section of the charge HX shell and in the upper section of the discharge HX shell. The insulation would prevent disadvantageous heat transfers during the charge and discharge processes and avoid salt entrapment in these sections.
- The internal channel length was extended by moving the charge HX shell closer to the tank bottom, specifically by the end of the vertical wall. This adjustment could facilitate the involvement of salt at the tank bottom in natural circulation within the tank.
- Thermal insulation was applied to the upper region of the charge HX shell and to the lower region of the discharge HX shell to prevent undesirable heat transfer from the HX shells to the tank body during the charge and discharge processes.

In the subsequent step, PCM can be integrated into the system to further enhance the thermal performance of the TES system, which is investigated in detail in Section 5.4.

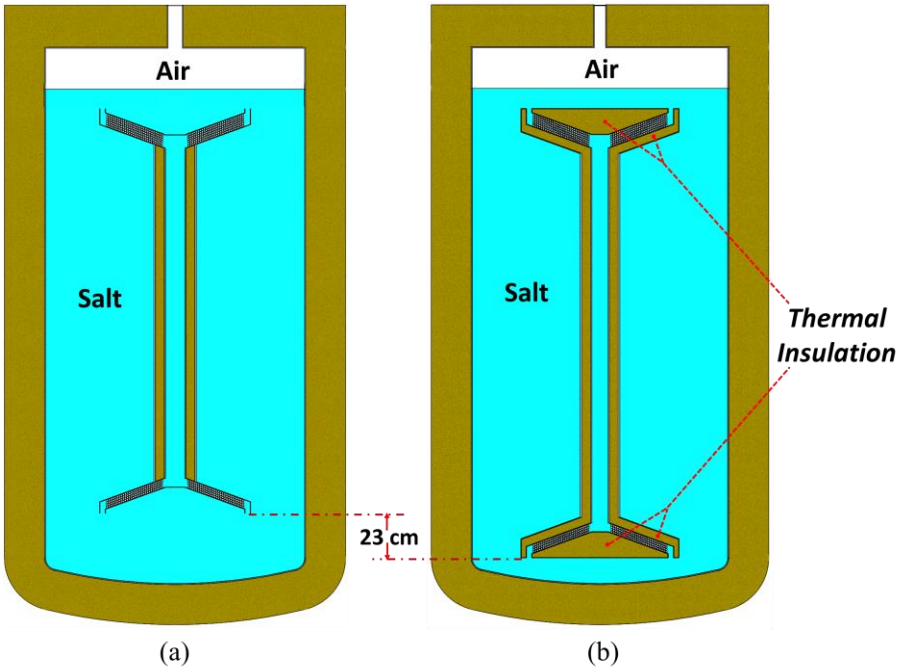

Figure 5.2: Schematic of the thermocline TES systems: (a) reference case (Case 1), and (b) the configuration with a modified geometry (Case 2).

It should be noted that the experiments proved that the impeller shown in Figure 5.1b would not affect the thermal performance of the TES system during the charge and discharge processes [104]. Therefore, it is not operated in Case 1 (the reference case) in this study and has been removed from the system in the modified geometry.

5.4 PCM integration

After modification of the tank geometry, layers of PCM tubes were introduced to the system to reach two main objectives: improving thermal storage capacity through the PCM latent heat, and stabilization of molten salt temperature at HXs locations. The latter is achieved as the PCM phase change occurs at a nearly constant temperature, providing more efficient thermal stratification within the tank and making a sharper temperature gradient within the thermocline region.

In this respect, sets of PCM tubes were strategically inserted at various heights in the tank. Specifically, PCM tubes were placed close to the top (discharge) HX (Figure 5.3a, Case 3a), near the bottom (charge) HX (Figure 5.3b, Case 3b), and at both top and bottom locations (Figure 5.3c, Case 3c). This approach, involving three different scenarios, allows for an examination of the effect of each PCM tube

insertion on the overall performance of the thermocline TES system and on the thermal stratification within the tank. Table 5.1 provides a summary of different configurations considered in this study.

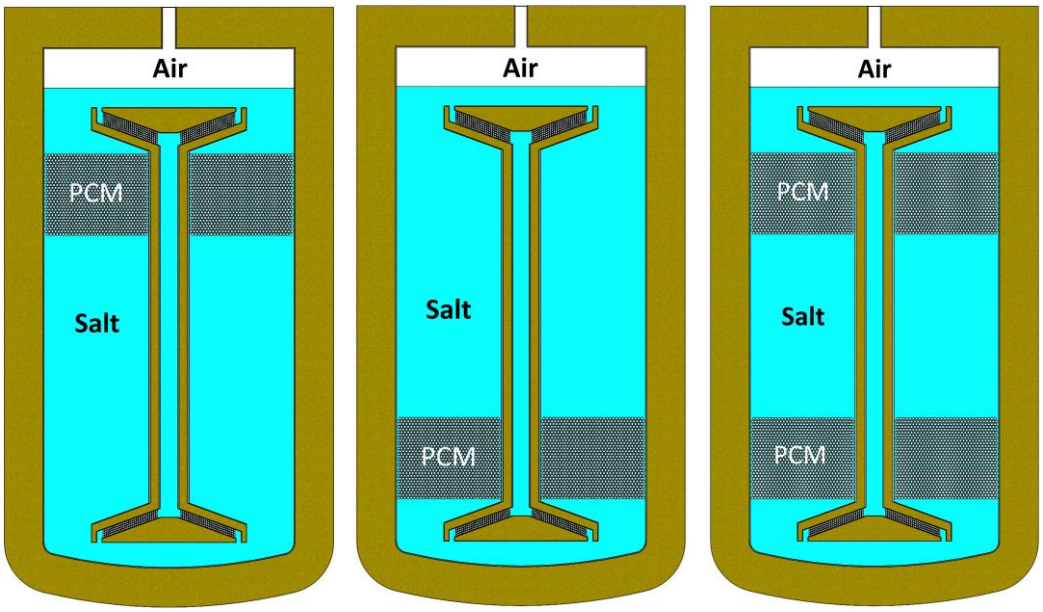

(a) (b) (c)

Figure 5.3: Thermocline TES systems integrated with PCM inserts at: (a) the top side (Case 3a), (b) the bottom side (Case 3b), and (c) both top and bottom sides (Case 3c).

Table 5.1: Various thermocline TES systems considered in this study

Case No.	Description
1	Reference case
2	Geometrically modified configuration
3a	Geometrically modified + PCM at top location
3b	Geometrically modified + PCM at bottom location
3c	Geometrically modified + PCM at both top/bottom locations

For the configurations depicted in Figure 5.3, the selection of appropriate PCM mediums is a critical step. This choice depends on the tank height and corresponding expected salt temperatures, which, in turn, needs PCMs with suitable

melting temperatures for each specific location. Furthermore, this approach involves determining the most effective option for introducing PCMs through finding a trade-off between maximizing PCM volume and maintaining an optimal heat transfer surface area. In this regard, the criteria considered for the PCM selection and their corresponding properties are detailed in Section 5.4.1. Additionally, Section 5.4.2 represents the procedure of the geometrical enhancement performed for the PCM tube banks introduced into the system.

5.4.1 PCM selection

As shown in Figure 5.3, two PCM tube banks are positioned at the top and bottom of the tank. Hence, two distinct PCMs must be selected to align with the expected salt temperature at each respective location. While the PCM melting temperature is a critical parameter for this selection, other factors such as chemical and thermal stability, cost and availability should also be taken into account.

Since maximum salt temperature at the top of the tank is expected to be 285 ℃, an appropriate choice for the PCM positioned at this location could be sodium nitrite ($NaNO_2$) with a melting temperature of 270 °C. Sodium nitrite exhibits stability up to 330 ℃ [154], well above the maximum reachable salt temperature in the thermocline TES system in this study. Moreover, sodium nitrite is commercially available in large quantities at affordable prices [155]. The thermophysical properties of sodium nitrite are provided in Table 5.2.

Table 5.2: Thermophysical properties of the PCMs

Properties	PCM-1	PCM-2
Composition, wt.%	$NaNO_2$ (100)	$LiNO_3$-$NaNO_3$ (57:43)
Phase change temperature, ℃	270	193
Latent heat, kJ/kg	178	248
Specific heat, kJ/kg.K (solid/liquid)	1.6/1.77	1.53/1.75
Density, kg/m^3 (solid/liquid)	2170/1810	1880/1880
Thermal conductivity, W/m.K (solid/liquid)	0.67/0.53	0.54/0.54
Dynamic viscosity, Pa.s	3.0e-3	4.5e-3

Conversely, PCM located at the lower zone interacts with the coldest layers in the tank, necessitating a melting temperature compatible with the salt temperature at this region (190 °C). For this purpose, the mixture of $LiNO_3$-$NaNO_3$ (57:43 wt.%) with a melting temperature of 193 °C was chosen to align with the salt temperature at bottom. As reported in [156], this mixture demonstrates stability at very high temperatures, up to 600 °C. Additionally, $NaNO_3$, a component of this mixture, is available in large quantities at economical prices [155]. Although $LiNO_3$ might not be the most cost-effective option, recent advancements in production technology have significantly lowered costs, as indicated in [157]. According to [158], the production of $LiNO_3$ from lithium carbonate with nitric acid would further reduce its cost. Table 5.2 summarizes the thermophysical properties of this mixture. It should be noted that, due to a lack of data in the literature for the thermal conductivity of $LiNO_3$-$NaNO_3$ (57:43 wt.%), that of $LiNO_3$-$NaNO_3$ (49:51 wt.%) has been utilized in this study.

5.4.2 Geometrical optimization of the PCM tube banks

After the selection of the PCMs, the subsequent step is to define an optimal geometrical strategy for the PCM inserts. As illustrated in Figure 5.3, the TES system involves a bank of PCM toroidal tubes positioned at each region (top/bottom) of the tank. This setup not only keeps the axisymmetric layout of the tank, but can also allow us to locate PCMs at the desired height inside the tank. Furthermore, the vertical motion of salt across the tubes simulates a cross-flow HX, potentially leading to more effective heat transfer.

The vertical locations of the tube banks were determined according to the thermal stratifications observed within the tank during the charge/discharge processes in Case 2 (refer to Section 5.8.1). In particular, areas with minimal differences in salt temperature were identified at each top and bottom zone, considering the respective PCM melting temperature. The resulting height of the tube banks would be approximately 420 mm for each zone, with the width constrained by a portion of the tank radius between the internal vertical channel and the tank inner wall, approximately 540 mm. The toroidal tubes were arranged in rows using a staggered array configuration, forming equilateral triangles, as depicted in Figure 5.4. This configuration could demonstrate more efficient thermal performance in comparison with an inline configuration, particularly in cases of low Reynolds numbers ($Re \approx 200$) [159,160].

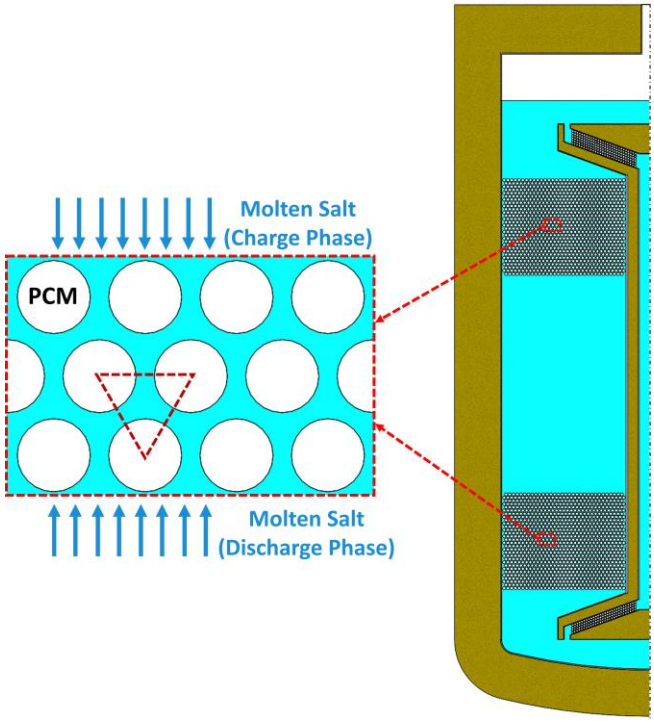

Figure 5.4: Staggered PCM tubes with equilateral triangles pattern, integrated into the thermocline TES system.

The tube wall thickness, constructed from stainless steel (AISI 316), was assumed to be 1 mm. The spacing between tubes was determined according to a pitch-to-diameter ratio, specifically chosen as 1.25 to optimize the heat transfer rate, as recommended in [159].

For the external diameter of the tubes, a parametric study is necessary to find a balance between the PCM volume and the heat transfer surface area. This optimization strategy will also influence the number of tubes accommodated within a predefined region. Figure 5.5a and Figure 5.5b show heat transfer surface density and PCM volume density, respectively, for various external tube diameters. The former is defined as the ratio of heat transfer surface area to tube length, while the latter is defined as the ratio of PCM volume to tube length. As can be seen, increasing the tube diameter results in a decrease in the heat transfer surface area (Figure 5.5a), while the PCM volume shows an upward trend with increasing the tube diameter (Figure 5.5b). Nevertheless, minor fluctuations are observed in the PCM volume trend due to a reduction in the number of tubes that can be accommodated in a predefined region with an increase in the tube diameter. To determine an optimal diameter, a balancing strategy was implemented, considering

the average values as minimum requirements (approximately 40 m²/m and 0.092 m³/m for heat transfer surface density and PCM volume density, respectively). In this respect, an external diameter of 13 mm was selected, ensuring a heat transfer surface density of approximately 40 m²/m and a PCM volume density of about 0.093 m³/m (refer to Figure 5.5).

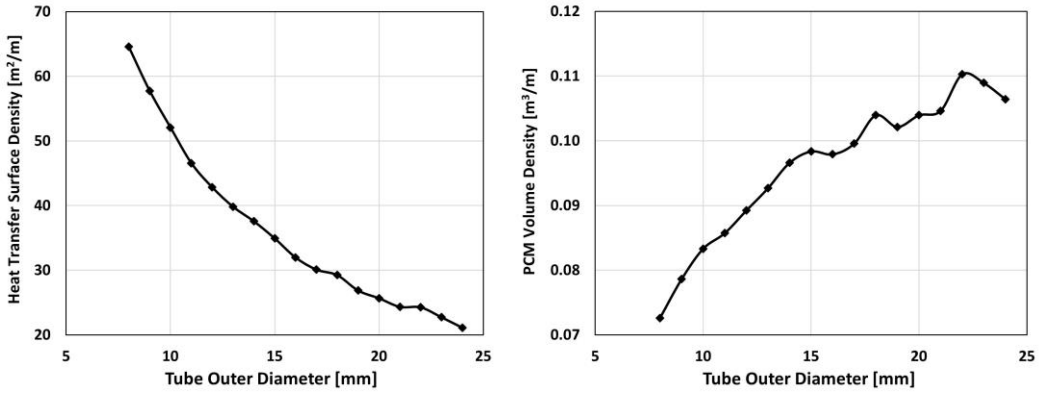

(a) (b)

Figure 5.5: Parametric optimization for obtaining the optimal tube external diameter: (a) heat transfer surface density and (b) PCM volume density.

Consequently, 975 tubes were located in total in each designated region (top/bottom). Each PCM tube bank individually accounts for approximately 7.7% of the tank volume, resulting in a removal volume of the salt at 10.8% because of the existence of the tube walls. Regarding the PCM integration at both top and bottom locations, the contribution of PCMs would be about 15.4% of the tank volume. This signifies about 14% enhancement in the thermal storage capacity of the thermocline TES system. The key geometric parameters of the PCM tube banks, as determined through the parametric optimization, are listed in Table 5.3.

5.5 CFD model

A transient two-dimensional CFD model was developed by using a commercial software Star-CCM+ [140]. The main objective of this model is to investigate heat losses and salt temperature distributions within the tank throughout the charge and discharge processes. The thermophysical properties of the materials incorporated into the CFD model are specified in [105].

Table 5.3: Geometric parameters of the PCM tube banks for each (top/bottom) location

Parameters	Value
Number of tubes in total	975
Number of rows	30
Number of tubes in each row (odd/even)	33/32
Height of the tube bank, mm	420
Width of the tube bank, mm	540
Pitch to diameter ratio	1.25
External tube diameter, mm	13
Thickness of the tube wall, mm	1

5.5.1 Computational domain, initial and boundary conditions

The CFD model developed for the thermocline TES system in this thesis is based on that represented and validated against experimental data for the charge and discharge processes in [105]. However, several modifications have been introduced to the computational domain, initial and boundary conditions, which are elaborated in this section.

Figure 5.6 illustrates the 2D axisymmetric computational domain of the CFD model, encompassing molten salt, the air above the salt, thermal insulations, and the stainless-steel (AISI 316) walls of the PCM tubes and of the charge/discharge HXs. Furthermore, Figure 5.6 highlights various heights within the tank where salt temperatures need to be monitored to facilitate the comparison among different configurations. The motivations behind selecting these specific heights are expressed in Section 5.8. As shown in Figure 5.6, the computational domain excludes the oil in the charge and discharge HXs; instead, a Robin boundary condition was introduced considering the heat transfer coefficient and the oil temperature. The latter was determined through a linear variation along the axial direction, taking into account the mean temperature for each loop [160]. The heat transfer coefficient incorporates a convection between the oil and the tube wall, and

a radial conduction within the tube wall. The former was computed using a proper correlation for conical coil HXs, as outlined in Eq. (5.1). This correlation has been developed for conical coil HXs with an aperture angle of 135° [161], which closely aligns with the configuration of the HXs in the present system (approximately 140°).

$$Nu = 0.136\, De^{0.8}.Pr^{-0.19} \tag{5.1}$$

where Nu, De and Pr are the Nusselt, Dean and Prandtl numbers, respectively.

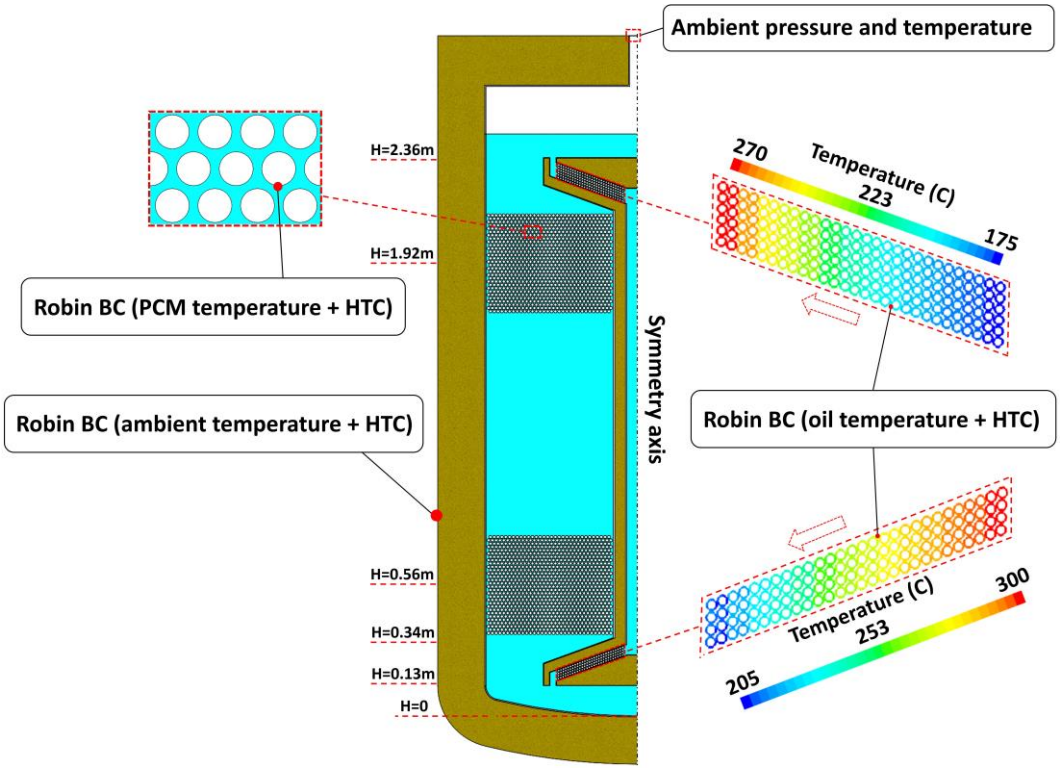

Figure 5.6: Computational domain and boundary conditions considered in the CFD model.

As depicted in Figure 5.6, the PCMs and the tube walls are not included in the computational domain, while a Robin boundary condition was implemented instead. In this regard, the heat transfer coefficient and the PCM temperature were determined through a lumped-parameter model developed for each PCM tube, integrated with the CFD model (refer to Section 5.6).

The CFD model incorporated the SST k-ω turbulence model, accounting for the gravity effect within the computational domain. Based on the original design specifications, an initial uniform temperature of 190 °C was assumed for the whole TES system in the first cycle of the charge process. This assumption is based on the premise that the TES system has already been fully discharged, reaching the minimum design temperature within the entire storage tank. In addition, mass flow rate of the mineral oil in the charge and discharge HXs was assumed to be 1 kg/s, while the inlet temperatures were 300 °C and 175 °C in the charge and discharge HXs, respectively.

5.5.2 Space and time discretization

The discretization of the computational domain led to the creation of a mesh composed of polygonal cells. A mesh sensitivity study was conducted for Case 3a with the number of cells varying from 8×10^4 to 3.2×10^5. This analysis was carried out with a heat load of 20 kW applied to the charge HX, while the transient stopped at t=100 min. Figure 5.7 displays the results of this mesh independence study in terms of the salt temperature at the tank top (h=2.36 m). According to Figure 5.7, it was determined that a minimum of 2.26×10^5 cells is required to attain grid size independent results. The chosen mesh demonstrated a deviation of less than 1% in comparison with the most refined mesh investigated in this analysis. Considering the same mesh settings for the cases without PCM, with one PCM tube bank at bottom, and with two PCM tube banks at top/bottom locations, the minimum numbers of cells would be 1.2×10^5, 2.26×10^5, and 3.34×10^5, respectively. Figure 5.8 shows the computational mesh generated for the CFD model, with a specific focus on the regions near PCM tubes.

Moreover, a sensitivity analysis was conducted concerning time discretization to achieve an optimal compromise between computational time and result accuracy. In this context, a range of time steps from 0.2s to 3s was investigated, and it was concluded that a time step of 0.5 seconds with 50 internal iterations would provide an optimal balance between computational time and result accuracy. This selection results in a deviation of less than 1% in comparison with the smallest time step investigated in this study, particularly in terms of the salt temperature at the topmost layer of the tank.

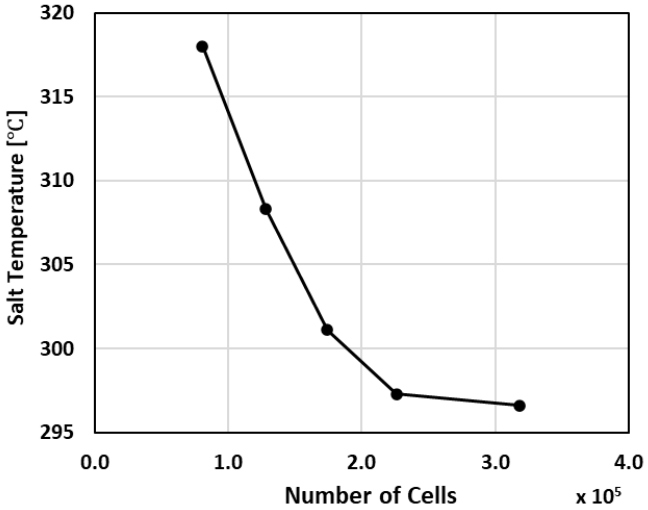

Figure 5.7: Mesh independence study investigating variations of the salt temperature at h=2.36 m with the number of cells.

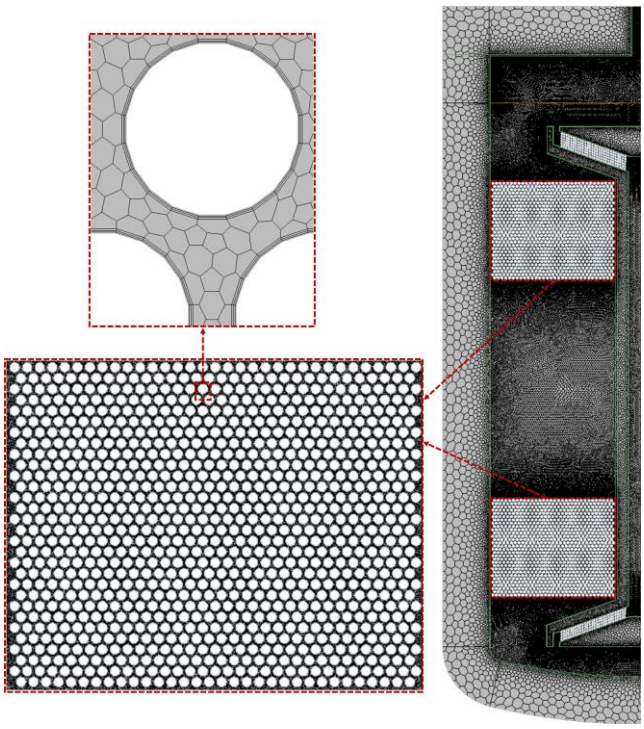

Figure 5.8: Computational mesh highlighting the regions near PCM tubes

5.6 PCM lumped-parameter model

As detailed in Section 5.5.1, a Robin boundary condition was implemented for PCM tubes, incorporating PCM temperature and heat transfer coefficient. These two parameters were determined by a lumped-parameter model, integrated with the CFD model. Figure 5.9 illustrates a schematic of heat transfer phenomena within a PCM tube, as considered in the PCM lumped-parameter model. This approach reduces computational costs by employing a validated (refer to Section 5.7) simplified model, as opposed to involving more complex differential equations. The following assumptions were considered in this model:

- The control volume is in the thermodynamic equilibrium at each moment.
- During the charge and discharge phases, PCM tubes are fully filled, and variations in PCM volume are neglected [162].
- Throughout the charge and discharge phases, PCM temperature is spatially uniform inside each tube [162].

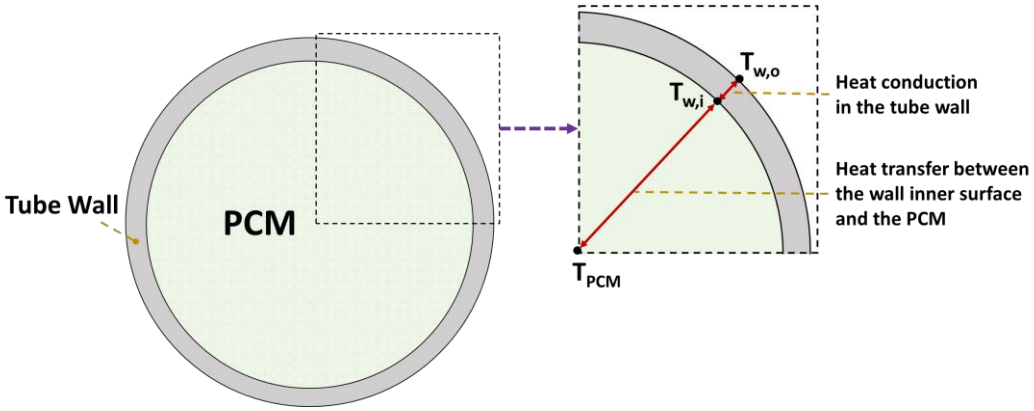

Figure 5.9: Schematic of heat transfer phenomena within a PCM tube as modelled in the lumped-parameter approach.

As outlined in Figure 5.9, the heat transfer coefficient considered in the Robin boundary condition encompasses a radial conduction within the tube wall and a heat transfer occurred between the PCM and the inner surface of the wall. The latter can occur through either conduction in the solid state (refer to Eq. (5.2)) or convection in the liquid state (refer to Eq. (5.3)). Additionally, heat transfer during the phase transition (melting or solidification) can be simulated by calculating the Nusselt number and, consequently, determining the convective heat transfer coefficient (refer to Eq. (5.4)).

$$q_s = k_s \times 2\pi x\left(T_{w,i} - T_{PCM,s}\right) \tag{5.2}$$

$$q_l = h_l \times \pi D_i x\left(T_{w,i} - T_{PCM,l}\right) \tag{5.3}$$

$$q_{pc} = h_{pc} \times \pi D_i x\left(T_{w,i} - T_m\right) \tag{5.4}$$

where q_s, q_l and q_{pc} represent the radial conduction within the tube wall in the solid state, liquid state and phase transition, respectively. $T_{PCM,s}$ and $T_{PCM,l}$ and T_m denote the PCM temperature in the solid state, liquid state and phase transition, respectively. $T_{w,i}$ is the temperature of the tube's inner wall, x and D_i are the length and the inner diameter of the tube, respectively. k_s represents the PCM thermal conductivity in the solid state, h_l and h_{pc} denote the convective heat transfer coefficient in the liquid state and phase transition, respectively.

In Eq. (5.3), the term h_l must be obtained by the Nusselt number, as provided by Eq. (5.5), applicable for horizontal tubes exposed to natural convection [163].

$$Nu_l = 0.35(Pr.Gr)^{0.25} \tag{5.5}$$

where Pr and Gr are the Prandtl and Grashof numbers, respectively.

In Eq. (5.4), the term h_{pc} should be calculated exclusively for each charge and discharge phase transition using the corresponding Nusselt number. Regarding the charge process, it can be defined as [164]:

$$Nu_{pc,ch} = \frac{C}{\Psi} \tag{5.6}$$

where C represents a function of controlling parameters, namely the dimensionless parameters that dominate the heat transfer phenomenon during melting. The determination of C is contingent upon the molten fraction, as detailed in [164]. Ψ is expressed as:

$$\Psi = \frac{St^{0.66}}{Gr^{0.29}Pr^{0.4}\chi^{0.72}\zeta^{0.02}} \tag{5.7}$$

where St denotes the Stefan number. χ and ζ are the parameters taking into account the effect of shell material thermal properties and sub-cooling of the system, respectively, which can be defined as:

$$\chi = 1 - k_{PCM}/k_w \tag{5.8}$$

$$\zeta = 1 - T_{\mathrm{i}}/T_m \tag{5.9}$$

where k_{PCM} and k_w are the thermal conductivity of the PCM and of the tube wall, respectively, and T_{i} represents the initial temperature of the system.

Regarding the discharge process, $h_{pc,disch}$ can be obtained through the respective Nusselt number, which is defined as [165]:

$$Nu_{pc,disch} = 3.23 \exp[-14.43(FoSte)] \tag{5.10}$$

where Fo represents the Fourier number.

It is worth mentioning that Eq. (5.10) is applicable when $FoSte \geq 0.015$. For the case of $FoSte < 0.015$, a linear correlation was applied, utilizing data derived from [165].

For each state of the PCM (solid, liquid or phase change), the radial conduction, occurring through the tube wall, can be computed by:

$$q_s\,, q_l\,, q_{pc} = k_w \frac{2\pi x}{ln(D_o/D_i)} \left(T_{w,o} - T_{w,i}\right) \tag{5.11}$$

where D_o represents the outer diameter of the tube and $T_{w,o}$ is the temperature of the tube's outer wall, which is obtained from the CFD model.

In addition, the dynamic energy equations for solid and liquid states are expressed as:

$$q_s = M c_{p,s} \frac{dT_{PCM,s}}{dt} \tag{5.12}$$

$$q_l = Mc_{p,l}\frac{dT_{PCM,l}}{dt} \tag{5.13}$$

where M is the PCM mass, t represents time, $c_{p,s}$ and $c_{p,l}$ denote the PCM specific heat in solid and liquid states, respectively.

In the solid state, Eq. (5.2), (5.11) and (5.12) yield the three unknowns $T_{PCM,s}$, q_s and $T_{w,i}$. Regarding the liquid state, the three unknowns $T_{PCM,l}$, q_l and $T_{w,i}$ can be determined by Eq. (5.3), (5.11) and (5.13). During the phase change, as the PCM temperature remains constant, only the two parameters q_{pc} and $T_{w,i}$ are unknown, which can be determined by Eq. (5.4) and (5.11).

Moreover, the molten fraction must be progressively calculated during the phase transition. Concerning the charge process, the molten fraction can be calculated by [164]:

$$\mathrm{MF}_{ch} = 1 - \left[1 - \frac{FoSt^{0.33}Gr^{0.27}Pr^{0.37}\chi^{0.72}\zeta^{-0.02}}{9.5}\right]^{1.8} \tag{5.14}$$

Regarding the discharge process, the molten fraction can be obtained by [166]:

$$\mathrm{MF}_{disch} = \left[1 - (3.8FoSt)^{1/2}\right]^2 \tag{5.15}$$

5.7 Model validation

In this section, validation of the present model against experimental data is presented. In this regard, first, validation of the CFD model of the TES thermocline tank is introduced using the experimental tests performed for the charge and discharge phases. Then, the PCM lumped-parameter model is validated against the experimental data for a spherical container in terms of PCM temperature during the melting and solidification processes.

5.7.1 CFD model of the thermocline tank

As mentioned in section 5.5, the CFD model of the thermocline TES system developed in the present work is based on that developed by [105], which has already been validated against the experimental data collected from the charge and

discharge tests. Figure 5.10 compares the results obtained by the CFD model with those observed during the charging and discharging experiments in terms of salt temperature stratification within the tank, reported in [105]. As shown, there is a good agreement between the experimental and numerical results, with $R^2 \approx 0.94$ for the charge test and $R^2 \approx 0.93$ for the discharge test. A good agreement could also be observed between the results of the experiment and those of the CFD model in terms of salt temperature at the channel ends for both charge and discharge tests. After validation of the CFD model, the study employed it to explore heat losses and salt temperature distribution within the tank during the charge and discharge processes. Based on these investigations, several geometrical issues were reported in the tank that could be mitigated by adopting appropriate enhancement measures. The present work focuses on these issues to address ineffective geometric characteristics of the TES system and to enhance its thermal performance by implementing specific improvement strategies.

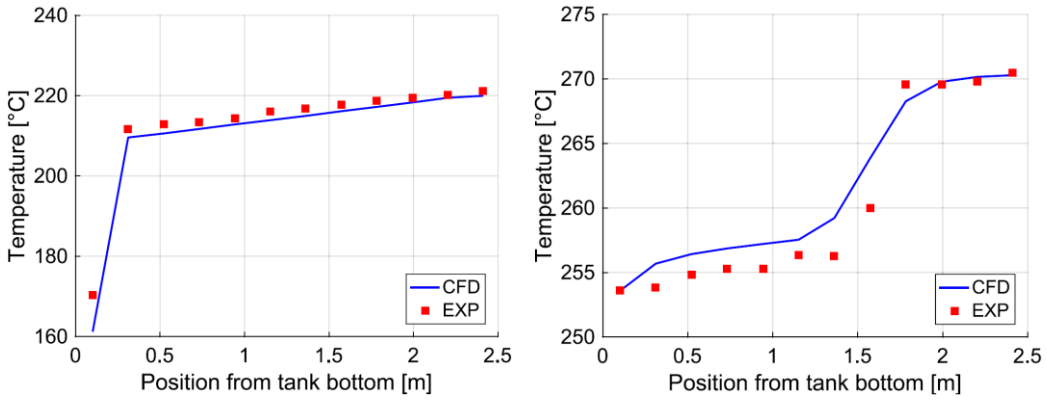

(a) (b)

Figure 5.10: Comparison between experimental and CFD results at the end of: (a) the charging process and (b) the discharging process [105].

5.7.2 PCM lumped-parameter model

The PCM lumped-parameter model has been validated against experimental data reported by [167]. As shown in Figure 5.11, the experimental setup involved two isothermal water baths (A and B), a spherical glass with a diameter of 100 mm, five thermocouples and a data acquisition unit. The sphere was filled with an organic PCM (paraffin) with a melting interval of 45.8-50.3 °C. The first bath (bath A) was employed to establish the initial temperature of the PCM inside the sphere, while

the second bath (bath B) facilitated the melting or solidification of the PCM. Throughout the experiment, PCM temperatures were measured by the five thermocouples positioned along the sphere's centerline, with the data recorded and stored by a data acquisition unit.

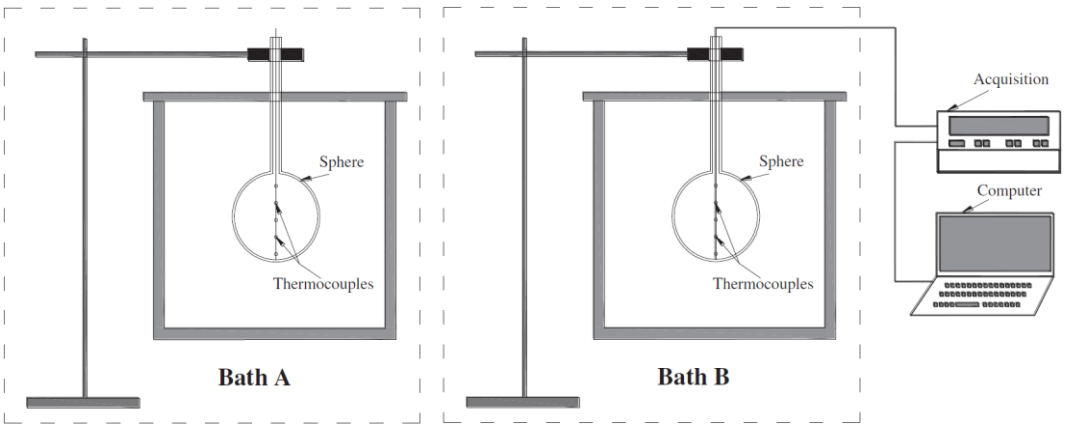

Figure 5.11: Schematic of the experimental setup established by [167]

The experimental procedure started with immersing the sphere into the bath A for a sufficiently long period to attain the initial PCM temperature. Subsequently, the sphere was quickly submerged into the bath B to initiate the melting or solidification process. Regarding the melting process, an initial temperature of 30 °C was considered for the PCM, while a temperature of 60 °C was applied to the Bath B. Conversely, for the solidification process, the PCM temperature was initially considered to be 60 °C, while a temperature of 30 °C was applied to the bath B.

To ensure consistency with the experimental setup, the model parameters were adjusted, including the sphere's diameter and PCM properties. Moreover, the initial temperature of the PCM and the temperature of the tube's outer wall were set based on the experimental conditions for the melting and solidification tests. It is noteworthy that the outer wall temperature was assigned to match the temperature of the bath B. Figure 5.12a shows a comparison between the experimentally measured temperature of the PCM (average from readings obtained by the five thermocouples) and the PCM temperature computed by the lumped-parameter model throughout the melting test. In Figure 5.12b, a similar comparison is made for the solidification process. In both figures, PCM temperatures below 45.8 °C represent the solid region, 45.8 °C to 50.3 °C correspond to the phase transition region, and above 50.3 °C indicate the liquid region. The results shown in Figure

5.12a and Figure 5.12b reveal a good agreement between the computed values and the experimental data across all states (solid, liquid and phase transition) throughout the melting and solidification processes. The coefficient of determination (R^2) is approximately 0.97 for both cases, indicating a strong correlation between the calculated values and the experimental observations.

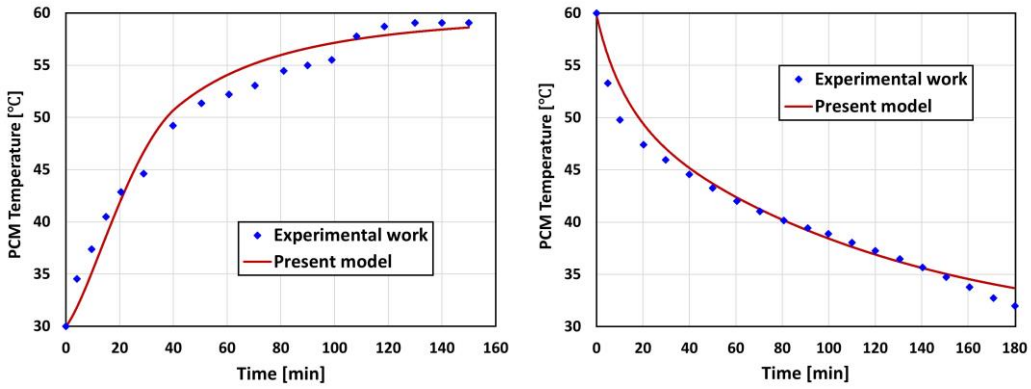

Figure 5.12: Comparison between the experimental data reported by [167] *and the computed results in terms of PCM temperature for: (a) melting and (b) solidification tests.*

5.8 Results and discussion

Several charge-discharge cycles were simulated for various TES configurations by employing the CFD model explained in section 5.5. According to the primary design, an initial uniform temperature of 190 °C was assumed for the whole TES system in the first charging cycle. For the first discharging cycle, the initial temperature would be the same as the temperature distribution resulted at the end of the first charging cycle. Similarly, for the second charging cycle, the initial temperature would be equal to the temperature distribution achieved at the end of the first discharging cycle. Several charge-discharge cycles were simulated until reaching a stable cycle, in which temperature distributions were equal for two consecutive charge-discharge cycles. Figure 5.13 shows temperature profiles at the end of four charge-discharge cycles for Case 2 and Case 3c. As shown, after four charge-discharge cycles, stable temperature distributions can be attained within the tank. Moreover, charging and discharging durations would be equal for the third and fourth cycles, as shown in Figure 5.14. It can be concluded that the fourth cycle would be the stable cycle. Therefore, the results presented in this section are provided for the fourth cycle for various configurations.

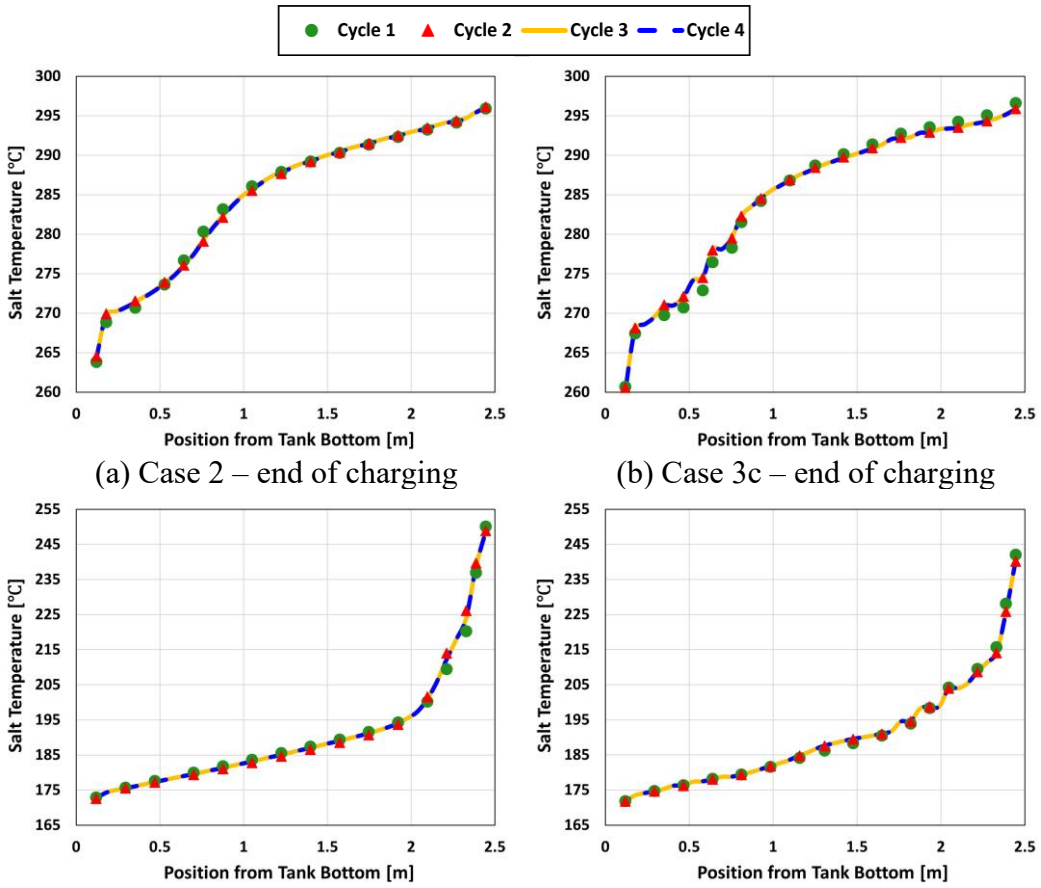

(a) Case 2 – end of charging (b) Case 3c – end of charging

(c) Case 2 – end of discharging (d) Case 3c – end of discharging

Figure 5.13: Comparison of cyclic operation in terms of temperature distribution profiles at the end of each charging/discharging process for Case 2 (without PCM) and Case 3c (with PCM at both top and bottom locations).

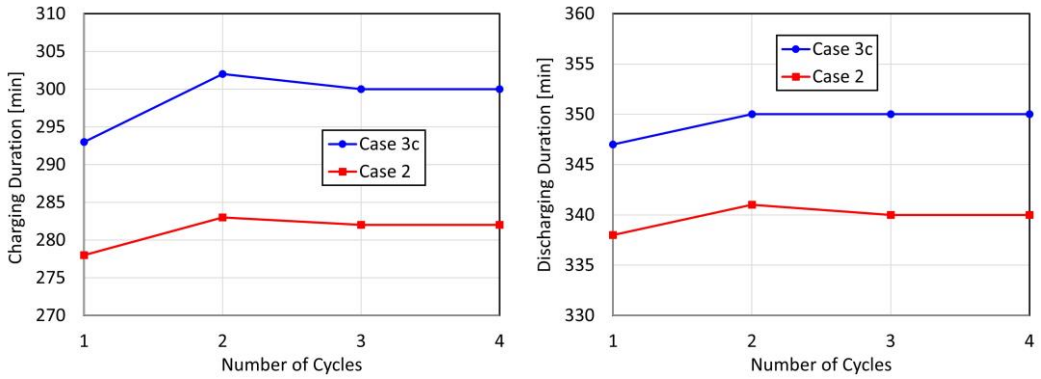

(a) (b)

Figure 5.14: Comparison of cyclic operation in terms of charging/discharging duration for Case 2 (without PCM) and Case 3c (with PCM at both top and bottom locations).

In this section, the thermal performance of various TES systems introduced in Section 5.2 is investigated. For this purpose, the temperature distributions of salt within the tank are presented during the charging and discharging processes. This analysis is conducted for two scenarios: the configuration with a modified tank geometry, as detailed in Section 5.8.1, and the one incorporating PCM tubes, as outlined in Section 5.8.2. Finally, different configurations are compared in terms of thermal performance parameters, as discussed in Section 5.8.3.

5.8.1 Thermocline energy storage system with a modified geometry

To assess the influence of the geometrical improvement measures detailed in Section 5.3 on the distribution of salt temperatures, a comparative analysis is required between the modified configuration (Case 2) and the reference case (Case 1). This evaluation is conducted for the charging process, as discussed in Section 5.8.1.1, and for the discharging process, as outlined in Section 5.8.1.2.

5.8.1.1 Charge process

The temperature evolution of molten salt during the charging process is depicted in Figure 5.15 for Case 1 and Case 2 considering various heights within the tank. In general, the charging process stops when the salt temperature reaches 285 °C on average within the entire tank to achieve the desired temperature at the end of the charging process. However, due to inefficient geometrical features of Case 1, as discussed in section 5.3, much longer charging duration would be required for this configuration, compared to Case 2. As illustrated in Figure 5.15, the charging process takes 417 min for Case 1 and 282 min for Case 2. Nevertheless, the average salt temperature could not reach 285 °C in Case 1, despite a much longer duration compared to Case 2. In fact, since the lowest zone of the tank in Case 1 does not contribute to the natural circulation within the tank, reaching the desired temperature of 285 °C is almost impossible for this configuration, and requires a duration longer than 1000 min (not shown here). It should be noted that very long charging duration might lead to a frozen salt at the bottom of the tank as salt temperature at this region is continuously decreasing. Therefore, the charging transient should stop at a certain time to prevent from salt freezing. This fact can be observed in Figure 5.15, where Case 1 lacks participation of the lowest zone in natural circulation, leading to a persistent temperature decrease at H=0.13 m because of the heat dissipation to the environment. In contrast, involvement of the lowest zone in natural circulation in Case 2 is evident as the salt temperature at

H=0.13 m begins to rise significantly around t=110 min. It can be concluded that the geometric enhancement in Case 2 results in an improvement in the thermal performance, as the entire mass of salt in the tank is engaged in the charge process.

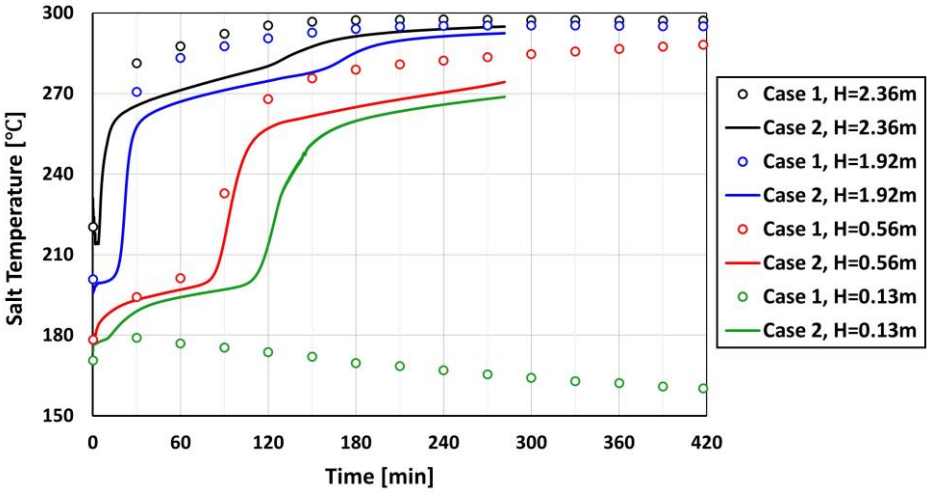

Figure 5.15: Salt temperature evolution during the charge process at different heights within the tank: comparison between the reference and the optimized cases.

Figure 5.16 displays the distribution of salt temperature along the vertical direction within the tank for Case 1 and Case 2 at the end of the charging process. As already explained, the average salt temperature reached 285 °C at the end of the charging process for Case 2, while it could not reach this desired value for Case 1 and reached about 281 °C after 417 min. It is evident from Figure 5.16 that in Case 1, salt temperature is slightly higher at the higher heights within the tank because of the extended duration of the charging process. However, due to the lack of contribution to the natural circulation within the tank at the bottom region in Case 1, salt temperature is substantially higher for Case 2 at this region.

The temperature field is also depicted in Figure 5.17 at the end of the charging process for both cases. Analysis of Figure 5.17 reveals that, for Case 2, the heated volume of the salt within the tank is more extensive compared to Case 1, in which the salt at the bottom zone remains cold by the end of the charging process. This means that the actual storage volume of the tank has increased in the modified geometry. This substantial difference, attributed to the geometrical modification, indicates a significant enhancement in the thermal performance of the system during the charging process, as elaborated in Section 5.8.3.

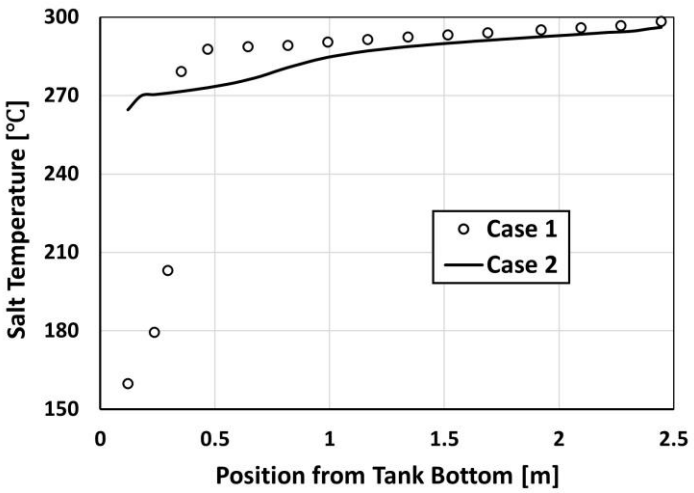

Figure 5.16: Salt temperature distribution along the vertical direction within the tank at the end of the charging process: comparison between the reference and the optimized cases.

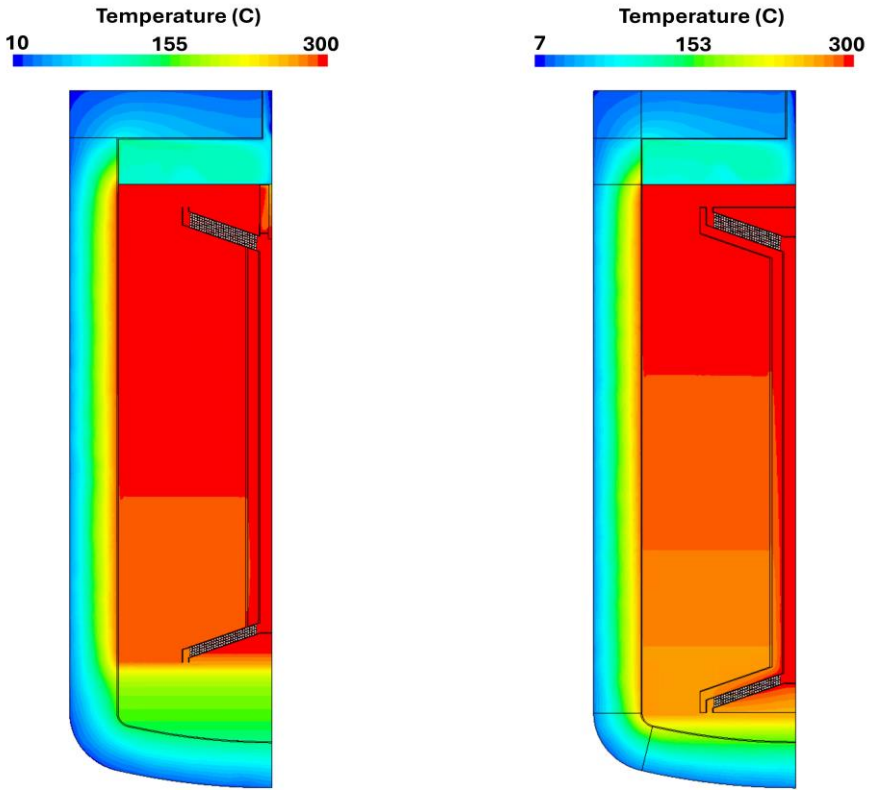

(a) Case 1 (b) Case 2

Figure 5.17: Temperature fields at the end of the charging process

5.8.1.2 Discharge process

The temperature evolution of molten salt during the discharging process is displayed in Figure 5.18 for Case 1 and Case 2 considering various heights within the tank. Similarly to the charge process, in both cases, the discharge transient stopped when the average salt temperature within the entire tank reached 190 °C, according to the primary design specifications. As shown in Figure 5.18, the discharging process takes 400 min and 340 min for Case 1 and Case 2, respectively. The extended duration of the discharging process in Case 1 is attributed to a smaller volume of hot salt involved in the discharging in this configuration. The lower volume of hot salt involved in the discharge process in Case 1 also results in a more rapid decrease in the temperature of the topmost layer compared to Case 2, as illustrated in Figure 5.18.

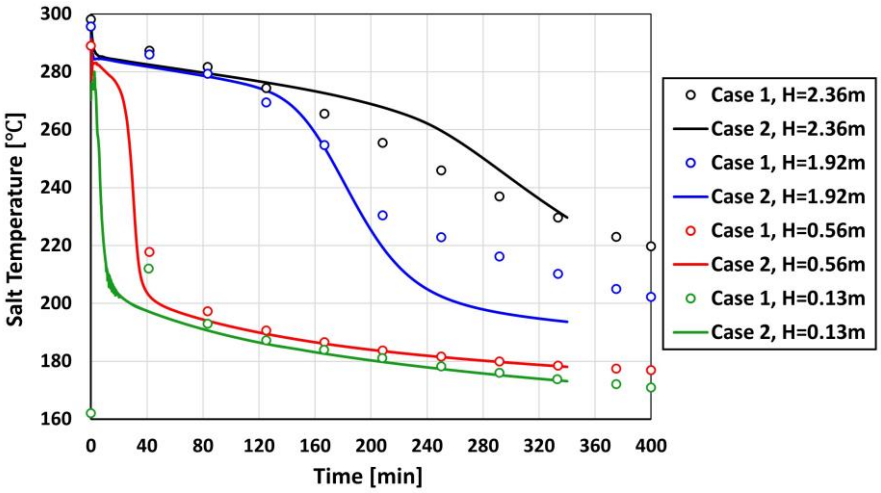

Figure 5.18: Salt temperature evolution during the discharge process at different heights within the tank: comparison between the reference and the optimized cases.

Figure 5.19 shows the distribution of salt temperature along the vertical direction within the tank for Case 1 and Case 2 at the end of the discharging process. As mentioned earlier, both systems reach an average salt temperature of 190 °C at the end of the discharging process. However, contribution of a smaller volume of hot salt to the discharging process in Case 1 allows for reaching a lower salt temperature at the topmost layer at the end of the discharging process. This temperature difference can also be seen in the temperature fields depicted in Figure 5.20, where the maximum salt temperature is 235 °C for Case 1, which is lower than that for Case 2 (249 °C).

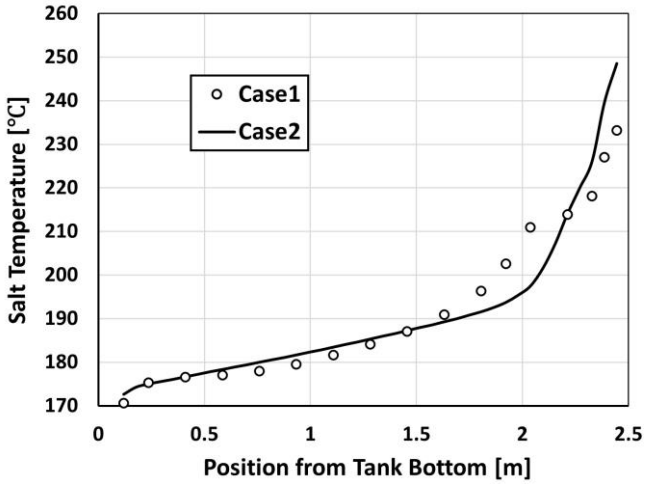

Figure 5.19: Salt temperature distribution along the vertical direction within the tank at the end of the discharging process: comparison between the reference and the optimized cases.

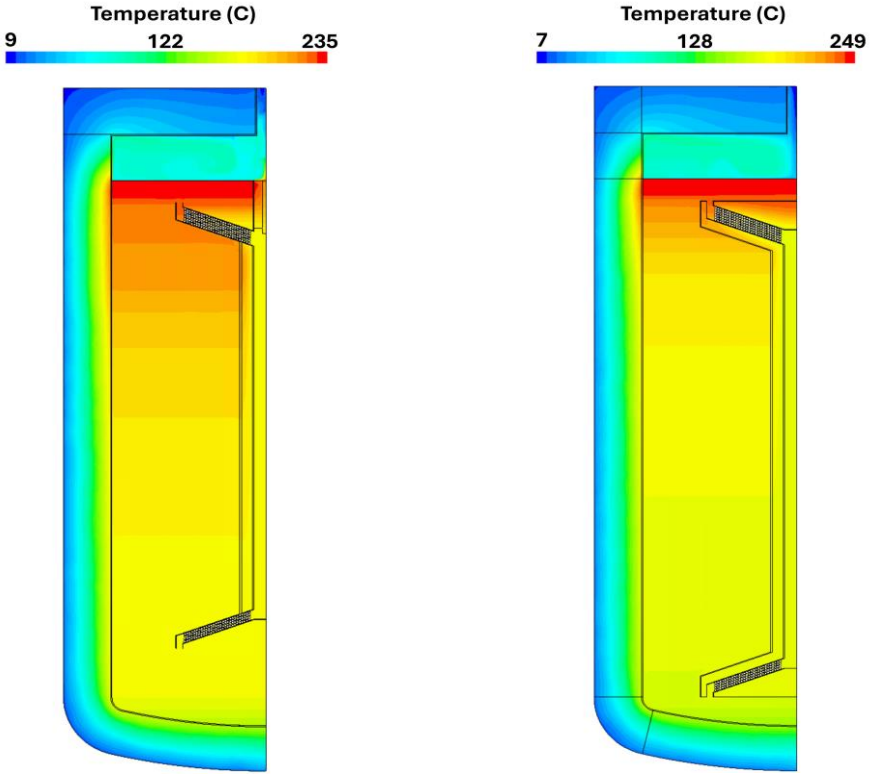

(a) Case 1 (b) Case 2

Figure 5.20: Temperature fields at the end of the discharging process

5.8.2 Thermocline energy storage system with PCM inserts

This section evaluates the impact of the PCM integration on the thermal performance of the thermocline TES system. For this purpose, salt temperature distributions are compared for various configurations, encompassing the geometrically modified case without PCM inserts, as well as diverse scenarios involving PCM insertions during the charge process (refer to Section 5.8.2) and the discharge process (refer to Section 5.8.2.2).

5.8.2.1 Charge process

Figure 5.21 shows the distribution of salt temperature along the vertical direction within the tank for various configurations during the charging process. It is evident from Figure 5.21a that, by t=50 min in Case 3b and Case 3c, portions of PCMs at the bottom location were completely melted, while lower rows of the PCM bank still continue to melt, resulting in a plateau in the salt temperature. Upon complete melting of the whole PCM bank at the bottom location, the plateau disappears, enabling the salt to attain higher temperatures than the PCM melting point (Figure 5.21b, c, d). Furthermore, Figure 5.21a suggests that the thermocline is less sharp for Case 3a and Case 3c compared to Case 2 and Case 3b. This observation is attributed to the substantial thermal conductivity of the PCM tubes, particularly the tube walls. The PCM tube bank functions as a conductive layer, expediting heat transfer between the cold salt below the PCM tube bank and the hot salt above it. This leads to a less sharp thermocline once the thermocline region is close to the upper PCM region. This temperature profile is still kept later during the charging process. Consequently, the salt in the lower regions of the tank experiences an earlier temperature increase in the presence of the upper PCM, resulting in a sharper thermocline for Case 2 and Case 3b compared to Case 3a and Case 3c.

At the subsequent time point (t=120 min in Figure 5.21b), the PCM melting process persists at the top location at specific heights of Case 3a and Case 3c, while the entire PCM bank is melted by the next time point (t=200 min in Figure 5.21c). Furthermore, the PCM at the top location influences the salt temperature not only in the PCM region but also below it; any layers beneath the PCM region could achieve a stabilized salt temperature near the PCM melting point. This occurs because the salt moves downward from the PCM location at a consistent temperature while the PCM is melting. However, as depicted in Figure 5.21d, differences in temperature distributions are minimal among various configurations

at the end of the charging process when average salt temperatures of 285 °C are achieved.

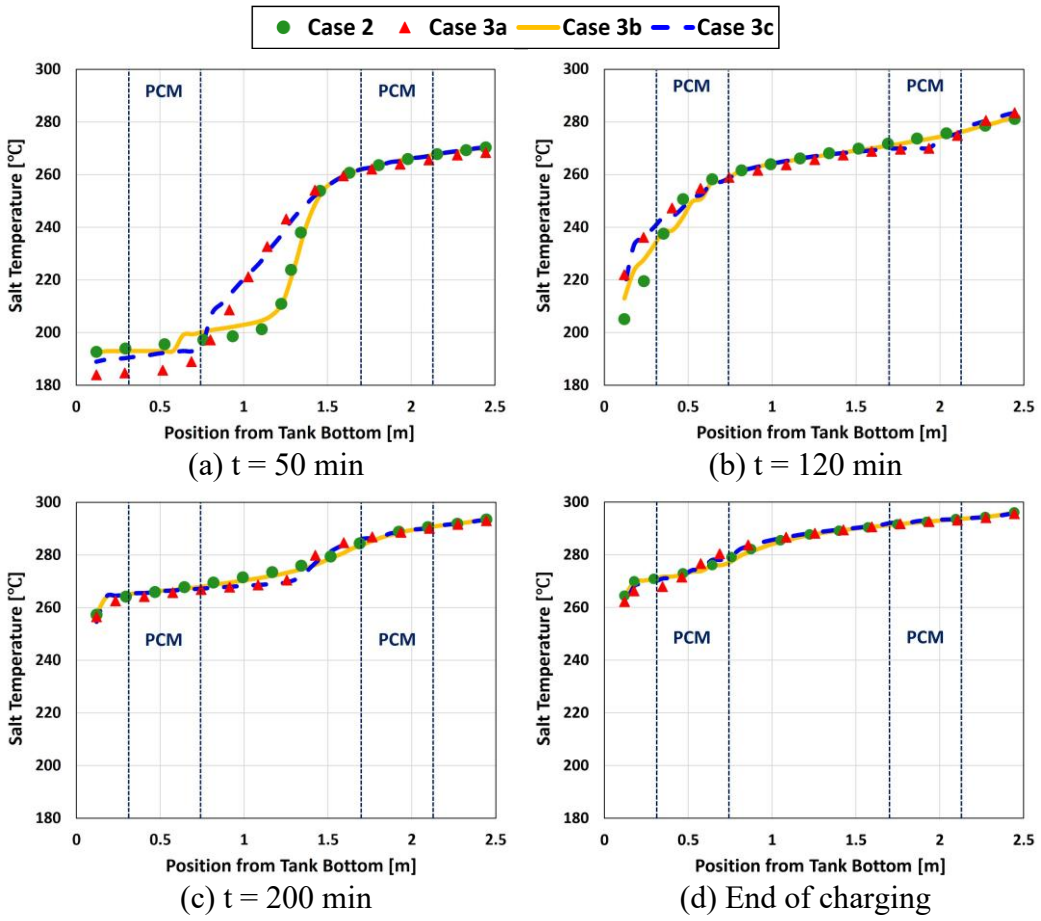

Figure 5.21: Salt temperature distributions along the vertical direction within the tank during the charging process for Case 2 (without PCM), Case 3a (with PCM at top), Case 3b (with PCM at bottom) and Case 3c (with PCM at top and bottom).

The temperature evolution of molten salt during the charging process is displayed in Figure 5.22 for different configurations at PCM inserts heights. Notably, while Case 2 undergoes a charging process lasting 282 min, this duration extends for the cases with PCM inserts: 292 min, 285 min and 300 min for Case 3a, Case 3b and Case 3c, respectively. The prolonged charge transient in the configuration with PCM inserts at both top and bottom locations is primarily attributed to the extended time required for PCM phase change. For the PCM in the top region, melting duration is approximately 35 min (Case 3a and Case 3c in Figure

5.22a), while for the PCM located in the bottom region, melting duration is about 30 min (Case 3b and Case 3c in Figure 5.22b).

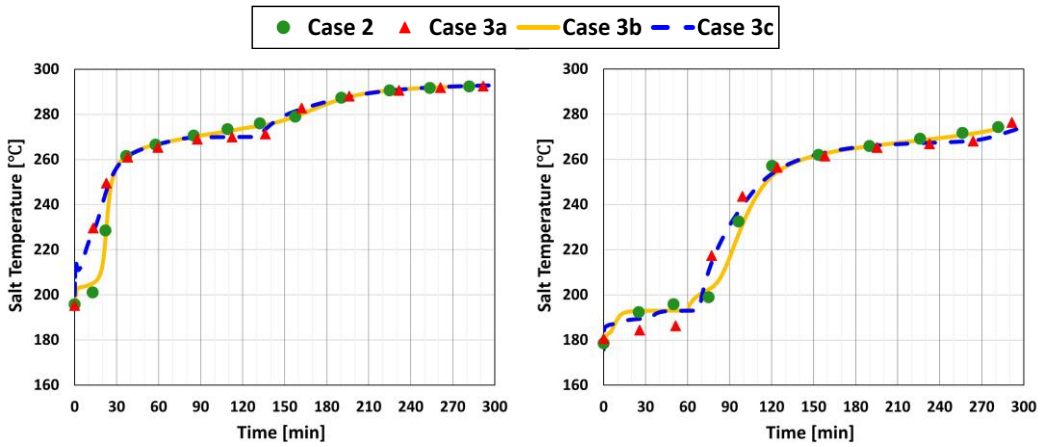

(a) H = 1.92 m (b) H = 0.56 m

Figure 5.22: Salt temperature evolution during the charging process at PCM inserts heights considering Case 2 (without PCM), Case 3a (with PCM at top), Case 3b (with PCM at bottom) and Case 3c (with PCM at top and bottom).

5.8.2.2 Discharge process

Figure 5.23 displays the distribution of salt temperature along the vertical direction within the tank for various configurations during the discharging process. At t=50 min (Figure 5.23a), the PCM impact is not evident as the salt temperature is still higher than the PCM solidification temperature at each top or bottom location. Additionally, it can be seen in Figure 5.23a that the configurations with PCM in the bottom region (Case 3b and Case 3c) exhibit a less sharp thermocline in comparison with Case 2 and Case 3a. As discussed in Section 5.8.2, the PCM tube bank serves as a conductive layer because of a high thermal conductivity provided by the PCM tubes, facilitating heat transfer between the cold salt below the PCM bank and the hot salt above it. Consequently, the salt temperature above the lower PCM bank decreases earlier during the discharge process, leading to a less sharp thermocline for the configurations with PCM at the bottom location.

Investigating the subsequent time point (t=120 min in Figure 5.23b) reveals that the PCM solidification process persists at both top and bottom locations at specific heights of Case 3a, Case 3b and Case 3c, while complete solidification occurs by t=200 min (Figure 5.23c). Moreover, in Case 3b and Case 3c, the PCM at the bottom location slightly influences the regions above the PCM zone through stabilizing the salt temperature. This occurs because the salt moves upward from the PCM location

at a consistent temperature during the PCM solidification. However, at the end of the discharging process when an average salt temperature of 190 °C is achieved, differences in temperature distributions are minimal among various configurations, as depicted in Figure 5.23d.

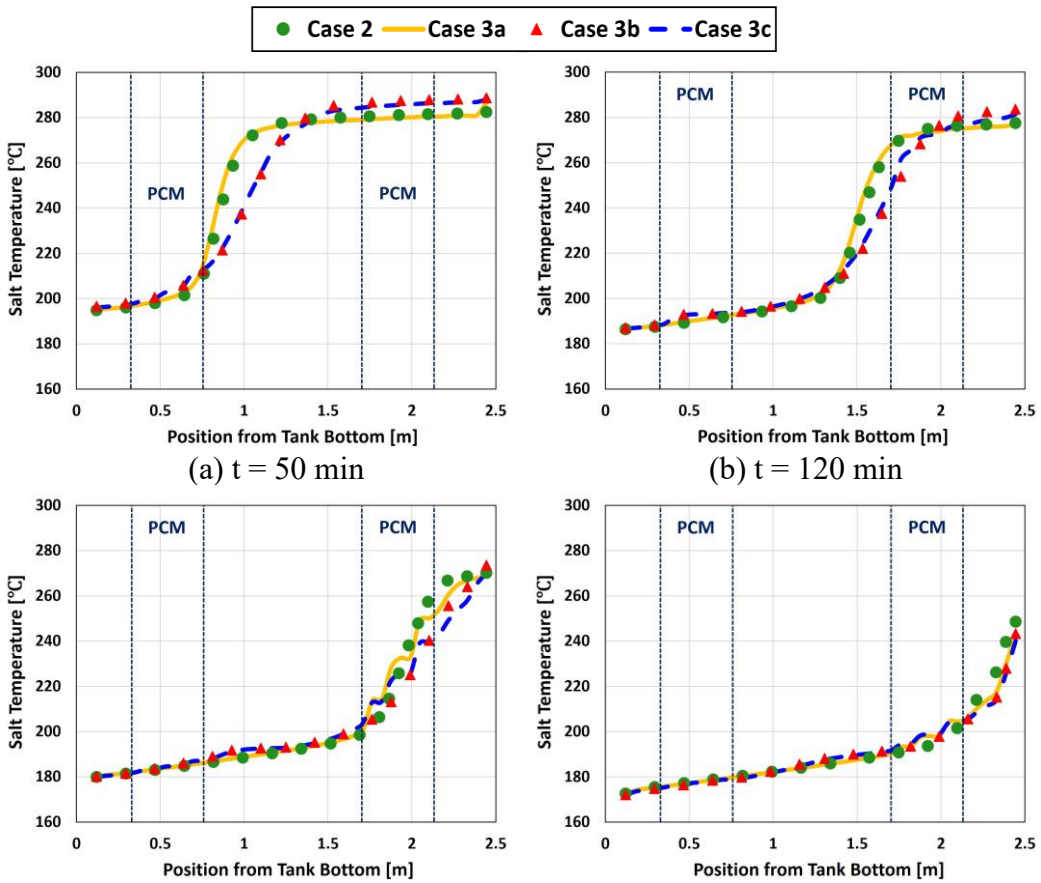

Figure 5.23: Salt temperature distributions along the vertical direction within the tank during the discharging process for Case 2 (without PCM), Case 3a (with PCM at top), Case 3b (with PCM at bottom) and Case 3c (with PCM at top and bottom).

Figure 5.24 shows the temperature evolution of molten salt at PCM inserts heights for different configurations during the discharging process. As can be observed, the configurations with PCM inserts exhibit longer transients in comparison with the case without PCM. The discharge transient durations are 340 min, 348 min, 348 min, and 350 min for Case 2, Case 3a, Case 3b, and Case 3c, respectively. This difference is primarily attributed to the extended time required for PCM phase change. As shown in Figure 5.24a, for all configurations, there is a moderate decline in salt temperature at H=1.92 m at the beginning of the transient,

followed by a sharp decrease at a particular time (between t=120 min and t=150 min for various cases). This sharp trend results in a significant temperature gradient in the top zone of the tank, expediting the PCM solidification in Case 3a and Case 3c. A comparison between Figure 5.24a and Figure 5.24b reveals a more prolonged solidification process for the PCM at the bottom location (approximately 30 min for Case 3b and Case 3c in Figure 5.24b) in comparison with the PCM at the top location (approximately 10 min for Case 3a and Case 3c in Figure 5.24a). This longer duration for the PCM at the bottom location is due to a slight temperature gradient in the bottom zone of the tank during the discharging process.

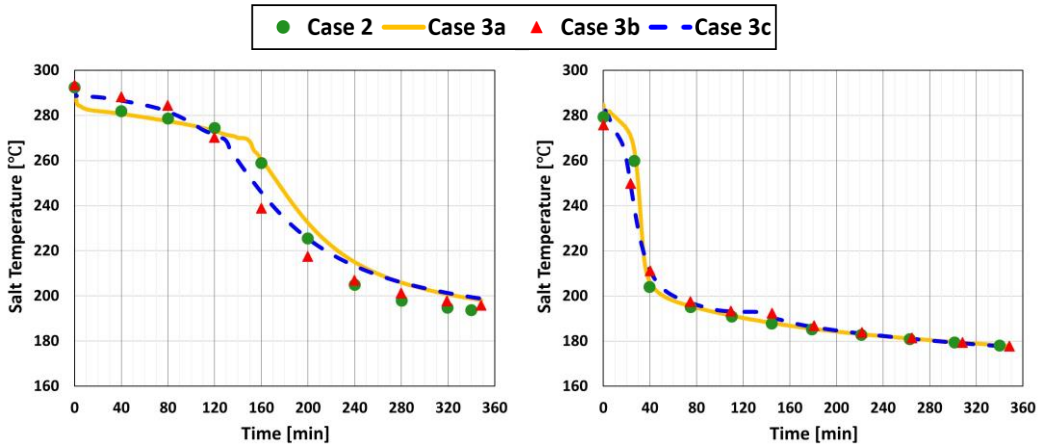

(a) H = 1.92 m (b) H = 0.56 m

Figure 5.24: Salt temperature evolution during the discharge process at PCM inserts heights considering Case 2 (without PCM), Case 3a (with PCM at top), Case 3b (with PCM at bottom) and Case 3c (with PCM at top and bottom).

5.8.3 Comparative performance analysis

To evaluate the thermal performance of the various TES systems introduced in the present study, conducting a thorough comparative analysis is essential. In this regard, stored and recovered energy are provided for different configurations during the charge and discharge processes. Additionally, a comparative performance analysis is carried out based on the performance parameters defined for the charge and discharge processes. For this purpose, three key parameters are defined, including charging efficiency, discharging efficiency, and overall efficiency.

The charging efficiency is computed by [168]:

$$\eta_{ch} = \frac{E_{stored}}{E_{input,oil}} \tag{5.16}$$

where E_{stored} represents the energy stored within the system and $E_{input,oil}$ denotes the energy provided by the oil in the charge process.

The discharging efficiency can be given by [168]:

$$\eta_{disch} = \frac{E_{recovered,oil}}{E_{stored}} \tag{5.17}$$

where $E_{recovered,oil}$ represents the energy recovered by the oil in the discharge process.

The overall efficiency can be expressed as [106]:

$$\eta_{overall} = \eta_{ch} \cdot \eta_{disch} = \frac{E_{recovered,oil}}{E_{input,oil}} \tag{5.18}$$

Figure 5.25a illustrates the stored and recovered energy during the charge and discharge processes and Figure 5.25b outlines the performance parameters for various TES systems. As shown in Figure 5.25a, in the absence of PCM, the geometrically modified configuration demonstrates a greater stored energy during the charging process compared to the reference case (approximately 256 kWh and 248 kWh, respectively), reflecting a 3% increase. Similarly, the modified configuration exhibits a higher energy recovery during the discharging process in contrast to the reference case (approximately 234 kWh and 229 kWh, respectively), representing an increase of 2.3%. This enhanced performance is attributed to the involvement of a larger salt volume in the process, facilitated by the implemented geometric modifications.

Furthermore, additional improvements in both stored and recovered energy are attainable through the PCM integration, owing to the enhanced capacity for heat storage and heat release facilitated by the latent heat of PCM. As shown in Figure 5.25a, the highest levels of stored and recovered energy are observed in Case 3c, where PCMs are integrated at both top and bottom locations (approximately 290 kWh and 264 kWh, respectively). This signifies that the PCM integration would increase the stored and recovered energy by 13.6% and 12.7%, respectively.

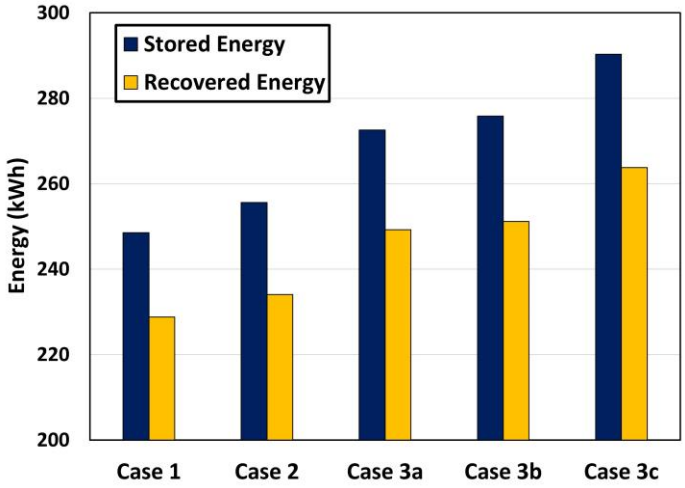

(a)

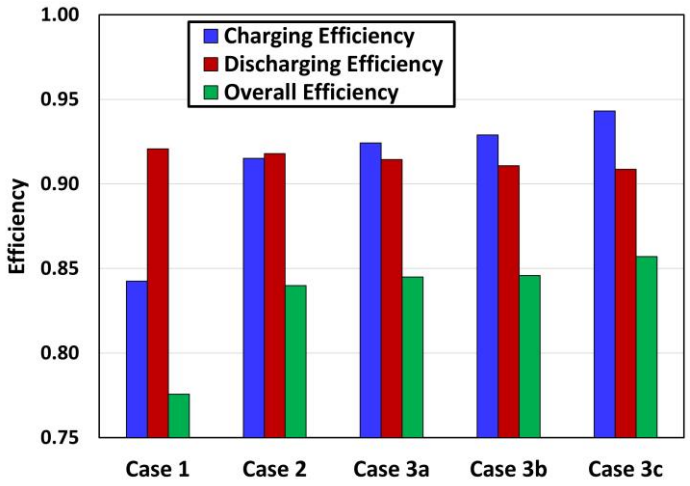

(b)

Figure 5.25: Comparative performance analysis of various TES systems in terms of: (a) stored and recovered energy, and (b) charging, discharging and overall efficiency.

Furthermore, it is evident from Figure 5.25b that despite a slight difference in the discharging efficiency between the configuration with a modified geometry (Case 2) and the reference case (Case 1), the charging efficiency is much higher for Case 2 with 91.5%, compared to case 1 with 84.2%. This huge difference is due to addressing ineffective geometric features of the reference case, leading to a more efficient heat storage by involving the entire tank in the charging process. This improvement also resulted in a remarkable difference in the overall efficiency, with 77.6% and 84% for case 1 and case 2, respectively.

Additionally, Figure 5.25b indicates that the PCM integration results in an increase in the charging efficiency. Among all configurations, Case 3c achieves the greatest charging efficiency with 94.3%. Improved charging efficiency with the PCM integration implies a decrease in the ratio of heat loss to the energy supplied by the oil in the charge process. This could be due to the effective absorption of the thermal energy by the PCMs, reducing thermal losses to the environment. Concerning the discharge process, the discharging efficiency slightly decreases by the PCM integration, with a maximum reduction of about 1% for Case 3c. This minor reduction in the discharging efficiency could be due to the fact that the PCMs contribute to thermal losses to a slightly greater extent than the molten salt. However, the configurations with the PCM inserts indicate higher overall efficiencies compared to the case without PCM. Case 3c achieves the highest overall efficiency with 85.7%, highlighting a 1.7% increase compared to Case 2.

Overall, investigation of Figure 5.25 reveals that the PCM integration not only increases stored and recovered energy during the charging and discharging processes, but also enhances the overall efficiency of the charge-discharge cycle. Consequently, incorporating the PCMs into the thermocline tank would be beneficial for the TES system.

5.9 Concluding remarks

This chapter presented enhanced configurations of TES systems based on the thermocline technology. The study performed enhancement strategies on a reference case (Case 1) in terms of geometrical modification and PCM integration. In this regard, the tank geometry was adjusted to move the charge HX shell to the tank bottom, promoting natural circulation of the salt. Thermal insulations were also considered for both HX shells to prevent disadvantageous heat transfer during the charge and discharge processes (Case 2). Subsequently, PCM tubes were strategically inserted at various heights within the tank, positioned near the top (discharge) HX (Case 3a), near the bottom (charge) HX (Case 3b) and at both top and bottom locations (Case 3c). This integration of PCM could facilitate an augmentation in the thermal storage capacity of the system through the PCM latent heat and could stabilize the salt temperature at the HX locations. Based on the anticipated salt temperatures in each region, $NaNO_2$ and $LiNO_3$-$NaNO_3$ (57:43 wt.%) were selected for the top and bottom locations, respectively. The geometric properties of the PCM tube banks were determined through a geometrical optimization conducted on the PCM inserts.

To determine the distribution of salt temperature within the tank, a validated transient 2D CFD model was developed, accounting for buoyancy-driven salt motion during the charge and discharge processes. This model was linked with a PCM lumped-parameter model, intending to compute PCM temperature and the corresponding heat transfer coefficient. The model was validated against experimental data.

Investigation of the TES systems during the charge process revealed that, due to inefficient geometrical features of Case 1, much longer charging duration would be required for this configuration, compared to Case 2. However, the average salt temperature could not reach the desired value of 285 °C in Case 1, despite a much longer duration compared to Case 2. In fact, since the lowest zone of the tank in Case 1 does not contribute to the natural circulation within the tank, reaching the desired temperature of 285 °C is almost impossible for this configuration. As a result, the modified configuration signifies a higher stored energy in comparison with the reference case at the end of the charge process, reflecting a nearly 3% increase. Concerning the discharge process, geometrical enhancement measures resulted in a shorter transient for the modified configuration. The extended duration of the discharging process in Case 1 is attributed to a smaller volume of hot salt involved in the discharging in this configuration. In addition, a greater amount of energy was recovered by the modified case in comparison with the reference case, indicating a 2.3% increase. The increased energy stored and recovered by the modified tank implies an enhancement in the thermal performance of the TES system. This improvement was also confirmed by evaluating the key performance parameters of the systems, where an increase of 6.4% was observed in the overall efficiency of the charge-discharge cycle for Case 2.

The PCM integration indicated a further improvement in the thermal performance of the thermocline TES system. For both charging and discharging processes, PCM insertion prolonged the transient duration because of the extended time required for PCM phase change. The configuration with PCM in both top and bottom regions (Case 3c) had the most prolonged transient. Case 3c also demonstrated the greatest stored and recovered energy due to the PCM latent heat, implying an increase of approximately 13.6% and 12.7% respectively, compared to Case 2.

Additionally, the PCM integration enhanced the charging efficiency of the thermocline TES system. Among all configurations, Case 3c achieved the highest charging efficiency with 94.3%. However, the discharging efficiency experienced

a slight decrease by the PCM integration, with a maximum reduction of about 1% for Case 3c. Regarding the overall efficiency of the charge-discharge cycle, Case 3c demonstrated the most efficient performance with an overall efficiency of 85.7%, indicating a 1.7% increase compared to Case 2. In conclusion, the PCM integration would be advantageous to the TES system since it not only increases stored and recovered energy, but also enhances the overall efficiency of the charge-discharge cycle.

Chapter 6

Conclusions and Perspective

This dissertation aims to propose effective solutions for enhancing the overall performance and minimizing the costs of different CSP technologies, thereby strengthening its competitiveness compared to other renewable systems. To achieve this goal, two key components of linear CSP technologies including receiver unit and TES system were investigated computationally to identify strategies for improving their operational performance and reducing the costs. In addition, a comparative techno-economic analysis of various linear CSP technologies was conducted to provide detailed guidelines for the selection of the most profitable technology.

Three main investigations were carried out through computational studies: firstly, the optimization of the photo-thermal performance of a PTC by implementing multiple selective coatings arrayed along the receiver tube; secondly, a comparative techno-economic assessment of various linear CSP technologies, including PTC and LFC with evacuated and non-evacuated receiver tubes; thirdly, the thermal performance enhancement of a case study thermocline TES system through geometrical modifications and PCM integration.

Conducting a computational study to identify the photo-thermally optimized configuration of a PTC receiver tube was the primary focus of this research. The present study adopted an approach in which multiple selective coatings are arranged along the collector line based on their photo-thermal performance at various HTF temperatures (290 ℃ to 550 ℃). A lumped-parameter model was developed along the radial direction of the receiver tube to calculate absorber tube wall temperature

and heat losses at different HTF temperatures. Then, a 1D model was developed along the collector axis, employing heat losses correlations, to determine HTF temperature profile along the receiver tube. Furthermore, the tube wall temperatures computed by the lumped-parameter model were utilized to obtain photo-thermal efficiencies for six selective coatings. The results showed that the most photo-thermally effective distribution encompasses three selective coatings, characterized by three temperature ranges. A negligible difference of less than 1% was observed between the results obtained for wind speeds of 0 and 15 m/s, due to the thermal insulation provided by the vacuum in the gap region. The optimized PTC configuration benefitted from an increase of 0.5-1.9% in the overall photo-thermal efficiency compared to the single-coated collectors. In addition, this strategy might offer financial advantages since the more expensive selective coatings is applied only to the final segment of the collector. Consequently, considering any given solar heat flux, HTF temperature range and mass flow rate, a shorter PTC receiver tube is required for an optimized configuration, incurring lower costs.

The second critical goal of this study was to perform a techno-economic feasibility assessment of linear CSP systems. In this respect, four CSP technologies were investigated, comprising PTC and LFC with evacuated and non-evacuated receiver tubes. This study was carried out based on the LCOE considering four different locations worldwide, characterized by various levels of DNI. The LCOE depends on economic data and net annual energy yield. While economic data was derived from literature, net annual energy yield was calculated by a 1D axial model, incorporating hourly meteorological data for the entire year. This 1D model was supported by an optical ray-tracing model to provide incident solar power on the tube, and by a radial lumped-parameter model to obtain heat losses for various HTF temperatures. Moreover, a 2D steady-state CFD model was developed in the case of the LFC receiver unit, where the presence of the secondary reflector necessitates computing ad-hoc correlations for the convective heat transfer between the glass tube and the environment. The results of the CFD study revealed that convective heat loss is substantially lower in the LFC receiver unit compared to the PTC owing to the semi-cavity impact of the secondary reflector, protecting the receiver tube against wind. According to the results of the annual-based thermal performance analysis, the PTC could provide higher net annual energy yield compared to the LFC because of the higher optical efficiency. This difference is less significant in the case of non-evacuated tubes due to lower heat losses from the LFC receiver tube. Furthermore, conducting an economic analysis demonstrated that the evacuated PTC is the most economical configuration among various linear CSP technologies. This is mainly owing to the higher optical efficiency and,

consequently, higher net annual energy yield, which outweighs the higher capital cost of the PTC. However, for the non-evacuated configuration, the LFC could be more economical than the PTC, where the lower capital cost is more dominant than the lower net annual energy yield. In addition, this study reported that the cost of evacuation could be justified due to an enhancement in the thermal performance, leading to a lower LCOE for the evacuated tubes compared to the non-evacuated ones. Finally, a sensitivity study was carried out based on the key parameters influencing the LCOE. It was found that an improvement of nearly 6% in the annual optical performance of the evacuated LFC could result in the same LCOE of the PTC. Similarly, a reduction of about 4% in the capital cost of the evacuated LFC could make it as economical as the PTC.

Finally, the third objective of this dissertation was to present enhanced configurations of the thermocline TES system. For this purpose, two enhancement measures were implemented in a case study, including geometric modifications and PCM integration. To modify the tank geometry, the charge HX shell was moved to the tank bottom, and thermal insulations were provided for both HX shells. In the subsequent step, PCM toroidal tubes were incorporated into the tank with three strategies: near the top (discharge) HX, near the bottom (charge) HX and at both top and bottom locations. This policy could result in an increase of about 23% in the thermal storage capacity of the TES system caused by the PCM latent heat. Furthermore, incorporating PCM tubes into the TES system could stabilize the salt temperature close to the HX locations. To compute the distribution of molten salt temperature within the tank, a transient 2D CFD model was developed. In the presence of the latent heat, this model was coupled with a PCM lumped-parameter model to provide PCM temperature and heat transfer coefficient. Based on the results obtained for the charge and discharge processes, the geometrically modified configuration demonstrated a shorter transient compared to the reference case. This is mainly due to the contribution of the tank bottom in the thermal stratification within the system. As a result, the modified TES system could attain an increase of about 3% and 2.3% compared to the reference case in terms of stored and recovered energy at the end of the charging and discharging processes, respectively. This performance improvement was also proven by investigating the key performance parameters, where an increase of about 6.4% was observed in the overall efficiency of the charge-discharge cycle by the geometric modification. PCM integration could also further enhance the thermal performance of the TES system. Regarding both charging and discharging processes, PCM insertion led to an extended transient duration owing to the prolonged time required for PCM phase change. The case with PCM at both top and bottom locations exhibited the greatest stored and

recovered energy due to the PCM latent heat, implying an increase of about 13.6% and 12.7% respectively, compared to the case without PCM. This configuration could also achieve the highest overall efficiency of the charge-discharge cycle with 85.7%, indicating a 1.7% increase compared to the case without PCM. It can be concluded that the PCM integration would be advantageous to the TES system due to the increase of stored energy, recovered energy, and overall efficiency of the charge-discharge cycle.

In perspective, the present dissertation could motivate several future investigations:

- The photo-thermal optimization study performed for the PTC might be further extended by conducting a techno-economic feasibility assessment to quantify the economic advantages offered by the adopted strategy.
- The two ad-hoc correlations developed for the Nusselt number in the LFC receiver unit could be validated through experimental studies.
- The techno-economic analysis of linear CSP systems might be conducted considering different selective coatings, particularly for the non-evacuated configuration, which encounters the issue of the stability in air at high temperatures.
- The impact of the enhancement strategies employed for the thermocline TES system could be further investigated by system-level modelling of the CSP plant, encompassing solar field, TES system and power block.
- The thermocline TES systems proposed in this dissertation could be developed experimentally to validate the results obtained for the charge and discharge processes.

References

[1] van Vuuren, D. P., Stehfest, E., Gernaat, D. E. H. J., Doelman, J. C., van den Berg, M., Harmsen, M., de Boer, H. S., Bouwman, L. F., Daioglou, V., Edelenbosch, O. Y., Girod, B., Kram, T., Lassaletta, L., Lucas, P. L., van Meijl, H., Müller, C., van Ruijven, B. J., van der Sluis, S., and Tabeau, A., 2017, "Energy, Land-Use and Greenhouse Gas Emissions Trajectories under a Green Growth Paradigm," Global Environmental Change, **42**, pp. 237–250. https://doi.org/10.1016/j.gloenvcha.2016.05.008.

[2] Ahmad, T., and Zhang, D., 2020, "A Critical Review of Comparative Global Historical Energy Consumption and Future Demand: The Story Told so Far," Energy Reports, **6**, pp. 1973–1991. https://doi.org/10.1016/j.egyr.2020.07.020.

[3] Işık, C., Kuziboev, B., Ongan, S., Saidmamatov, O., Mirkhoshimova, M., and Rajabov, A., 2024, "The Volatility of Global Energy Uncertainty: Renewable Alternatives," Energy, **297**, p. 131250. https://doi.org/10.1016/j.energy.2024.131250.

[4] Rahman, A., Murad, S. M. W., Mohsin, A. K. M., and Wang, X., 2024, "Does Renewable Energy Proactively Contribute to Mitigating Carbon Emissions in Major Fossil Fuels Consuming Countries?," J Clean Prod, **452**, p. 142113. https://doi.org/10.1016/j.jclepro.2024.142113.

[5] Wang, J., and Azam, W., 2024, "Natural Resource Scarcity, Fossil Fuel Energy Consumption, and Total Greenhouse Gas Emissions in Top Emitting Countries," Geoscience Frontiers, **15**(2), p. 101757. https://doi.org/10.1016/j.gsf.2023.101757.

[6] Blondeel, M., Price, J., Bradshaw, M., Pye, S., Dodds, P., Kuzemko, C., and Bridge, G., 2024, "Global Energy Scenarios: A Geopolitical Reality Check," Global Environmental Change, **84**, p. 102781. https://doi.org/10.1016/j.gloenvcha.2023.102781.

[7] Hassan, Q., Viktor, P., J. Al-Musawi, T., Mahmood Ali, B., Algburi, S., Alzoubi, H. M., Khudhair Al-Jiboory, A., Zuhair Sameen, A., Salman, H. M., and Jaszczur, M., 2024, "The Renewable Energy Role in the Global Energy Transformations," Renewable Energy Focus, **48**, p. 100545. https://doi.org/10.1016/j.ref.2024.100545.

[8] International Energy Agency, 2023, *Net Zero Roadmap: A Global Pathway to Keep the 1.5 °C Goal in Reach*, Paris, https://www.iea.org/reports/net-zero-roadmap-a-global-pathway-to-keep-the-15-0c-goal-in-reach.

[9] International Energy Agency, 2023, *World Energy Outlook*, Paris, https://origin.iea.org/reports/world-energy-outlook-2023.

[10] International Energy Agency, 2021, *Net Zero by 2050: A Roadmap for the Global Energy Sector*, Paris, https://www.iea.org/reports/net-zero-by-2050.

[11] Anika, O. C., Nnabuife, S. G., Bello, A., Okoroafor, E. R., Kuang, B., and Villa, R., 2022, "Prospects of Low and Zero-Carbon Renewable Fuels in 1.5-Degree Net Zero Emission Actualisation by 2050: A Critical Review," Carbon Capture Science & Technology, **5**, p. 100072. https://doi.org/10.1016/j.ccst.2022.100072.

[12] International Energy Agency, 2020, *World Energy Outlook*, Paris, https://www.iea.org/reports/world-energy-outlook-2020.

[13] United Nations, 2015, *Paris Agreement*, https://unfccc.int/sites/default/files/english_paris_agreement.pdf.

[14] Intergovernmental Panel on Climate Change (IPCC), 2018, *Global Warming of 1.5 °C: IPCC Special Report on the Impacts of Global Warming of 1.5°C above Pre-industrial Levels and Related Global Greenhouse Gas Emission Pathways*, https://www.ipcc.ch/sr15/.

[15] Feder, T., 2011, "Scientists Help Make Deserts into Solar-Energy Hubs," Phys Today, **64**(7), pp. 21–23. https://doi.org/10.1063/PT.3.1157.

[16] Global Solar Atlas, 2024, "Https://Globalsolaratlas.Info/Map."

[17] Daxini, R., and Wu, Y., 2024, "Review of Methods to Account for the Solar Spectral Influence on Photovoltaic Device Performance," Energy, **286**, p. 129461. https://doi.org/10.1016/j.energy.2023.129461.

[18] Abdulla, H., Sleptchenko, A., and Nayfeh, A., 2024, "Photovoltaic Systems Operation and Maintenance: A Review and Future Directions," Renewable and Sustainable Energy Reviews, **195**, p. 114342. https://doi.org/10.1016/j.rser.2024.114342.

[19] Yousef, B. A. A., Obaideen, K., AlMallahi, M. N., Alajmi, N., Radwan, A., Al-Shihabi, S., and Elgendi, M., 2024, "On the Contribution of Concentrated Solar Power (CSP) to the Sustainable Development Goals (SDGs): A Bibliometric Analysis," Energy Strategy Reviews, **52**, p. 101356. https://doi.org/10.1016/j.esr.2024.101356.

[20] Alam, Md. I., Nuhash, M. M., Zihad, A., Nakib, T. H., and Ehsan, M. M., 2023, "Conventional and Emerging CSP Technologies and Design Modifications: Research Status and Recent Advancements," International Journal of Thermofluids, **20**, p. 100406. https://doi.org/10.1016/j.ijft.2023.100406.

[21] Kalair, A. R., Dilshad, S., Abas, N., Seyedmahmoudian, M., Stojcevski, A., and Koh, K., 2021, "Application of Business Model Canvas for Solar Thermal Air Conditioners," Front Energy Res, **9**. https://doi.org/10.3389/fenrg.2021.671973.

[22] Gong, J., Jiang, Z., Luo, X., Du, B., Wang, J., and Lund, P. D., 2020, "Straight-through All-Glass Evacuated Tube Solar Collector for Low and Medium Temperature Applications," Solar Energy, **201**, pp. 935–943. https://doi.org/10.1016/j.solener.2020.03.069.

[23] Lasluisa, D., Salas, D., Mazet, N., and Aussel, D., 2024, "Multidimensional Analysis for the Techno-Economic Study of the CSP Plant," J Energy Storage, **86**, p. 110732. https://doi.org/10.1016/j.est.2024.110732.

[24] DLR, 2021, *Solar Thermal Power Plants - Heat, Electricity and Fuels from Concentrated Solar Power*, https://www.dlr.de/en/media/publications/brochures/2021/brochure-study-solar-thermal-power-plants/.

[25] Shankar, A., Saxena, A. K., and Mazumdar, R., 2024, *Concentrating Solar Power Plants with Storage: Deployment Essential Now*, The Energy and Resources Institute (TERI), https://www.teriin.org/policy-brief/concentrating-solar-power-plants-storage-deployment-essential-now.

[26] Australian Renewable Energy Agency (ARENA), 2018, *Comparison of Dispatchable Renewable Electricity Options - Technologies for an Orderly Transition*, https://arena.gov.au/assets/2018/10/Comparison-Of-Dispatchable-Renewable-Electricity-Options-ITP-et-al-for-ARENA-2018.pdf.

[27] He, Y.-L., Xiao, J., Cheng, Z.-D., and Tao, Y.-B., 2011, "A MCRT and FVM Coupled Simulation Method for Energy Conversion Process in Parabolic Trough Solar Collector," Renew Energy, **36**(3), pp. 976–985. https://doi.org/10.1016/j.renene.2010.07.017.

[28] Qiu, Y., Li, M.-J., Wang, K., Liu, Z.-B., and Xue, X.-D., 2017, "Aiming Strategy Optimization for Uniform Flux Distribution in the Receiver of a Linear Fresnel Solar Reflector Using a Multi-Objective Genetic Algorithm," Appl Energy, **205**, pp. 1394–1407. https://doi.org/10.1016/j.apenergy.2017.09.092.

[29] Qiu, Y., He, Y.-L., Li, P., and Du, B.-C., 2017, "A Comprehensive Model for Analysis of Real-Time Optical Performance of a Solar Power Tower with a Multi-Tube Cavity Receiver," Appl Energy, **185**, pp. 589–603. https://doi.org/10.1016/j.apenergy.2016.10.128.

[30] Rajan, A., and Reddy, K. S., 2024, "Integrated Optical-Thermal Model and Deep Learning Technique to Estimate the Performance of a Conical Cavity Receiver Coupled Solar Parabolic Dish Collector," Energy Convers Manag, **301**, p. 118052. https://doi.org/10.1016/j.enconman.2023.118052.

[31] Hamada, M. A., Ehab, A., Khalil, H., Al-Sood, M. M. A., and Sharshir, S. W., 2023, "Thermal Performance Augmentation of Parabolic Trough Solar Collector Using Nanomaterials, Fins and Thermal Storage Material," J Energy Storage, **67**, p. 107591. https://doi.org/https://doi.org/10.1016/j.est.2023.107591.

[32] Alamdari, P., Khatamifar, M., and Lin, W., 2024, "Heat Loss Analysis Review: Parabolic Trough and Linear Fresnel Collectors," Renewable and Sustainable Energy Reviews, **199**, p. 114497. https://doi.org/10.1016/j.rser.2024.114497.

[33] Morin, G., Dersch, J., Platzer, W., Eck, M., and Häberle, A., 2012, "Comparison of Linear Fresnel and Parabolic Trough Collector Power

Plants," Solar Energy, **86**(1), pp. 1–12. https://doi.org/10.1016/j.solener.2011.06.020.

[34] Alami, A. H., Olabi, A. G., Mdallal, A., Rezk, A., Radwan, A., Rahman, S. M. A., Shah, S. K., and Abdelkareem, M. A., 2023, "Concentrating Solar Power (CSP) Technologies: Status and Analysis," International Journal of Thermofluids, **18**, p. 100340. https://doi.org/10.1016/j.ijft.2023.100340.

[35] Wang, Q., Yao, Y., Shen, Y., Shen, Z., and Yang, H., 2024, "A Mutually Beneficial System Incorporating Parabolic Trough Concentrating Solar Power System with Photovoltaics: A Comprehensive Techno-Economic Analysis," Appl Energy, **360**, p. 122834. https://doi.org/https://doi.org/10.1016/j.apenergy.2024.122834.

[36] Shankar, A., Saxena, A. K., and Mazumdar, R., 2024, *Concentrating Solar Power with Storage: Deployment Essential Now*, New Delhi, India.

[37] Vant-Hull, L. L., 2012, "8 - Central Tower Concentrating Solar Power (CSP) Systems," *Concentrating Solar Power Technology*, K. Lovegrove, and W. Stein, eds., Woodhead Publishing, pp. 240–283. https://doi.org/10.1533/9780857096173.2.240.

[38] Morosini, E., Villa, E., Quadrio, G., Binotti, M., and Manzolini, G., 2023, "Solar Tower CSP Plants with Transcritical Cycles Based on CO2 Mixtures: A Sensitivity on Storage and Power Block Layouts," Solar Energy, **262**, p. 111777. https://doi.org/10.1016/j.solener.2023.05.054.

[39] Pratik, N. A., Ali, Md. H., Lubaba, N., Hasan, N., Asaduzzaman, Md., and Miyara, A., 2024, "Numerical Investigation to Optimize the Modified Cavity Receiver for Enhancement of Thermal Performance of Solar Parabolic Dish Collector System," Energy, **290**, p. 130133. https://doi.org/10.1016/j.energy.2023.130133.

[40] Jayathunga, D. S., Karunathilake, H. P., Narayana, M., and Witharana, S., 2024, "Phase Change Material (PCM) Candidates for Latent Heat Thermal Energy Storage (LHTES) in Concentrated Solar Power (CSP) Based Thermal Applications - A Review," Renewable and Sustainable Energy Reviews, **189**, p. 113904. https://doi.org/10.1016/j.rser.2023.113904.

[41] Guillén-Lambea, S., and Carvalho, M., 2021, "A Critical Review of the Greenhouse Gas Emissions Associated with Parabolic Trough Concentrating Solar Power Plants," J Clean Prod, **289**, p. 125774. https://doi.org/https://doi.org/10.1016/j.jclepro.2020.125774.

[42] Al-Maliki, W. A. K., Hadi, A. S., Al-Khafaji, H. M. H., Alobaid, F., and Epple, B., 2022, "Novel Feedwater Preheating System for Parabolic Trough Solar Power Plant," Energy Reports, **8**, pp. 10665–10687. https://doi.org/https://doi.org/10.1016/j.egyr.2022.08.190.

[43] Mohammadi, K., Khanmohammadi, S., Immonen, J., and Powell, K., 2021, "Techno-Economic Analysis and Environmental Benefits of Solar Industrial Process Heating Based on Parabolic Trough Collectors," Sustainable Energy Technologies and Assessments, **47**, p. 101412. https://doi.org/10.1016/j.seta.2021.101412.

[44] Li, C., Goswami, Y., and Stefanakos, E., 2013, "Solar Assisted Sea Water Desalination: A Review," Renewable and Sustainable Energy Reviews, **19**, pp. 136–163. https://doi.org/https://doi.org/10.1016/j.rser.2012.04.059.

[45] Mohammadi, K., Saghafifar, M., Ellingwood, K., and Powell, K., 2019, "Hybrid Concentrated Solar Power (CSP)-Desalination Systems: A Review," Desalination, **468**, p. 114083. https://doi.org/10.1016/j.desal.2019.114083.

[46] Xia, J., Li, Y., Li, C., Wang, Y., Xie, L., Miao, Y., Zhang, Q., Hao, C., and Sun, G., 2020, "Performance Evaluation of Different Solar Collectors in Building Cooling, Heating, and Hot Water Supply," Journal of Renewable and Sustainable Energy, **12**(4), p. 043701. https://doi.org/10.1063/1.5117268.

[47] Boudries, R., 2018, "Techno-Economic Study of Hydrogen Production Using CSP Technology," Int J Hydrogen Energy, **43**(6), pp. 3406–3417. https://doi.org/10.1016/j.ijhydene.2017.05.157.

[48] Belgasim, B., Aldali, Y., Abdunnabi, M. J. R., Hashem, G., and Hossin, K., 2018, "The Potential of Concentrating Solar Power (CSP) for Electricity Generation in Libya," Renewable and Sustainable Energy Reviews, **90**, pp. 1–15. https://doi.org/10.1016/j.rser.2018.03.045.

[49] Kuravi, S., Trahan, J., Goswami, D. Y., Rahman, M. M., and Stefanakos, E. K., 2013, "Thermal Energy Storage Technologies and Systems for Concentrating Solar Power Plants," Prog Energy Combust Sci, **39**(4), pp. 285–319. https://doi.org/10.1016/j.pecs.2013.02.001.

[50] Bayareh, M., and Usefian, A., 2023, "Simulation of Parabolic Trough Solar Collectors Using Various Discretization Approaches: A Review," Eng Anal Bound Elem, **153**, pp. 126–137. https://doi.org/10.1016/j.enganabound.2023.05.025.

[51] Giaconia, A., Tizzoni, A. C., Sau, S., Corsaro, N., Mansi, E., Spadoni, A., and Delise, T., 2021, "Assessment and Perspectives of Heat Transfer Fluids for CSP Applications," Energies (Basel), **14**(22). https://doi.org/10.3390/en14227486.

[52] Merchán, R. P., Santos, M. J., Medina, A., and Calvo Hernández, A., 2022, "High Temperature Central Tower Plants for Concentrated Solar Power: 2021 Overview," Renewable and Sustainable Energy Reviews, **155**, p. 111828. https://doi.org/10.1016/j.rser.2021.111828.

[53] Manikandan, G. K., Iniyan, S., and Goic, R., 2019, "Enhancing the Optical and Thermal Efficiency of a Parabolic Trough Collector – A Review," Appl Energy, **235**, pp. 1524–1540. https://doi.org/https://doi.org/10.1016/j.apenergy.2018.11.048.

[54] Rossi, G., D'Angelo, A., Diletto, C., Esposito, S., Guglielmo, A., and Lanchi, M., 2023, "New Spectrally Selective Coatings for CSP Linear Receivers Operating in Air at High Temperature," Applied Research, **n/a**(n/a), p. e202200117. https://doi.org/https://doi.org/10.1002/appl.202200117.

[55] Bilal Awan, A., Khan, M. N., Zubair, M., and Bellos, E., 2020, "Commercial Parabolic Trough CSP Plants: Research Trends and Technological Advancements," Solar Energy, **211**, pp. 1422–1458. https://doi.org/10.1016/j.solener.2020.09.072.

[56] Muñoz, J., Martinez-Val, J. M., and Ramos, A., 2011, "Thermal Regimes in Solar-Thermal Linear Collectors," Solar Energy, **85**(5), pp. 857–870. https://doi.org/10.1016/j.solener.2011.02.004.

[57] Sahoo, S. S., Singh, S., and Banerjee, R., 2013, “Steady State Hydrothermal Analysis of the Absorber Tubes Used in Linear Fresnel Reflector Solar Thermal System,” Solar Energy, **87**, pp. 84–95. https://doi.org/10.1016/j.solener.2012.10.002.

[58] Chaitanya Prasad, G. S., Reddy, K. S., and Sundararajan, T., 2017, “Optimization of Solar Linear Fresnel Reflector System with Secondary Concentrator for Uniform Flux Distribution over Absorber Tube,” Solar Energy, **150**, pp. 1–12. https://doi.org/10.1016/j.solener.2017.04.026.

[59] Collares-Pereira, M., Canavarro, D., and Chaves, J., 2017, “3 - Improved Design for Linear Fresnel Reflector Systems,” *Advances in Concentrating Solar Thermal Research and Technology*, M.J. Blanco, and L.R. Santigosa, eds., Woodhead Publishing, pp. 45–55. https://doi.org/10.1016/B978-0-08-100516-3.00003-4.

[60] Canavarro, D., Chaves, J., and Collares-Pereira, M., 2014, “Simultaneous Multiple Surface Method for Linear Fresnel Concentrators with Tubular Receiver,” Solar Energy, **110**, pp. 105–116. https://doi.org/10.1016/j.solener.2014.09.002.

[61] Bellos, E., 2019, “Progress in the Design and the Applications of Linear Fresnel Reflectors – A Critical Review,” Thermal Science and Engineering Progress, **10**, pp. 112–137. https://doi.org/10.1016/j.tsep.2019.01.014.

[62] Singh, P. L., Ganesan, S., and Yàdav, G. C., 1999, “Technical Note: Performance Study of a Linear Fresnel Concentrating Solar Device,” Renew Energy, **18**(3), pp. 409–416. https://doi.org/10.1016/S0960-1481(98)00805-2.

[63] Montes, M. J., Barbero, R., Abbas, R., and Rovira, A., 2016, “Performance Model and Thermal Comparison of Different Alternatives for the Fresnel Single-Tube Receiver,” Appl Therm Eng, **104**, pp. 162–175. https://doi.org/10.1016/j.applthermaleng.2016.05.015.

[64] Bellos, E., Mathioulakis, E., Papanicolaou, E., and Belessiotis, V., 2018, “Experimental Investigation of the Daily Performance of an Integrated Linear Fresnel Reflector System,” Solar Energy, **167**, pp. 220–230. https://doi.org/10.1016/j.solener.2018.04.019.

[65] Lin, M., Sumathy, K., Dai, Y. J., Wang, R. Z., and Chen, Y., 2013, "Experimental and Theoretical Analysis on a Linear Fresnel Reflector Solar Collector Prototype with V-Shaped Cavity Receiver," Appl Therm Eng, **51**(1), pp. 963–972. https://doi.org/10.1016/j.applthermaleng.2012.10.050.

[66] Goswami, R. P., Negi, B. S., Sehgal, H. K., and Sootha, G. D., 1990, "Optical Designs and Concentration Characteristics of a Linear Fresnel Reflector Solar Concentrator with a Triangular Absorber," Solar Energy Materials, **21**(2), pp. 237–251. https://doi.org/10.1016/0165-1633(90)90057-8.

[67] Incropera, F. P., Dewitt, D. P., Bergman, T. L., and Lavine, A. S., 2012, *Fundamentals of Heat and Mass Transfer*, Sixth ed. Wiley.

[68] Pye, J., Morrison, G., and Behnia, M., 2003, "Transient Modelling of Cavity Receiver Heat Transfer for the Compact Linear Fresnel Reflector." [Online]. Available: https://api.semanticscholar.org/CorpusID:45473442.

[69] Natarajan, S. K., Reddy, K. S., and Mallick, T. K., 2012, "Heat Loss Characteristics of Trapezoidal Cavity Receiver for Solar Linear Concentrating System," Appl Energy, **93**, pp. 523–531. https://doi.org/10.1016/j.apenergy.2011.12.011.

[70] Guadamud, E., Oliva, A., Lehmkuhl, O., Rodriguez, I., and González, I., 2015, "Thermal Analysis of a Receiver for Linear Fresnel Reflectors," Energy Procedia, **69**, pp. 405–414. https://doi.org/10.1016/j.egypro.2015.03.047.

[71] Cagnoli, M., Mazzei, D., Procopio, M., Russo, V., Savoldi, L., and Zanino, R., 2018, "Analysis of the Performance of Linear Fresnel Collectors: Encapsulated vs. Evacuated Tubes," Solar Energy, **164**, pp. 119–138. https://doi.org/10.1016/j.solener.2018.02.037.

[72] Olson, K. D., and Talghader, J. J., 2016, "Solar Selective Coating Optimization for Direct Steam Generation Parabolic Trough Designs," Solar Energy, **124**, pp. 82–88. https://doi.org/10.1016/j.solener.2015.12.006.

[73] Esposito, S., D'Angelo, A., Antonaia, A., Castaldo, A., Ferrara, M., Addonizio, M. L., and Guglielmo, A., 2016, "Optimization Procedure and Fabrication of Highly Efficient and Thermally Stable Solar Coating for

Receiver Operating at High Temperature," Solar Energy Materials and Solar Cells, **157**, pp. 429–437. https://doi.org/10.1016/j.solmat.2016.06.047.

[74] Yang, H., Wang, Q., Huang, Y., Feng, J., Ao, X., Hu, M., and Pei, G., 2019, "Spectral Optimization of Solar Selective Absorbing Coating for Parabolic Trough Receiver," Energy, **183**, pp. 639–650. https://doi.org/10.1016/j.energy.2019.06.090.

[75] Yang, H., Wang, Q., Huang, X., Li, J., and Pei, G., 2018, "Performance Study and Comparative Analysis of Traditional and Double-Selective-Coated Parabolic Trough Receivers," Energy, **145**, pp. 206–216. https://doi.org/10.1016/j.energy.2017.12.126.

[76] Yang, H., Wang, Q., Zhong, S., Kwan, T. H., Feng, J., Cao, J., and Pei, G., 2020, "Spectral-Spatial Design and Coupling Analysis of the Parabolic Trough Receiver," Appl Energy, **264**, p. 114692. https://doi.org/10.1016/j.apenergy.2020.114692.

[77] Zhao, K., Jin, H., Gai, Z., and Hong, H., 2022, "A Thermal Efficiency-Enhancing Strategy of Parabolic Trough Collector Systems by Cascadingly Applying Multiple Solar Selective-Absorbing Coatings," Appl Energy, **309**, p. 118508. https://doi.org/10.1016/j.apenergy.2021.118508.

[78] Singh, S. K., Tiwari, A. K., and Paliwal, H. K., 2023, "Performance Augmentation Strategy of Parabolic Trough Collector by Employing MXene-Based Solar Absorbing Coating," Process Safety and Environmental Protection, **174**, pp. 971–982. https://doi.org/10.1016/j.psep.2023.05.007.

[79] Stanek, B., Wang, W., and Bartela, Ł., 2023, "A Potential Solution in Reducing the Parabolic Trough Based Solar Industrial Process Heat System Cost by Partially Replacing Absorbers Coatings with Non-Selective Ones in Initial Loop Sections," Appl Energy, **331**, p. 120472. https://doi.org/10.1016/j.apenergy.2022.120472.

[80] Raccurt, O., Disdier, A., Bourdon, D., Donnola, S., Stollo, A., and Gioconia, A., 2015, "Study of the Stability of a Selective Solar Absorber Coating under Air and High Temperature Conditions," Energy Procedia, **69**, pp. 1551–1557. https://doi.org/10.1016/j.egypro.2015.03.107.

[81] Wang, X., Lee, E., Xu, C., and Liu, J., 2021, "High-Efficiency, Air-Stable Manganese–Iron Oxide Nanoparticle-Pigmented Solar Selective Absorber Coatings toward Concentrating Solar Power Systems Operating at 750 °C," Mater Today Energy, **19**, p. 100609. https://doi.org/https://doi.org/10.1016/j.mtener.2020.100609.

[82] Cau, G., and Cocco, D., 2014, "Comparison of Medium-Size Concentrating Solar Power Plants Based on Parabolic Trough and Linear Fresnel Collectors," Energy Procedia, **45**, pp. 101–110. https://doi.org/10.1016/j.egypro.2014.01.012.

[83] Cocco, D., and Cau, G., 2015, "Energy and Economic Analysis of Concentrating Solar Power Plants Based on Parabolic Trough and Linear Fresnel Collectors," Proceedings of the Institution of Mechanical Engineers, Part A: Journal of Power and Energy, **229**(6), pp. 677–688. https://doi.org/10.1177/0957650915587433.

[84] Sait, H. H., Martinez-Val, J. M., Abbas, R., and Munoz-Anton, J., 2015, "Fresnel-Based Modular Solar Fields for Performance/Cost Optimization in Solar Thermal Power Plants: A Comparison with Parabolic Trough Collectors," Appl Energy, **141**, pp. 175–189. https://doi.org/10.1016/j.apenergy.2014.11.074.

[85] Rovira, A., Barbero, R., Montes, M. J., Abbas, R., and Varela, F., 2016, "Analysis and Comparison of Integrated Solar Combined Cycles Using Parabolic Troughs and Linear Fresnel Reflectors as Concentrating Systems," Appl Energy, **162**, pp. 990–1000. https://doi.org/10.1016/j.apenergy.2015.11.001.

[86] Purohit, I., and Purohit, P., 2017, "Technical and Economic Potential of Concentrating Solar Thermal Power Generation in India," Renewable and Sustainable Energy Reviews, **78**, pp. 648–667. https://doi.org/10.1016/j.rser.2017.04.059.

[87] Bellos, E., 2023, "A Geospatial Comparative Analysis of Solar Thermal Concentrating Power Systems in Greece," Cleaner Energy Systems, **4**, p. 100055. https://doi.org/10.1016/j.cles.2023.100055.

[88] Bendato, I., Cassettari, L., Mosca, M., and Mosca, R., 2016, "Stochastic Techno-Economic Assessment Based on Monte Carlo Simulation and the

Response Surface Methodology: The Case of an Innovative Linear Fresnel CSP (Concentrated Solar Power) System," Energy, **101**, pp. 309–324. https://doi.org/10.1016/j.energy.2016.02.048.

[89] Montes, M. J., Abbas, R., Muñoz, M., Muñoz-Antón, J., and Martínez-Val, J. M., 2017, "Advances in the Linear Fresnel Single-Tube Receivers: Hybrid Loops with Non-Evacuated and Evacuated Receivers," Energy Convers Manag, **149**, pp. 318–333. https://doi.org/10.1016/j.enconman.2017.07.031.

[90] Osorio, J. D., and Rivera-Alvarez, A., 2022, "Influence of the Concentration Ratio on the Thermal and Economic Performance of Parabolic Trough Collectors," Renew Energy, **181**, pp. 786–802. https://doi.org/10.1016/j.renene.2021.09.040.

[91] Pelay, U., Luo, L., Fan, Y., Stitou, D., and Rood, M., 2017, "Thermal Energy Storage Systems for Concentrated Solar Power Plants," Renewable and Sustainable Energy Reviews, **79**, pp. 82–100. https://doi.org/10.1016/j.rser.2017.03.139.

[92] Elfeky, K. E., Ahmed, N., and Wang, Q., 2018, "Numerical Comparison between Single PCM and Multi-Stage PCM Based High Temperature Thermal Energy Storage for CSP Tower Plants," Appl Therm Eng, **139**, pp. 609–622. https://doi.org/10.1016/j.applthermaleng.2018.04.122.

[93] Bellan, S., Alam, T. E., González-Aguilar, J., Romero, M., Rahman, M. M., Goswami, D. Y., and Stefanakos, E. K., 2015, "Numerical and Experimental Studies on Heat Transfer Characteristics of Thermal Energy Storage System Packed with Molten Salt PCM Capsules," Appl Therm Eng, **90**, pp. 970–979. https://doi.org/10.1016/j.applthermaleng.2015.07.056.

[94] Xu, C., Wang, Z., He, Y., Li, X., and Bai, F., 2012, "Sensitivity Analysis of the Numerical Study on the Thermal Performance of a Packed-Bed Molten Salt Thermocline Thermal Storage System," Appl Energy, **92**, pp. 65–75. https://doi.org/10.1016/j.apenergy.2011.11.002.

[95] Hatte, S., Mira-Hernández, C., Advaith, S., Tinaikar, A., Chetia, U. K., Manu, K. V, Chattopadhyay, K., Weibel, J. A., Garimella, S. V, Srinivasan, V., and Basu, S., 2016, "Short and Long-Term Sensitivity of Lab-Scale Thermocline Based Thermal Storage to Flow Disturbances," Appl Therm

Eng, **109**, pp. 936–948. https://doi.org/10.1016/j.applthermaleng.2016.04.138.

[96] Shaikh, W., Wadegaonkar, A., Kedare, S. B., and Bose, M., 2018, "Numerical Simulation of Single Media Thermocline Based Storage System," Solar Energy, **174**, pp. 207–217. https://doi.org/10.1016/j.solener.2018.08.084.

[97] Advaith, S., Parida, D. R., Aswathi, K. T., Dani, N., Chetia, U. K., Chattopadhyay, K., and Basu, S., 2021, "Experimental Investigation on Single-Medium Stratified Thermal Energy Storage System," Renew Energy, **164**, pp. 146–155. https://doi.org/10.1016/j.renene.2020.09.092.

[98] Gajbhiye, P., Salunkhe, N., Kedare, S., and Bose, M., 2018, "Experimental Investigation of Single Media Thermocline Storage with Eccentrically Mounted Vertical Porous Flow Distributor," Solar Energy, **162**, pp. 28–35. https://doi.org/10.1016/j.solener.2017.12.062.

[99] Joshi, V., Wasnik, C., Wadegaonkar, A., Kedare, S. B., and Bose, M., 2021, "Influence of Porosity and Permeability of Flow Distributor on Thermal Stratification in Single Media Storage Tank," J Energy Storage, **44**, p. 103241. https://doi.org/10.1016/j.est.2021.103241.

[100] Gajbhiye, P., Kedare, S., and Bose, M., 2022, "Experimental Analysis of Parameters Influencing Thermal Stratification in Single Media Single Tank Storage System with Flow Distributor," Thermal Science and Engineering Progress, **30**, p. 101243. https://doi.org/10.1016/j.tsep.2022.101243.

[101] Lou, W., Fan, Y., and Luo, L., 2020, "Single-Tank Thermal Energy Storage Systems for Concentrated Solar Power: Flow Distribution Optimization for Thermocline Evolution Management," J Energy Storage, **32**, p. 101749. https://doi.org/10.1016/j.est.2020.101749.

[102] Lou, W., Xie, B., Aubril, J., Fan, Y., Luo, L., and Arrivé, A., 2023, "Optimized Flow Distributor for Stabilized Thermal Stratification in a Single-Medium Thermocline Storage Tank: A Numerical and Experimental Study," Energy, **263**, p. 125709. https://doi.org/10.1016/j.energy.2022.125709.

[103] Lou, W., Baudin, N., Roux, S., Fan, Y., and Luo, L., 2023, "Impact of Buoyant Jet Entrainment on the Thermocline Behavior in a Single-Medium Thermal Energy Storage Tank," J Energy Storage, **71**, p. 108017. https://doi.org/10.1016/j.est.2023.108017.

[104] Gaggioli, W., Liberatore, R., Di Ascenzi, P., Mazzei, D., and Russo, V., 2020, "Experimental Test of Characterization of an Innovative Thermal Energy Storage System Based on Low Melting Molten Salt Thermocline Tank Integrated with an Oil Exchanger," AIP Conf Proc, **2303**(1), p. 190012. https://doi.org/10.1063/5.0028779.

[105] Cagnoli, M., Gaggioli, W., Liberatore, R., Russo, V., and Zanino, R., 2023, "CFD Modelling of an Indirect Thermocline Energy Storage Prototype for CSP Applications," Solar Energy, **259**, pp. 86–98. https://doi.org/10.1016/j.solener.2023.05.019.

[106] Elfeky, K. E., Li, X., Ahmed, N., Lu, L., and Wang, Q., 2019, "Optimization of Thermal Performance in Thermocline Tank Thermal Energy Storage System with the Multilayered PCM(s) for CSP Tower Plants," Appl Energy, **243**, pp. 175–190. https://doi.org/10.1016/j.apenergy.2019.03.182.

[107] Wang, Z., Zhang, H., Dou, B., Zhang, G., and Wu, W., 2019, "Influence of Inlet Structure on Thermal Stratification in a Heat Storage Tank with PCMs: CFD and Experimental Study," Appl Therm Eng, **162**, p. 114151. https://doi.org/10.1016/j.applthermaleng.2019.114151.

[108] Wu, M., Xu, C., and He, Y.-L., 2014, "Dynamic Thermal Performance Analysis of a Molten-Salt Packed-Bed Thermal Energy Storage System Using PCM Capsules," Appl Energy, **121**, pp. 184–195. https://doi.org/10.1016/j.apenergy.2014.01.085.

[109] Galione, P. A., Pérez-Segarra, C. D., Rodríguez, I., Oliva, A., and Rigola, J., 2015, "Multi-Layered Solid-PCM Thermocline Thermal Storage Concept for CSP Plants. Numerical Analysis and Perspectives," Appl Energy, **142**, pp. 337–351. https://doi.org/10.1016/j.apenergy.2014.12.084.

[110] Galione, P. A., Pérez-Segarra, C. D., Rodríguez, I., Torras, S., and Rigola, J., 2015, "Multi-Layered Solid-PCM Thermocline Thermal Storage for CSP. Numerical Evaluation of Its Application in a 50MWe Plant," Solar Energy, **119**, pp. 134–150. https://doi.org/10.1016/j.solener.2015.06.029.

[111] Zhao, B., Cheng, M., Liu, C., and Dai, Z., 2016, "Thermal Performance and Cost Analysis of a Multi-Layered Solid-PCM Thermocline Thermal Energy Storage for CSP Tower Plants," Appl Energy, **178**, pp. 784–799. https://doi.org/10.1016/j.apenergy.2016.06.034.

[112] Zhao, B., Cheng, M., Liu, C., and Dai, Z., 2017, "Cyclic Thermal Characterization of a Molten-Salt Packed-Bed Thermal Energy Storage for Concentrating Solar Power," Appl Energy, **195**, pp. 761–773. https://doi.org/10.1016/j.apenergy.2017.03.110.

[113] Wang, Z., Zhang, H., Huang, H., Dou, B., Huang, X., and Goula, M. A., 2019, "The Experimental Investigation of the Thermal Stratification in a Solar Hot Water Tank," Renew Energy, **134**, pp. 862–874. https://doi.org/10.1016/j.renene.2018.11.088.

[114] Suresh, C., and Saini, R. P., 2020, "Experimental Study on Combined Sensible-Latent Heat Storage System for Different Volume Fractions of PCM," Solar Energy, **212**, pp. 282–296. https://doi.org/10.1016/j.solener.2020.11.013.

[115] Keilany, M. A., Vannerem, S., Milhé, M., Falcoz, Q., Bézian, J.-J., and Flamant, G., 2022, "Experimental and Numerical Study of Combining Encapsulated Phase Change Material to Sensible Heat Storage Material in One-Tank Pilot Scale Thermal Energy Storage," J Energy Storage, **51**, p. 104504. https://doi.org/10.1016/j.est.2022.104504.

[116] Elfeky, K. E., Mohammed, A. G., and Wang, Q., 2022, "Thermo-Economic Evaluation of PCM Layer Thickness Change on the Performance of the Hybrid Heat Storage Tank for Concentrating Solar Power Plants," Energy, **253**, p. 124128. https://doi.org/10.1016/j.energy.2022.124128.

[117] Zahid, M. S., Ahmed, N., Qaisrani, M. A., Mahmood, M., Ali, M., Waqas, A., and Assadi, M., 2022, "Charging and Discharging Characterization of a Novel Combined Sensible-Latent Heat Thermal Energy Storage System by Experimental Investigations for Medium Temperature Applications," J Energy Storage, **55**, p. 105612. https://doi.org/10.1016/j.est.2022.105612.

[118] Elfeky, K. E., Mohammed, A. G., Ahmed, N., and Wang, Q., 2023, "Thermo-Mechanical Investigation of the Multi-Layer Thermocline Tank

for Parabolic Trough Power Plants," Energy, **268**, p. 126749. https://doi.org/10.1016/j.energy.2023.126749.

[119] Shokrnia, M., Cagnoli, M., Grena, R., D'Angelo, A., Lanchi, M., and Zanino, R., 2024, "Photo-Thermal Optimization of a Parabolic Trough Collector with Arrayed Selective Coatings," Energies (Basel), **17**(13). https://doi.org/10.3390/en17133221.

[120] Ferri, R., Cammi, A., and Mazzei, D., 2008, "Molten Salt Mixture Properties in RELAP5 Code for Thermodynamic Solar Applications," International Journal of Thermal Sciences, **47**(12), pp. 1676–1687. https://doi.org/10.1016/j.ijthermalsci.2008.01.007.

[121] Esposito, S., Antonaia, A., Addonizio, M. L., and Aprea, S., 2009, "Fabrication and Optimisation of Highly Efficient Cermet-Based Spectrally Selective Coatings for High Operating Temperature," Thin Solid Films, **517**(21), pp. 6000–6006. https://doi.org/10.1016/j.tsf.2009.03.191.

[122] Forristall, R., 2003, *Heat Transfer Analysis and Modeling of a Parabolic Trough Solar Receiver Implemented in Engineering Equation Solver, Technical Report, NREL/TP-550-34169*.

[123] Österholm, R., and Pålsson, J., 2014, "Dynamic Modelling of a Parabolic Trough Solar Power Plant." [Online]. Available: https://api.semanticscholar.org/CorpusID:55951272.

[124] Rodriguez-Sanchez, M. R., Soria, A., Almendros-Ibáñez, J. A., Acosta-Iborra, A., and Santana, D., 2014, "Thermal Design Guidelines of Solar Power Towers," Appl Therm Eng, **63**, pp. 428–438. https://doi.org/10.1016/j.applthermaleng.2013.11.014.

[125] Soltigua, 2015, *1MWe CSP-ORC Pilot Plant, Solar Field Process Description. Report No.: S-F14ET001-M-B-A-2602-C*.

[126] Marshal, N., 1976, *Gas Encyclopedia*, Elsevier, New York.

[127] Martynenko, O. G., and Khramtsov, P., 2005, *Free-Convection Heat Transfer*, Springer, New York.

[128] ASTM International, 2003, *Standard G173-03: Standard Tables for Reference Solar Spectral Irradiances: Direct Normal and Hemispherical on*

37° Tilted Surface. Derived from SMARTS v. 2.9.2. Https://Www.Astm.Org/Standards/G173.Htm.

[129] Morin, G., Dersch, J., Platzer, W., Eck, M., and Häberle, A., 2012, "Comparison of Linear Fresnel and Parabolic Trough Collector Power Plants," Solar Energy, **86**(1), pp. 1–12. https://doi.org/https://doi.org/10.1016/j.solener.2011.06.020.

[130] Richter, C., 2008, *Solar Power and Chemical Energy Systems, SolarPACES Annual Report*.

[131] Shokrnia, M., Cagnoli, M., Grena, R., D'Angelo, A., Lanchi, M., and Zanino, R., 2024, "Comparative Techno-Economic Analysis of Parabolic Trough and Linear Fresnel Collectors with Evacuated and Non-Evacuated Receiver Tubes in Different Geographical Regions," Processes, **12**(11). https://doi.org/10.3390/pr12112376.

[132] SolarPACES, 2022, "Partanna MS-LFR CSP Project," https://solarpaces.nrel.gov/project/partanna-ms-lfr.

[133] Falchetta, M., Mazzei, D., Russo, V., Campanella, V., Floridia, V., Schiavo, B., Venezia, L., Brunatto, C., and Orlando, R., 2020, "The Partanna Project: A First of a Kind Plant Based on Molten Salts in LFR Collectors." [Online]. Available: https://api.semanticscholar.org/CorpusID:234573255.

[134] Falchetta, M., Gambarotta, A., Vaja, I., Cucumo, M., and Manfredi, C., 2006, "Modelling and Simulation of the Thermo and Fluid Dynamics of the 'Archimede Project' Solar Power Station," *Renewable Energy Processes and Systems*, National Technical University of Athens.

[135] Vignolini, M., 2009, *A New Approach to Concentrating Solar Plant (CSP) by ENEA*.

[136] ENEA, 2015, *Laboratorio Di Qualificazione Collettori e Sistemi Solari, Technical Report N° RT.2015.COL183.1*.

[137] Blanco, M. J., Mutuberria, A., and Martinez, D., 2010, "Experimental Validation of Tonatiuh Using the Plataforma Solar de Almería Secondary Concentrator Test campaign Data," *16th Annual SolarPACES Symposium*, Perpignan, France.

[138] Bonanos, A. M., Georgiou, M. C., Stokos, K. G., and Papanicolas, C. N., 2019, "Engineering Aspects and Thermal Performance of Molten Salt Transfer Lines in Solar Power Applications," Appl Therm Eng, **154**, pp. 294–301. https://doi.org/10.1016/j.applthermaleng.2019.03.091.

[139] He, Y.-L., Qiu, Y., Wang, K., Yuan, F., Wang, W.-Q., Li, M.-J., and Guo, J.-Q., 2020, "Perspective of Concentrating Solar Power," Energy, **198**, p. 117373. https://doi.org/10.1016/j.energy.2020.117373.

[140] Siemens, 2021, "Star-CCM+. https://Www.Plm.Automation.Siemens.Com/Global/En/Products/Simcenter/STAR-CCM.Html."

[141] Menter, F. R., 1994, "Two-Equation Eddy-Viscosity Turbulence Models for Engineering Applications," AIAA Journal, **32**(8), pp. 1598–1605. https://doi.org/10.2514/3.12149.

[142] CD-ADAPCO, 2014, "STAR CCM+ User Guide, Version 9.02."

[143] PVGIS, 2022, "European Commission, Https://Re.Jrc.Ec.Europa.Eu/."

[144] Xiao, G., Nie, J., Xu, H., Zhang, C., and Zhu, P., 2022, "Performance Analysis of a Solar Power Tower Plant Integrated with Trough Collectors," Appl Therm Eng, **214**, p. 118853. https://doi.org/10.1016/j.applthermaleng.2022.118853.

[145] SAM, 2022, "System Advisor Model [Software]. Version 21.11.2022. Https://Sam.Nrel.Gov/."

[146] Kamel, S., Agyekum, E. B., Adebayo, T. S., Taha, I. B. M., Gyamfi, B. A., and Yaqoob, S. J., 2022, "Comparative Analysis of Rankine Cycle Linear Fresnel Reflector and Solar Tower Plant Technologies: Techno-Economic Analysis for Ethiopia," Sustainability, **14**(3), p. 1677. [Online]. Available: https://www.mdpi.com/2071-1050/14/3/1677.

[147] Islam, M. T., Huda, N., and Saidur, R., 2019, "Current Energy Mix and Techno-Economic Analysis of Concentrating Solar Power (CSP) Technologies in Malaysia," Renew Energy, **140**, pp. 789–806. https://doi.org/10.1016/j.renene.2019.03.107.

[148] Aseri, T. K., Sharma, C., and Kandpal, T. C., 2021, "Estimation of Capital Costs and Techno-Economic Appraisal of Parabolic Trough Solar Collector and Solar Power Tower Based CSP Plants in India for Different Condenser Cooling Options," Renew Energy, **178**, pp. 344–362. https://doi.org/10.1016/j.renene.2021.05.166.

[149] Aseri, T. K., Sharma, C., and Kandpal, T. C., 2022, "A Techno-Economic Appraisal of Parabolic Trough Collector and Central Tower Receiver Based Solar Thermal Power Plants in India: Effect of Nominal Capacity and Hours of Thermal Energy Storage," J Energy Storage, **48**, p. 103976. https://doi.org/10.1016/j.est.2022.103976.

[150] Arnaoutakis, G. E., Katsaprakakis, D. Al., and Christakis, D. G., 2022, "Dynamic Modeling of Combined Concentrating Solar Tower and Parabolic Trough for Increased Day-to-Day Performance," Appl Energy, **323**, p. 119450. https://doi.org/10.1016/j.apenergy.2022.119450.

[151] Cheng, Z.-D., Zhao, X.-R., He, Y.-L., and Qiu, Y., 2018, "A Novel Optical Optimization Model for Linear Fresnel Reflector Concentrators," Renew Energy, **129**, pp. 486–499. https://doi.org/10.1016/j.renene.2018.06.019.

[152] Ling-zhi, R., Xin-gang, Z., Yu-zhuo, Z., and Yan-bin, L., 2018, "The Economic Performance of Concentrated Solar Power Industry in China," J Clean Prod, **205**, pp. 799–813. https://doi.org/10.1016/j.jclepro.2018.09.110.

[153] Shokrnia, M., Cagnoli, M., Gaggioli, W., Liberatore, R., Russo, V., and Zanino, R., 2024, "Geometrical and PCM Optimization of a Thermocline Energy Storage System," J Energy Storage, **98**, p. 113070. https://doi.org/10.1016/j.est.2024.113070.

[154] Laue, W., Thiemann, M., Scheibler, E., and Wiegand, K. W., "Nitrates and Nitrites," *Ullmann's Encyclopedia of Industrial Chemistry*. https://doi.org/10.1002/14356007.a17_265.

[155] Pradeep, N., and Reddy, K. S., 2022, "Development of an Effective Algorithm for Selection of PCM Based Filler Material for Thermocline Thermal Energy Storage System," Solar Energy, **236**, pp. 666–686. https://doi.org/10.1016/j.solener.2022.02.044.

[156] Coscia, K., Neti, S., Oztekin, A., Nelle, S., Mohapatra, S. C., and Elliott, T., 2011, "The Thermophysical Properties of the NaNO3-KNO3, LiNO3-NaNO3, and LiNO3-KNO3 Systems." [Online]. Available: https://api.semanticscholar.org/CorpusID:92820564.

[157] Zhou, D., and Eames, P., 2017, "A Study of a Eutectic Salt of Lithium Nitrate and Sodium Chloride (87–13%) for Latent Heat Storage," Solar Energy Materials and Solar Cells, **167**, pp. 157–161. https://doi.org/10.1016/j.solmat.2017.04.016.

[158] Zhao, C. Y., and Wu, Z. G., 2011, "Thermal Property Characterization of a Low Melting-Temperature Ternary Nitrate Salt Mixture for Thermal Energy Storage Systems," Solar Energy Materials and Solar Cells, **95**(12), pp. 3341–3346. https://doi.org/10.1016/j.solmat.2011.07.029.

[159] Wang Y. Q., Ormiston S. J., and Penner L. A., 2000, "ANALYSIS OF LAMINAR FORCED CONVECTION OF AIR FOR CROSSFLOW IN BANKS OF STAGGERED TUBES," Numeri Heat Transf A Appl, **38**(8), pp. 819–845. https://doi.org/10.1080/104077800457449.

[160] Bergman, T. L., Lavine, A. S., Incropera, F. P., and DeWitt, D. P., 2011, *Introduction to Heat Transfer*, 6th ed. John Wiley & Sons.

[161] Purandare, P. S., Lele, M. M., and Gupta, R. K., 2015, "Investigation on Thermal Analysis of Conical Coil Heat Exchanger," Int J Heat Mass Transf, **90**, pp. 1188–1196. https://doi.org/10.1016/j.ijheatmasstransfer.2015.07.044.

[162] Wu, X., and Tang, Z., 2023, "Heat Transfer and Storage Characteristics of a Hexagonal Close Structured Packed-Bed Thermal Storage System with Molten Salt Phase Change Materials," J Energy Storage, **65**, p. 107356. https://doi.org/10.1016/j.est.2023.107356.

[163] Oliver, D. R., 1962, "The Effect of Natural Convection on Viscous-Flow Heat Transfer in Horizontal Tubes," Chem Eng Sci, **17**(5), pp. 335–350. https://doi.org/10.1016/0009-2509(62)80035-9.

[164] Archibold, A. R., Rahman, M. M., Goswami, D. Y., and Stefanakos, E. K., 2014, "Analysis of Heat Transfer and Fluid Flow during Melting inside

a Spherical Container for Thermal Energy Storage," Appl Therm Eng, **64**(1), pp. 396–407. https://doi.org/10.1016/j.applthermaleng.2013.12.016.

[165] Liu, M.-J., Fan, L.-W., Zhu, Z.-Q., Feng, B., Zhang, H.-C., and Zeng, Y., 2016, "A Volume-Shrinkage-Based Method for Quantifying the Inward Solidification Heat Transfer of a Phase Change Material Filled in Spherical Capsules," Appl Therm Eng, **108**, pp. 1200–1205. https://doi.org/10.1016/j.applthermaleng.2016.08.027.

[166] Nazzi Ehms, J. H., De Césaro Oliveski, R., Oliveira Rocha, L. A., and Biserni, C., 2018, "Theoretical and Numerical Analysis on Phase Change Materials (PCM): A Case Study of the Solidification Process of Erythritol in Spheres," Int J Heat Mass Transf, **119**, pp. 523–532. https://doi.org/10.1016/j.ijheatmasstransfer.2017.11.124.

[167] Li, W., Wang, Y.-H., and Kong, C.-C., 2015, "Experimental Study on Melting/Solidification and Thermal Conductivity Enhancement of Phase Change Material inside a Sphere," International Communications in Heat and Mass Transfer, **68**, pp. 276–282. https://doi.org/10.1016/j.icheatmasstransfer.2015.09.004.

[168] Jegadheeswaran, S., Pohekar, S. D., and Kousksou, T., 2010, "Exergy Based Performance Evaluation of Latent Heat Thermal Storage System: A Review," Renewable and Sustainable Energy Reviews, **14**(9), pp. 2580–2595. https://doi.org/10.1016/j.rser.2010.07.051.